

# **WORKING TITLE:**

## **Water at $\alpha$ -Alumina Quanteneffekte, Wasser auf Metalloxidoberflächen**

Dissertation zur Erlangung des akademischen Grades  
(*doctor rerum naturalium*) (Dr. rer. nat.)  
in der Wissenschaftsdisziplin Theoretische Chemie

vorgelegt von  
**Sophia L. Heiden**

an der  
Mathematisch-Naturwissenschaftlichen Fakultät  
der Universität Potsdam



Potsdam, 2018

This work has been done between January 2015 and xx 2018 in the workgroup of Prof. Dr. Peter Saalfrank at the Institute of Chemistry at the University of Potsdam.

Potsdam, xx 2018

Erstgutachter: Prof. Dr. Peter Saalfrank (Uni Potsdam)  
Zweitgutachter: Prof. Dr. Beate Paulus (FU Berlin)  
Drittgutachter: Prof. Dr. xy

## Preamble

The importance of surface science in our industrialized world is overwhelming, because most processes in industry are carried out using (heterogeneous) catalysts [1–3]. These do not have to be separated from the reactants and the product after the process, which is mostly a costly step in the production of chemicals. It is therefore desirable to understand heterogeneous catalytic processes by learning more about the microscopic processes that take place on the surface of materials. Metal oxide materials are frequently used in catalysts as well as catalyst support materials, so that understanding their properties in contact with chemicals, in this work water, is crucial.

Aluminum is used in rocket fuels as a reduction agent so that during launch alumina particles are ejected in the atmosphere during the start [4]. For a space shuttle the start can produce around 276,000 kg of alumina particles [5]. It can be measured that approximately one third of these particles can be deposited in the stratosphere [6] (in an altitude between 15 and 50 km above the surface of the earth) and there it can react with the water and other molecules in the stratosphere where these particles are accumulated after the launch of a shuttle [7, 8].

Also in geochemical sciences  $\text{Al}_2\text{O}_3$  is a subject of a variety of studies since aluminum is the third most common element in the crust with 6.3% (

[http://www.unterra.de/rutherford/tab\\_hauf.htm](http://www.unterra.de/rutherford/tab_hauf.htm)

*Riedel [9]: Alumina is the most abundant metal in the crust and the third most element therein. Component of feldspar, Glimmer and clay minerals (with silicates), more seldomly as corundum and "Schmirgel". Some of them are precious stones ruby, saphir*

Dtv-Atlas [10]: third most abundant element, 8.1% of the earth crust and with that the far most abundant metal ) and it also can be seen as a model systems for more complex aluminosilicates. Oxide rocks are omnipresent in the crust of the earth and henceforth in most geochemical processes since the times the earth's atmosphere became oxidizing with rise of photosynthetic life forms/(bacteria?) 2.3 billion years ago *TODO: seems to be not true:* <https://nai.nasa.gov/articles/2011/12/2/earths-early-atmosphere-an-update/> and

### *Preamble*

<https://www.nature.com/articles/nature10655> [11]. Before under reductive conditions sulfidic rocks were dominant but when photosynthesis became more common with the rise of more advanced life forms, the oxygen content of the atmosphere grew giving rise to oxidic metal compounds.

# Contents

<b>Preamble</b>	<b>3</b>
<b>1. Theory und Methodology</b>	<b>7</b>
1.1. Density Functional Theory . . . . .	7
1.2. Periodic Boundary Conditions . . . . .	9
1.3. Plane Wave Basis, Atom Centered Basis and Peculiarities . . . . .	12
1.4. <i>Ab Initio</i> Molecular Dynamics . . . . .	13
1.5. Frequencies and Intensities . . . . .	15
1.6. Finding Transition States . . . . .	16
1.7. From Density Functionals to Hybrids and Perturbation Theory . . . . .	18
1.7.1. Hybrid Functionals . . . . .	18
1.7.2. Møller Plesset Peturbation Theory . . . . .	18
1.8. Computational Details and Used Programs . . . . .	20
<b>2. Water on <math>\alpha\text{-Al}_2\text{O}_3(11\bar{2}0)</math></b>	<b>21</b>
2.1. Surface Model . . . . .	21
2.2. Structure Search . . . . .	24
2.3. Reactions and Microkinetic Model . . . . .	29
2.4. Vibrational Frequencies . . . . .	36
2.4.1. Normal Mode Analysis . . . . .	37
2.4.2. Born Effective Charges . . . . .	47
2.4.3. Velocity-Velocity Autocorrelation Function . . . . .	48
<b>3. Water on <math>\alpha\text{-Al}_2\text{O}_3(0001)</math></b>	<b>51</b>
3.1. Surface Model and Static Calculations . . . . .	51
3.2. AIMD for MBS Process . . . . .	54
3.2.1. Beam Model . . . . .	55
3.2.2. Example Trajectories . . . . .	56
3.2.3. Microcanonical AIMD at clean surface . . . . .	59
3.2.4. Thermalized Surface . . . . .	61

## *Contents*

3.2.5. Refined Surface Model . . . . .	62
3.2.6. Refined Beam Model . . . . .	65
3.3. Improvement of Reaction Rates . . . . .	69
3.3.1. MP2 and B3LYP . . . . .	70
<b>Summary</b>	<b>71</b>
<b>Appendix</b>	<b>73</b>
A. Experimental Techniques . . . . .	73
A.1. Vibrational Sum Frequency Generation . . . . .	73
A.2. Thermal Desorption Spectroscopy . . . . .	74
A.3. Molecular Beam Source vs. Pinhole Dosing . . . . .	74
A.4. Low-Energy Electron Diffraction . . . . .	74
B. Reaction Probabilities . . . . .	75
B.1. Microcanonical AIMD at a Clean Surface at $T = 0$ . . . . .	75
B.2. Refined Surface Models: Effects of Precoverage . . . . .	75
B.3. Refined Beam Models: Clustering and Preexcitation . . . . .	76
C. $2\text{D}_2\text{O}$ Cluster . . . . .	78
<b>References</b>	<b>81</b>

# 1. Theory und Methodology

In this chapter the basics of the applied theoretical methods shall be explained. Starting from the ideas of Density Functional Theory, going over periodic boundary conditions, the specialties when dealing with atom centered bases to *ab initio* Molecular Dynamics. Proceeding with frequency calculations and intensities over Transition State Theory to more developed methods like hybrid functionals and Perturbation Theory. Most parts of this chapter are based on [12].

**MAKE SURE THAT ALL VARIABLES ARE CONSISTENT!**

## 1.1. Density Functional Theory

For all molecular and periodic systems, theoretical descriptions are based on the calculation of the electronic structure. For this, it is reasonable to separate electronic and nucleic degrees of freedom as introduced by the Born-Oppenheimer approximation [13]. With this, the electronic Schrödinger equation for the time independent case with the electronic Hamiltonian  $\hat{H}_e$ , the electronic total wave function  $\Psi_e(\underline{\mathbf{r}})$  and total energy  $E_e$  is

$$\hat{H}_e \Psi_e(\underline{\mathbf{r}}) = E_e \Psi_e(\underline{\mathbf{r}}). \quad (1.1)$$

The wave function  $\Psi_e(\underline{\mathbf{r}})$  is a function of the coordinate vector  $\underline{\mathbf{r}}$  and is  $3N_e$  dimensional, with the number of electrons  $N_e$ . For larger systems, the solution of 1.1 gets computationally demanding.

An alternative to the wave function based theory is Density Functional Theory (DFT). The idea of DFT is based on the Hohenberg Kohn theorem, that connects the ground state electronic energy to the electron density  $n(\underline{\mathbf{r}})$ , there exists a one to one correspondence. If  $\Psi(\underline{\mathbf{r}}^N)$  is a N-electron wavefunction, then the electron density can be given as

$$n(\underline{\mathbf{r}}) = N_{\text{norm}} \int \dots \int \Psi^*(\underline{\mathbf{r}}, \underline{\mathbf{r}}_2, \underline{\mathbf{r}}_3, \dots, \underline{\mathbf{r}}_N) \Psi(\underline{\mathbf{r}}, \underline{\mathbf{r}}_2, \underline{\mathbf{r}}_3, \dots, \underline{\mathbf{r}}_N) d\underline{\mathbf{r}}_2 \dots d\underline{\mathbf{r}}_N \quad (1.2)$$

**TODO:** *integral starts with  $d\underline{\mathbf{r}}_2$ ?* with the normalization factor  $N_{\text{norm}}$ . The second Hohenberg Kohn theorem, also called the variational principle of DFT proves, that a test density  $n'(\underline{\mathbf{r}})$

## 1. Theory und Methodology

will give a higher or the same energy as the exact density:

$$E_0^{exact} \leq E_0^{HK}[n'(\underline{\mathbf{r}})]. \quad (1.3)$$

In this way, the energy can be determined iteratively with the self consistent field method (SCF) by taking a guess, solving the equation and then improve the guess accordingly.

The total energy  $E[n]$  can be determined as:

$$E[n] = T[n] + V_{ext}[n] + V_{ee}[n] = \int n(\underline{\mathbf{r}})v_{ext}(\underline{\mathbf{r}})d\underline{\mathbf{r}} + T[n] + E_H[n] + E_{xc}[n] \quad (1.4)$$

with the kinetic energy  $T[n]$ , the potential energy  $V[n]$  for electron electron interaction  $ee$  and the external potential  $ext$ , the Hartree energy  $E_H[n]$ , corresponding to the classical Coulomb interaction and the exchange correlation energy  $E_{xc}[n]$  for the non-classical exchange correlation interactions. A big advantage over wave function based methods is that only a three dimensional system instead of  $3N$ -dimensional system has to be solved, with  $N$  being the number of electrons that have to be considered for three spatial coordinates  $n(x, y, z)$ . The size of a system calculated with wave function methods increases exponentially with the number of electrons, while for density calculations, we have always three spatial coordinates, independent from the number of electrons. Problematic in this ansatz is, that the explicit form of the interacting kinetic energy  $T[n]$  and the exchange correlation functional<sup>1</sup>  $E_{xc}[n]$  are unknown. Calculating all energy components from the pure density was not very successful, but Kohn and Sham presented their work in 1965 showing that the kinetic energy should be calculated from non-interacting auxiliary particles in a set of orbitals that is used for representing the electron density. A test system with non-interacting electrons that reflects the real systems electron density, is set and calculated. The use of orbitals makes it possible to use the same methods and algorithms known from wave function methods. With this the exchange-correlation functional is the only unknown functional, but it only is a small fraction of the total energy. Simple approximations to this functional still give reasonable results, as for example the Local Density Approximation (LDA). Here the homogeneous electron gas is used as a model. Furthermore, notable improvement can be made by using the first derivative of the density (generalized gradient approximation, GGA) **TODO: write a little about this?** and even better by adding second derivatives and mixing in Hartree-Fock exchange (hybrid functionals, like B3LYP and HSE06).

---

<sup>1</sup> To make clear the difference between a function and a functional: in a function (*e.g.*  $f(x)$ ), a number is produced by a set of variables, whereas in a functional ( $F[f]$ ) gives a number from a function which depends on variables.

## 1.2. Periodic Boundary Conditions

A huge problem of DFT is, that it can not be systematically improved like wave function based methods and the weakness of not being able to reproduce important features like van der Waals interactions. To overcome the latter problem it is possible to add dispersion corrections nowadays, that account for van der Waals interactions, and are important, especially for the adsorbate-surface interaction and the adsorbate-adsorbate interaction. They describe pair interactions between atoms  $A$  and  $B$  in the form:

$$E_{disp}^{(2)} = \sum_A^{N_A} \sum_{B>A}^{N_A} s_6 \frac{C_6^{AB}}{R_{AB}^6} f_{damp}(R_{AB}), \quad (1.5)$$

with the number of atoms  $N_A$ , the scaling factor  $s_6$  that is dependent on the functional, the averaged dispersion coefficient  $C_6$ , the interatomic distance  $R_{AB}$  and a damping function  $f_{damp}(R_{AB})$ . This equation gives the D2-corrections. For the more advanced D3 method,  $E_{disp}^{(2)}$  is altered by subtracting the term  $E'_{disp}^{(2)} = E_{disp}^{(2)} - \sum_A^{N_A} \sum_{B>A}^{N_A} s_8 \frac{C_8^{AB}}{R_{AB}^8} f_{damp}(R_{AB})$  and in addition a three body term  $E^{(3)}$  is added.

$$E_{disp}^{(3)} = \sum_A^{N_A} \sum_{B>A}^{N_A} \sum_{C>B>A}^{N_A} f_{damp}(\bar{R}_{ABC}) \frac{C_9^{AB} (3\cos\phi_a \cos\phi_b \cos\phi_c)}{(R_{AB} R_{BC} R_{AC})^3}. \quad (1.6)$$

Here,  $\phi_i$  are the angles of the corresponding triangle that is built by the three atoms A, B and C, and  $C_9^{ABC} = \sqrt{C_6^{AB} C_6^{BC} C_6^{AC}}$ .

## 1.2. Periodic Boundary Conditions

Surface systems can be simulated by either calculating clusters that were cut from the surface and represent an "important part" of the system or can be represented as the whole system by choosing a periodic cell. These periodic systems can be described by a single unit cell and respective cell vectors, that are used to generate the infinite system by repeating the cell in each direction. This can be either done in 1-D (polymers), 2-D (surface systems) or 3-D (bulk crystals). Also, surfaces can be described within the 3-D model as a slab with a three dimensional repetition of the unit cell. The only difference is that one has to define a vacuum gap between two slabs (unit or super cell model of a surface) in one direction perpendicular to the surface (*e.g.* here z). This gap has to be large enough to prevent unit cells from influencing each other in this direction and therefore lead to unphysical behaviour between the surface atoms and the lowest atoms of the neighboring slab above. Since it is (yet) not possible in VASP to mimic a 2-D system, in the main part of this work this vacuum gap 3-D model just mentioned was applied. Some programs, however, (*here CRYSTAL was used*) deliver the

## 1. Theory und Methodology

opportunity to calculate 2-D systems, repeating the slab only in x/y, a/b, respectively.

A disadvantage of this is, that perfect surfaces are simulated, with absolutely no defect sites. If one was to model a defect, it is repeated periodically and leads to a defined defect site density. There are models available handling this issue: the defect is only treated in one unit cell and for the others, the regular unit cell is applied. But before handling defects one has to understand the clean defect free surface properly.

The 3-D unit cell can be described by three vectors,  $\underline{\mathbf{a}}_1$ ,  $\underline{\mathbf{a}}_2$  and  $\underline{\mathbf{a}}_3$  and can be translated along these vectors to gain the infinite system. They span the space with defined length and angles, with seven different models existing. The unit cell with the atoms occupying different positions is called Bravais lattice, where 14 different form exist, *e.g.* hexagonal D<sub>6h</sub>. The lattice can be described by the lattice vector  $\underline{\mathbf{B}}$ .  $\underline{\mathbf{a}}_i$  are basis vectors of the lattice and  $n_i$  integers:

$$\underline{\mathbf{B}} = n_1 \underline{\mathbf{a}}_1 + n_2 \underline{\mathbf{a}}_2 + n_3 \underline{\mathbf{a}}_3 \quad (1.7)$$

Analogue to that, also a reciproce space exists (the so called  $\underline{\mathbf{k}}$ -space) that is the Fourier transform of the direct lattice and is defined by the reciprocal lattice vector  $\underline{\mathbf{G}}$  and a set of vectors  $\underline{\mathbf{b}}_i$  and  $h, k, l$  being integers:

$$\underline{\mathbf{G}} = h \underline{\mathbf{b}}_1 + k \underline{\mathbf{b}}_2 + l \underline{\mathbf{b}}_3 \quad (1.8)$$

that span the lattice space. The dimension of the  $\underline{\mathbf{b}}_i$  is m<sup>-1</sup>. For sampling one uses a  $\underline{\mathbf{k}}$ -point grid instead of a continuous model, where only important points within the reciproce cell have to be considered which lowers the computational costs. Due to symmetry only a reduced number of  $\underline{\mathbf{k}}$ -points have to be evaluated (irreducible  $\underline{\mathbf{k}}$ -points). For the reciproce space we have:

$$e^{i\underline{\mathbf{G}} \cdot \underline{\mathbf{B}}} = 1. \quad (1.9)$$

Between the vectors of the direct and the reciprocal space there are fixed relations, the vectors  $\underline{\mathbf{b}}_i$  can be derived from  $\underline{\mathbf{a}}_i$ , *e.g.* by writing

$$\underline{\mathbf{b}}_1 = 2\pi \frac{\underline{\mathbf{a}}_2 \times \underline{\mathbf{a}}_3}{\underline{\mathbf{a}}_1 \cdot (\underline{\mathbf{a}}_2 \times \underline{\mathbf{a}}_3)} \quad (1.10)$$

and so forth, analogously, and they are perpendicular to each other:

$$\underline{\mathbf{a}}_i \cdot \underline{\mathbf{b}}_j = 2\pi \delta_{ij}, \quad (1.11)$$

## 1.2. Periodic Boundary Conditions

with  $\delta_{ij}$  being the Kronecker delta.

The unit cell within the reciprocal space, what is called Wigner-Seitz cell in the real space, is also referred to as first Brillouin zone, whose center is the  $\Gamma$ -point ( $h = k = l = 0$ ). It is a uniquely defined primitive cell in reciprocal space that contains all critical points of interest. The integers  $h$ ,  $k$ , and  $l$  from Equation 1.8 are also called Miller indices, that can be used to describe the crystallographic planes (position of the surface in the coordinate system). They are determined by finding the point of intersection of the surface plane with the axes of the coordinate system, reduce, then take the reciprocal values and multiply with the least common multiple to gain three integers.

Within the hexagonal (and rhombohedral) lattice system, also the Miller-Bravais notation with four indices can be used  $[h, k, i, l]$ . Here,  $i$  is redundant and the relation between  $h$ ,  $k$  and  $i$  is:  $i = -(h + k)$ , for example, the  $(110)$  surface would be referred to as  $(11-(1+1)0)=(11\bar{2}0)$ , since the minus is expressed by the overbar. The advantage of this notation is, that one can identify symmetry-equivalent planes easily.

To express a direction vector in the basis of the direct lattice vectors, the notation  $[uvw]$  is used. In general this vector is not perpendicular to the plane  $(uvw)$ , only for cubic lattice this is the case. **TODO: seems to be out of context?**

To describe a periodic system with quantum mechanical methods, one has to introduce periodic boundary conditions. This includes that the periodicity of the nuclei is reflected by the periodicity of the effective potential  $v_{eff}$ , which has to be the same in all cells that are given by  $\underline{\mathbf{B}}$ :

$$v_{eff}(\underline{\mathbf{r}}) = v_{eff}(\underline{\mathbf{r}} + \underline{\mathbf{B}}). \quad (1.12)$$

According to the Bloch theorem the wave function value at equivalent positions in different cells are related to each other with a phase factor in the lattice vector  $\underline{\mathbf{t}}$ :

$$\phi(\underline{\mathbf{r}} + \underline{\mathbf{t}}) = e^{i\underline{\mathbf{k}} \cdot \underline{\mathbf{t}}} \phi(\underline{\mathbf{r}}) \quad (1.13)$$

In this equation the crystalline orbital  $\phi$  for the  $n^{\text{th}}$  band can be understood as having one wave-like and one cell periodic part  $\varphi$ , also known as Bloch orbital:

$$\phi_{n,k}(\underline{\mathbf{r}}) = e^{i\underline{\mathbf{k}} \cdot \underline{\mathbf{r}}} \varphi_n(\underline{\mathbf{r}}). \quad (1.14)$$

## 1. Theory und Methodology

Bloch orbitals can be expanded as a set of plane wave functions ( $\chi^{\text{PW}}$ ). Solutions are now dependent on the reciprocal space vector  $\underline{k}$  leading to a Roothaan-Hall expression:

$$\underline{\mathbf{F}}^k \underline{\mathbf{C}}^k = \underline{\mathbf{S}}^k \underline{\mathbf{C}}^k \underline{\varepsilon}^k \quad (1.15)$$

The solutions give a band (range of energies) and are a continuous function. For the total energy per unit cell one has to integrate over the  $\underline{k}$ -space. For non-metallic systems the integration can be done numerically using only a few points [14]. In analogy to molecular HOMO orbital, the energy of the highest filled band is called Fermi energy. The band gap, equivalent to HOMO-LUMO gap, is between the highest filled and the lowest empty band. In metallic systems, there is no bandgap, whereas in insulating systems the band gap is large **value?**.

As was raised before basis functions within a unit cell can be either delocalized in the form of plane waves or localized as a Gaussian basis set.

### 1.3. Plane Wave Basis, Atom Centered Basis and Peculiarities

In comparison plane waves (PW) and atom centered orbitals (ACO) have different advantages and disadvantages [15]. For solid state systems both the energy and the gradient converge faster with plane waves. Additionally, the calculation of atomic forces is simpler because only Hellmann-Feynmann forces have to be evaluated. The quality of the basis is simply dependent on the cutoff energy  $E_{\text{kin}}$ , the higher this energy is, the better is the basis. On the negative side, when norm-conserving pseudopotentials are applied more memory is needed. Pseudopotentials are used, when core electrons are not treated explicitly but their presence is considered for indirect. To treat this, the PAW (projector augmented-wave method) is applied which gives explicit treatment of the core electrons so that the accuracy is greatly increased. The system is intrinsically defined in 3D, no matter if the system is a 1D (polymer), 2D (surface) or 3D system (bulk). It is computationally demanding to calculate exact (Fock) exchange, which makes the use of hybrid functionals so costly, although the precision of the results is considerably enhanced.

Whenever there are atom centered basis sets the orbitals can overlap and due to this electrons are considered multiple times. This is called Basis Set Superposition Error (BSSE) and only appears in atom centered cases. One can apply Counterpoise corrections to get rid of this source of error. This is done here by calculating ghosted calculations with the system as a whole, the adsorbate alone, and the adsorbate with surface from ghost atoms. Then one applies a subtractive scheme to cancel out the effect of the orbital overlap. On the other hand one can use a huge basis set, that doesn't have this problem, which comes with a higher

## 1.4. *Ab Initio* Molecular Dynamics

computational demand. In contrast to PW calculations due to the locality of the basis, the true dimensionality is obeyed. Probably, the biggest advantage of atom centered bases is that exact exchange and hybrid methods are standard methods. Transferring atom centered bases to periodic systems is not trivial, especially for bases including many diffuse Gaussians.

### 1.4. ***Ab Initio* Molecular Dynamics**

Apart from solving stationary problems, *Ab initio* Molecular Dynamics (AIMD) can deliver results for time dependent processes [12,16]. This is necessary for simulating transport/diffusion processes as well as spectral properties. For this, Newton's equation of motion is solved:

$$-\frac{\partial V(\underline{\mathbf{R}})}{\partial \underline{\mathbf{R}}(t)} = M_A \frac{d^2 \underline{\mathbf{R}}_A(t)}{dt^2} \quad (1.16)$$

with the potential energy  $V$  that is a function of all nuclear coordinates  $\underline{\mathbf{R}}$ , the vector  $\underline{\mathbf{R}}_A$  that contains all coordinates of atom  $A$ , the atomic mass  $M_A$  and the time  $t$ . This equation gives in principle  $F = M_A \cdot a$ , the force  $F$  acting on each atom in a classical ansatz with the velocity  $a$ . This is a good approximation for nuclei are usually sufficiently massive to be treated classically. Strictly speaking, this is not sufficient for hydrogen, since it is so lightweight, that quantum mechanical tunneling processes can not be excluded. For treating quantum effects like zero point energy and tunneling one would have to solve the nuclear Schrödinger equation.

In comparison to classical Molecular Dynamics, where predefined potentials or force fields based on either empirical data or further electron structure methods are used, *ab initio* MD calculates the potential and the respective (Hellmann-Feynman) forces “on-the-fly” at each time step. This has the advantage, that no further parameterization has to be done when changing atoms or molecular groups/surfaces etc. Also a change in electron structure along the trajectory can be compensated without the necessity of another potential/force field to describe interatomic interactions.

As starting conditions, positions and momenta of the atoms have to be given. Between two time steps of the propagation there is a time span  $\Delta t$ . The time propagation can be done with the Verlet algorithm [17] numerically, delivering the trajectory  $\underline{\mathbf{R}}(t)$ :

$$\underline{\mathbf{R}}_A(t + \Delta t) = \underline{\mathbf{R}}_A(t) + \underline{\mathbf{v}}_A(t) \cdot \Delta t + \frac{1}{2} \underline{\mathbf{a}}_A(t) \cdot \Delta t^2 + \dots \quad (1.17)$$

$$\underline{\mathbf{R}}_A(t - \Delta t) = \underline{\mathbf{R}}_A(t) - \underline{\mathbf{v}}_A(t) \cdot \Delta t + \frac{1}{2} \underline{\mathbf{a}}_A(t) \cdot \Delta t^2 \pm \dots \quad (1.18)$$

## 1. Theory und Methodology

the previous and next time steps are approximated by a Taylor expansion with the velocity  $\underline{\mathbf{v}}_A(t)$  of atom A (the derivative of the coordinates with respect to time  $t$ ,  $\frac{\partial \underline{\mathbf{R}}_A}{\partial t}$ ), the acceleration  $\underline{\mathbf{a}}_A(t) = \frac{\partial^2 \underline{\mathbf{R}}_A}{\partial t^2}$ . With equations 1.17 and 1.18 one can predict the positions at a later time step from the current and the previous positions and the acceleration:

$$\underline{\mathbf{R}}_A(t + \Delta t) = (2\underline{\mathbf{R}}_A(t) - \underline{\mathbf{R}}_A(t - \Delta t)) + \underline{\mathbf{a}}_A(t)(\Delta t)^2 + \dots \quad (1.19)$$

with the acceleration, that must be evaluated at each time step from the potential (gradient of the forces):

$$\underline{\mathbf{a}}_A(t) = -\frac{1}{M_A} \frac{dV}{d\underline{\mathbf{R}}_A}. \quad (1.20)$$

This allows for the time propagation that gives the trajectory.

The time step  $\Delta t$  is an important parameter, it has to be small enough to describe the fastest processes of interest. Therefore it is typically around  $10^{-15}\text{s}$ , for example a molecular vibration of  $3000\text{ cm}^{-1}$  corresponds to  $\approx 10^{14}\text{s}^{-1}$ . On the other hand, a sufficiently long time has to be propagated to measure all chemically relevant processes, usually  $10^{-9}\text{s}$ . The smaller the time step the more accurate the simulation gets, but with decreased time steps, one has to propagate longer to gain the same duration, which increases the computational time drastically. Additionally, it may be necessary to compute several trajectories instead of just a single one, for reasonable averaging. *TODO: da gibt es doch ein Theorem*

The simulations are characterized by the following parameters: the total energy E, the temperature T, volume V, pressure p, the number of particles N and the chemical potential  $\mu$ . Not all of these are independent, either V or p can be constant. The corresponding ensemble is named after the fixed quantities, *e.g.* NVT (=canonical) and NVE (=microcanonical).

In a microcanonical ensemble (NVE) the system is isolated (it can not exchange particles or energy with the surroundings) and the total energy  $E$  is fixed. Computationally, it can be implemented easily. In experiments usually not the energy but the temperature are controlled. In contrast to that in a canonical ensemble (NVT) the system is coupled / in thermal equilibrium with a heat bath, also referred to as thermostat.  $T$  (on average) is given by the temperature of the thermostat. For this thermostat, several models are available, in this work the Nosé-Hoover thermostat [18–20] is used. The energy accounting of the heat bath is realized by a fictitious particle, that is propagated like real particles of the system and acts like a reservoir of energy for the heat bath. The total energy of the extended system is again a conserved quantity and therefore a control parameter.

## 1.5. Frequencies and Intensities

A characteristic of stationary points on the potential energy surface (PES) is, that the derivation with respect to all coordinates equals zero. For these points (minima and saddle points of first order) the eigenvalues and -vectors of the Hessian matrix  $\underline{\underline{H}}$  are of interest. The elements of this Hessian are the derivation of the potential with respect to coordinates:

$$H_{ij} = \left( \frac{\partial^2 V}{\partial Q_i \partial Q_j} \right)_{|Q_i=Q_j=0} = \left( \frac{1}{\sqrt{m_i m_j}} \frac{\partial^2 V}{\partial R_i \partial R_j} \right) \quad (1.21)$$

Here,  $Q_i$  are mass weighted coordinates  $Q_i = \sqrt{m_i} R_i$ , with the mass  $m_i$  and the displacement from the equilibrium position  $R_i$ . Then the matrix problem for the Hessian  $\underline{\underline{H}}$  has to be solved:

$$\underline{\underline{H}} \underline{\underline{A}}_i = \lambda_i \underline{\underline{A}}_i. \quad (1.22)$$

with the vectors of the normal modes  $A_i$  and  $\lambda_i$  being the squares of vibrational frequencies  $\omega_i$ :

$$\omega_i = \sqrt{\lambda_i}. \quad (1.23)$$

All frequencies are delivered in the harmonic approximation. One has to distinguish two physically relevant cases: all eigenvalues are positive ( $\lambda_i \geq 0 \forall i$ ) so the structure is a minimum on the PES. This could be the educt and product of a reaction. The second relevant case is if there is only one negative eigenvalue, that gives according to equation 1.23 one imaginary frequency, respectively. This is in a mathematical sense a saddlepoint of first order and can be interpreted as a transition state.

To calculate intensities there are several methods available with three being presented in this work:

- I) The IR intensities for each normal mode are estimated from the derivative of the dipole moment with respect to the atomic positions, also known as dynamical dipole moment [21]. Transition dipole moments of vibrations are determined by  $I \propto < i | \hat{\mu} | f >^2$ . For this approach, only the dipole components perpendicular to the surface are taken into account. Only these can be measured in respective SFG spectra. These are not completely comparable to IR spectra but IR sensitivity is next to Raman activity one of the selection rules for SFG. Additionally the process is only visible for interfaces (selection rules are shown in Appendix).
- II) Another way to get intensities is by calculating Born effective charges, as it was done in the work of Grillo *et al.* [22]. With the charges the dipole and also the intensities are

## 1. Theory und Methodology

available through  $\mu = \text{charge} \times \text{distance}$ , and again,  $I \propto \mu^2$ . Both methods are based on normal mode analyses and therefore give IR intensities.

While normal modes are a good approximation for high energy vibrations, for example OD stretch vibrations, it becomes worse for lattice vibrations, which are typically more delocalized.

- III) As a fundamentally different method, power spectra can be calculated from *ab initio* MD trajectories [23]. This is done by analyzing the velocity of the atoms along the trajectories, giving the vibrational spectrum via fast Fourier transformation of the velocity-velocity autocorrelation function:

$$VDOS(\omega) = \sum_{i=1}^N \int_{-\infty}^{+\infty} \langle v_i(t) \cdot v_i(0) \rangle e^{i\omega t} dt . \quad (1.24)$$

VDOS is the vibrational density of states,  $v_i$  are the velocities at different times and  $\omega$  is the frequency. The resulting spectra include implicitly anharmonic and quantum effects: No harmonic approximation for the potential energy surface and the modes are established and movement of the atoms are taken into account. Still, further anharmonic effects like mode coupling, overlapping of neighboring peaks and line broadening are missing [24, 25]. The power spectrum contains peaks for each normal mode vector apart from selection rules for vibrational spectroscopy. Intensities correspond to the oscillator amplitudes.

## 1.6. Finding Transition States

According to the Born Oppenheimer approximation [13] nuclear and electronic degrees of freedom are separated. In this picture, stable systems are minima on the PES and chemical reactions can be understood as nuclei, moving on the PES along the reaction coordinate  $\xi$ . On the N-dimensional surface, the energetically most favorable reaction path is chosen. This is the one with the least energy necessary (minimum energy path, MEP, see Figure 1.1). At the highest energy on this path it is called transition state. As mentioned before, it is a first-order saddle point, the energetically highest point along the reaction coordinate, but in all other coordinates a minimum.

Transition State Theory is a semi-classical theory: dynamics along the reaction coordinate  $\xi$  are treated classically, but perpendicular directions allow for quantization of vibrational and rotational energy. In thermodynamical equilibrium, all possible quantum states along the reaction coordinate are occupied with respect to their Boltzmann weight  $e^{\Delta E/(k_B T)}$ .

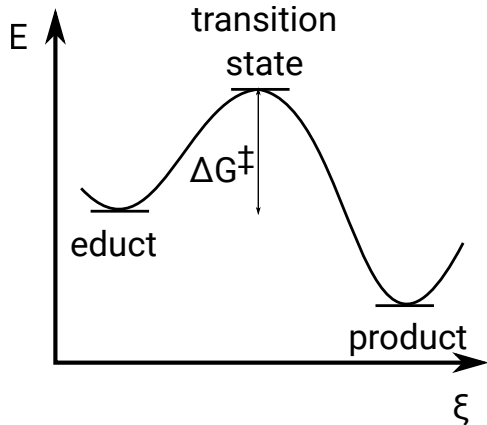


**Figure 1.1.:** Schematic view of a minimum energy path (MEP) for a thermal reaction.  $\Delta G^\ddagger$  for the reaction is also plotted.

Assuming the reaction



where reactants  $A$  and  $B$  are in thermodynamical equilibrium with the transition state  $C^\ddagger$  and this reacts to the product  $D$ . The rate can then be determined with Eyring theory:

$$k(T) = \kappa \frac{k_B T}{h} e^{\Delta G^\ddagger(T)/(k_B T)} \quad (1.26)$$

with the reaction rate constant  $k(T)$ , Boltzmann's constant  $K_B$ , the temperature  $T$ , the difference of Gibb's free energy for the transition state and the educt  $\Delta G^\ddagger = \Delta G_{TS} - \Delta G_{educt}$ , give the reaction rate constant as a function of temperature and free energy barrier height. Note, that this equation is only valid for cases, where all reactants that reach the TS react to the product site, *i.e.* no re-crossing is employed, so the rate is in the classical picture the upper limit. For quantum effects, the rate can be increased due to tunneling, where reactants can overcome the barrier although they do not possess the sufficient amount of energy for the barrier. For this, the Eyring equation can be expanded with the transmission coefficient  $\kappa$ , that can be interpreted as a tunneling prefactor, for  $\kappa > 1$  tunneling occurs and for  $\kappa < 1$  non-classical reflection or re-crossing to the educt side.

For the barrier height one needs to find the energies of the transition state and the educt. The educt geometry can simply be obtained by geometry optimization as a minimum on the PES. To find the transition state geometry and henceforth the energy we used Nudged Elastic Band calculations (NEB), with Climbing Image. The Reaction path is approximated as a series of associated images, which are connected via spring forces. These spring forces prevent the images from optimizing into the local minimum next to the transition state. First a

## 1. Theory und Methodology

regular NEB, then on top of this climbing image was done which gives better convergence. In this calculation the energetically highest image is "optimized" towards higher energies in the contrary direction of the gradient. For the point found by this scheme we checked whether this is a transition state via frequency analysis, since a TST of first order has to have one imaginary mode, that vibrates along the reaction path.

## 1.7. From Density Functionals to Hybrids and Perturbation Theory

### 1.7.1. Hybrid Functionals

In this work we also want to go beyond GGA (Generalized Gradient Approximation, here the PBE functional), because it is known from literature [26] to underestimate reaction rates. Since we are interested in reaction kinetics it therefore is desirable to use more sophisticated methods to improve the rates. The first approach applied here is using hybrid functionals, where a fraction of exact exchange is mixed into the potential. For this the exchange correlation functional is split up into two parts:

$$E_{xc}[n(\underline{\mathbf{r}})] = E_x[n(\underline{\mathbf{r}})] + E_c[n(\underline{\mathbf{r}})]. \quad (1.27)$$

The exchange part can be specified with a DFT part and HF with exact exchange:

$$E_x = aE_x^{HF} + (1 - a)E_x^{DFT}. \quad (1.28)$$

with the parameter  $a$ , that gives the amount of exact Hartree-Fock exchange. As an example, the functional B3LYP consists of 20% exact exchange.

$$E_{xc}^{B3LYP} = aE_{xc}^{LDA} + (1 - a)E_x^{HF} + bE_x^{B88} + cE_c^{LYP} + (1 - c)E_c^{LDA} \quad (1.29)$$

with  $a = 0.80$ ,  $b = 0.72$  and  $c = 0.81$ .

### 1.7.2. Møller Plesset Peturbation Theory

**TODO:** *difference of MP2 to local MP2?*

Another ansatz is using Local Møller Plesset Peturbation Theory [27] of 2<sup>nd</sup> order (LMP2) as implemented in crystal/crysco<sup>TODO: citations</sup>. These calculations are way more computationally demanding but offer better results on a higher level of theory. It offers more precise treatment of the dynamical electron correlation than DFT. The electronical Hamiltonian (here

### 1.7. From Density Functionals to Hybrids and Perturbation Theory

the subscript  $e$  is omitted) has already been solved exactly or approximately. The solution to the given problem is similar to the already known one. The reference system  $\hat{H}_0$  is perturbed by an external potential  $\hat{V}$ :

$$\hat{H} = \hat{H}_0 + \lambda \hat{V}. \quad (1.30)$$

$\hat{H}_0$  is the unperturbed Hamiltonian and  $\lambda$  a parameter, that determines the extent of the perturbation, but in general it is considered as “small”, compared to  $\hat{H}_0$ . The perturbed Schrödinger equation is given by:

$$\hat{H}\Psi = E\Psi. \quad (1.31)$$

If  $\lambda = 0$ ,  $E = E^{(0)}$  and  $\Psi = \Psi^{(0)}$  **TODO: then what?**. For higher values of  $\lambda$ , the energy and the wave function change and can be written by expanding the ground state wave function  $\Psi_0$  at  $\lambda = 0$

$$\Psi_0 = \Psi_0^{(0)} + \lambda \Psi_0^{(1)} + \lambda^2 \Psi_0^{(2)} + \dots, \quad (1.32)$$

the eigenvalues  $E_0$  can be determined analogously as:

$$E_0 = E_0^{(0)} + \lambda E_0^{(1)} + \lambda^2 E_0^{(2)} + \dots \quad (1.33)$$

The superscript  $E_0^{(n)}$  equals the correction of n-th level.

The unperturbed energy can be calculated with:

$$E^{(0)} = <\Psi^{(0)}|\hat{H}^{(0)}|\Psi^{(0)}> = \sum_{i=1}^N \varepsilon_i \quad (1.34)$$

and the energy of 1<sup>st</sup> order is:

$$E^{(1)} = <\Psi^{(0)}|\hat{V}|\Psi^{(0)}>. \quad (1.35)$$

$E^{(0)} + E^{(1)}$  equals the Hartree-Fock energy  $E_{HF}$ . For the energy of the second order, both occupied orbitals  $i, j$  and unoccupied orbitals  $k, l$  and their energy have to be considered:

$$E^{(2)} = \sum_i^{\text{occ.}} \sum_{j>i}^{\text{occ.}} \sum_k^{\text{unocc.}} \sum_{l>k}^{\text{unocc.}} \frac{(<ij|kl> - <ij|lk>)^2}{\varepsilon_i + \varepsilon_j - \varepsilon_k - \varepsilon_l} \quad (1.36)$$

The MP2-corrected total energy is composed of the HF energy and the second order energy:

$$E_{MP2} = E^{(0)} + E^{(1)} + E^{(2)} = E_{HF} + E^{(2)}. \quad (1.37)$$

The second order energy accounts for approximately 80 – 90% of correlation which makes it a highly feasible method that includes electron correlation. However, a main limitation of MP2

## 1. Theory und Methodology

is the wave function of the zeroth order is a good approximation to the real system and the perturbation is rather small. If the wave function describes the system poorly, the corrections have to be higher and eventually, convergence is slow. In this case perturbation theory might not be a good option to describe correlation.

## 1.8. Computational Details and Used Programs

Vasp4.x, 5.2 and version x (newer), crystal, cryscor **TODO: citations!**

For all the VASP calculations for the (0001) surface the parameters from prior work in our workgroup was used, like vacuum gap and convergence criteria, because these were converged carefully by Dr. Jonas Wirth [28–31]. Convergence was achieved when energies between two SCF steps was smaller then  $10^{-5}$  eV.

For (11 $\bar{2}$ 0) surface parameters were adopted and used as well. Also here the convergence criterion for the energy of two SCF cycles was  $10^{-5}$  eV.

For crystal and cryscor that were not used before for the calculation of alumina in our group the geometries from the VASP output were used as starting points and the usual convergence criteria of the programs were applied with some exception when convergence was hard to achieve.

## 2. Water on $\alpha\text{-Al}_2\text{O}_3(11\bar{2}0)$

### 2.1. Surface Model

The structure of  $\alpha$ -alumina has been well known for decades and was studied extensively (*e.g.* [32, 33]). It crystallizes in the hexagonal cell, that means  $\underline{a} = \underline{b} \neq \underline{c}$ , with an angle of 60° between the cell vectors  $\underline{a}$  and  $\underline{b}$ .

To obtain the clean surface slab model of the (11 $\bar{2}$ 0) surface a  $2 \times 2$  supercell was cut from the bulk. The corresponding cell vectors were adopted from the bulk structure and a vacuum gap in z-direction (perpendicular to the surface) was introduced to avoid unphysical interaction between the slabs in z-direction. In Figure 2.1(a) apart from the (11 $\bar{2}$ 0) surface the (0001) surface that is also studied in this work can be seen. Figure 2.1(b) shows the top view and the cell vectors  $\underline{a}$  and  $\underline{b}$  of (11 $\bar{2}$ 0). They are not equal to those in the hexagonal cell, but  $\underline{a} = 10.36\text{\AA}$ ,  $\underline{b} = 14.16\text{\AA}$  and  $\underline{c} = 20.5\text{\AA}$ . The angle  $\theta$  between  $\underline{a}$  and  $\underline{b}$  is 84.56° unlike the 60° since the (11 $\bar{2}$ 0) surface is tilted with respect to the top crystal plane. The nomenclature and color code of the surface Al and O atoms is also shown: The Alumina atoms have the same number of oxygen neighbor atoms but differ slightly in the arrangement of their neighbors and the distance in the relaxed structure, whereas the oxygen atoms in fact differ by the number of neighbors. In this work, the black spheres denote the CUSb atoms, the grey ones depict the CUSA. The twofold coordinated oxygen atoms ( $\text{O}-\mu_2$ ) are shown in yellow and the threefold coordinated ( $\text{O}-\mu_3$ ) in red. Atoms of the underlying layers are illustrated in pale colors, light grey for alumina and pale red for oxygen.

The unit cell consists of 5 atomic layers in z direction ( $\text{O}-\text{O}_2-\text{Al}_4-\text{O}_2-\text{O}$ ), see Figure 2.1(c)). The spacing between these layers in the relaxed structure and in the bulk crystal is slightly changed as given in Table 2.1. A major issue of the optimization apart from layer spacing is that the interatomic distances of Al species change: the inter-CUSA–inter-CUSA distance increased from 2.682 to 2.994 $\text{\AA}$ , the inter-CUSA–CUSb distance increased from 2.833 to 2.876 $\text{\AA}$  whereas the CUSb–CUSb distance decreased from 2.682 to 2.499 $\text{\AA}$ .

The supercell that is mostly used in this work has 10 atomic layers, with the lowest 5 fixed to the bulk value to mimic the surface situation. For the calculation of the lattice vibrations up to 25 layers were considered (Figure 2.2). For each slab size the respective lowest 5 layers

## 2. Water on $\alpha\text{-Al}_2\text{O}_3(11\bar{2}0)$

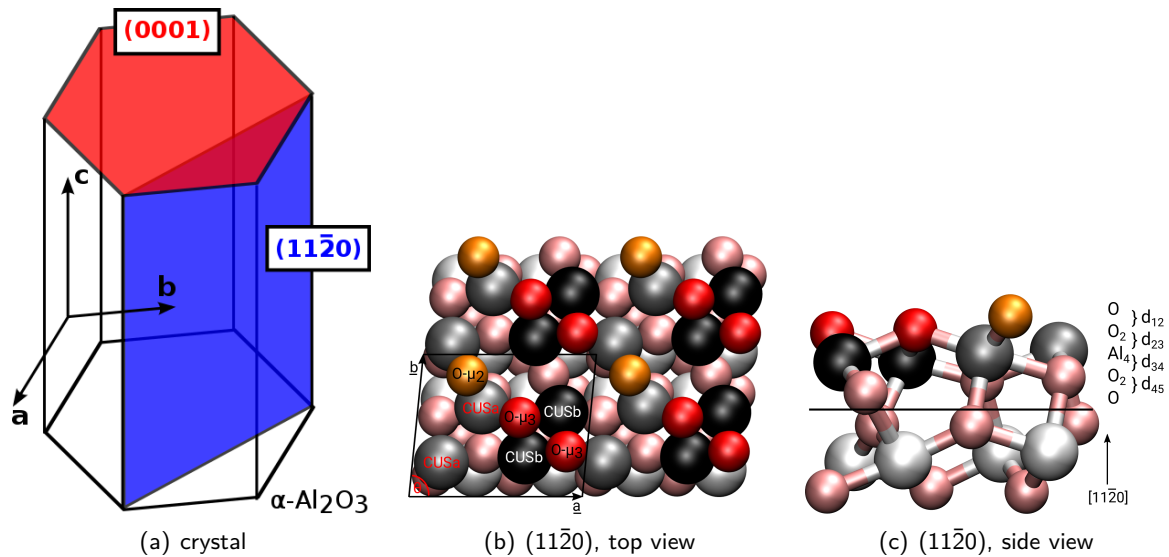


**Figure 2.1.**: The crystal cut of  $\alpha$ -Al<sub>2</sub>O<sub>3</sub>, (a) schematic view compared to the (0001) surface, (b) a top view of the geometry optimized  $2 \times 2$  super cell with the nomenclature of the surface atoms. The two types of surface Al atoms (grey CUSa and black CUSb) as well as the twofold and threefold coordinated oxygen atoms (orange O- $\mu_2$  and red O- $\mu_3$ ). Subsurface atoms are indicated by pale colors. (c) gives the side view of the unit cell showing the distinctive atomic layers with the same color code.

were kept fixed, see chapter 2.4.1. The spacing between the 5 top layers for each slab size is displayed in Table 2.1.

**Table 2.1.:** Distances between the top 5 layers (see also numbering in Figure 2.1(c)) for different optimized slab sizes and the unrelaxed bulk structure (right column). All values are given in Å.

distance	total number of atomic layers				bulk
	10	15	20	25	
d <sub>12</sub>	0.232	0.234	0.247	0.245	0.193
d <sub>23</sub>	0.642	0.649	0.638	0.639	0.741
d <sub>34</sub>	0.656	0.655	0.671	0.672	0.741
d <sub>45</sub>	0.198	0.205	0.209	0.213	0.191

k-point tests were done for 5 different grid sizes from  $1 \times 1 \times 1$  to  $5 \times 5 \times 1$ . In contrast to the even grid sizes, the odd ones contain the  $\Gamma$ -point and therefore are favorable. It can be deduced from Figure 2.3 that the  $3 \times 3 \times 1$  grid is already converged with respect to the energy of the clean surface.

Starting from the  $2 \times 2$  supercell approach of the clean surface there are 16 CUS Al-atoms (Coordinatively Unsaturated Sites). These have fewer bonds than the aluminum atoms in

## 2.1. Surface Model

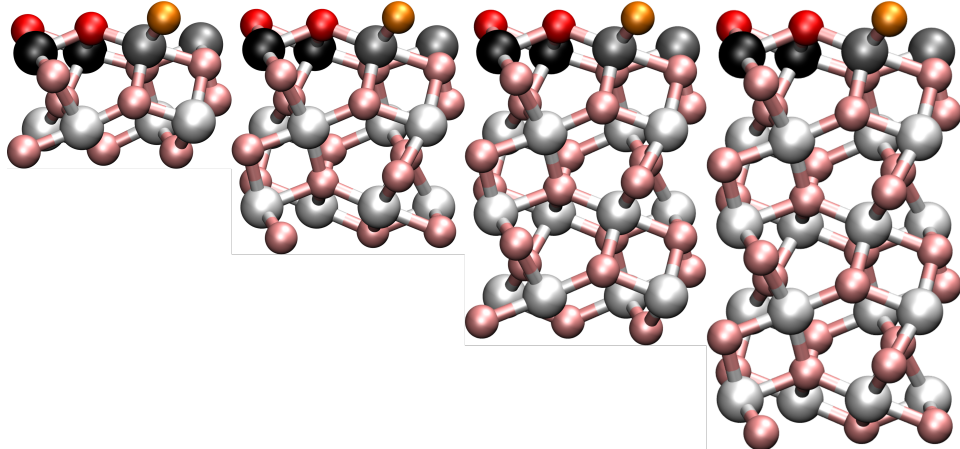


**Figure 2.2.:** Side view for the different cell sizes for 10, 15, 20 and 25 layers in z-direction. Surface atoms are shown in the color code clarified before.

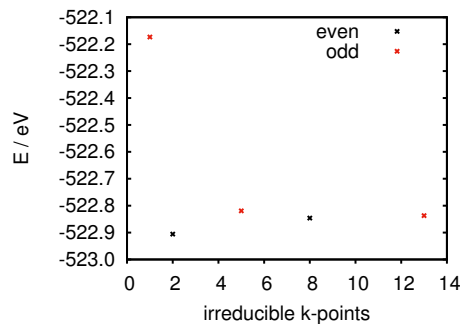


**Figure 2.3.:** Sampling of the  $\mathbf{k}$ -points, shown is the energy of the optimized super cell with respect to the number of irreducible  $\mathbf{k}$ -points. The even values correspond to the  $2 \times 2 \times 1$  (2 irreducibles) and  $4 \times 4 \times 1$  (8 irr.), whereas the odd, which contain the  $\Gamma$ -point, are described by  $1 \times 1 \times 1$  (1 irr.),  $3 \times 3 \times 1$  (5 irr.) and  $5 \times 5 \times 1$  (13 irr.).

the bulk structure since the surface layer is depleted. These atoms are very interesting for adsorbate molecules/atoms, because these surface atoms are electron rich and can be addressed for adsorption. Theoretically, these 16 atoms could be covered with adsorbates (in this work water) to gain 1 mono layer (ML). As will be shown shortly, water can not adsorb on all 16 Al CUS simultaneously to get 1ML. Of these 16 CUS atoms eight are CUSA and eight CUSb. On top of CUSb, a water molecule/OH residue can adsorb, but on top of a CUSA the adsorbate roams to an bridging inter-CUSA position between two CUSA. Due to this the number of potential adsorbates is decreased to 12.

## 2. Water on $\alpha\text{-Al}_2\text{O}_3(11\bar{2}0)$

### 2.2. Structure Search

To study water adsorption, first a low coverage regime was investigated: 1 water molecule per  $2 \times 2$  supercell, which equals a coverage of 1/12. The procedure was the following: put molecular water at different positions on the surface and let it relax. By doing this one molecular minimum and several dissociated species including both CUS and oxygen types were found. This multitude of different surface atoms gives rise to a large variety of possible adsorption geometries. Adsorption energies and Gibb's free energy of the resulting next neighbor species can be seen in Table 2.2. The nomenclature for the adsorption sites that is used in the following gives at first the type of Al site where the OH-residue ( $/\text{OH}^-$ ) is adsorbed and at second place the oxygen type where the H( $/\text{H}^+$ ) is adsorbed (OH-site||H-site). The term "inter" that is used in the following characterizes a position between two CUS atoms and leads to a bidentate adsorption pattern. The additional notation with ' denotes greater distances between the residues. There is also one metastable molecular species that appears to be more stable than the found molecular minimum considering adsorption energy, but it cannot be classified as a stable minimum since there is one imaginary mode displaying the movement of the proton towards the dissociated species.

The adsorption energy is defined by Equation 2.1 as the energy of the adsorbed system compared to the energies of the clean surface and the isolated water molecule:

$$E_{\text{ads}} = E_{\text{ads. species}} - (E_{\text{free water molecule}} + E_{\text{surface}}). \quad (2.1)$$

**Table 2.2.:** For molecular and (singly) dissociated water on  $\alpha\text{-Al}_2\text{O}_3(11\bar{2}0)$  adsorption energies  $E_{\text{ads}}$  and Gibb's free energy  $G_{\text{ads}}$  for different temperatures are given in eV.  $E_{\text{ads}}$  was calculated from Equation 2.1 and  $G_{\text{ads}}$  is defined analogously. These results were obtained with PBE+D2. The three most stable configurations are marked with bold letters.

Adsorbed Species		$E_{\text{ads}}$	$G_{\text{ads}, 130 \text{ K}}$	$G_{\text{ads}, 300 \text{ K}}$	$G_{\text{ads}, 400 \text{ K}}$
molecular	CUSb	-1.78	-1.60	-1.51	-1.46
	<b>inter-CUSa  O-<math>\mu_2</math></b>	<b>-2.50</b>	-2.27	-2.16	-2.09
	inter-CUSa  O- $\mu_3$	-1.67	-1.44	-1.33	-1.27
	<b>CUSb  O-<math>\mu_2</math></b>	<b>-2.28</b>	-2.12	-2.03	-1.97
	CUSb  O- $\mu_3$	-1.19	-1.05	-0.98	-0.95
	<b>inter-CUSb  O-<math>\mu_2</math></b>	<b>-2.09</b>	-1.88	-1.80	-1.76
	inter-CUSb  O- $\mu_3$	-1.89	-1.71	-1.63	-1.58

The molecular minimum is substantially less stable than the dissociated species. On the contrary, the dissociated water is very stable, even in comparison to the more stable surface cuts

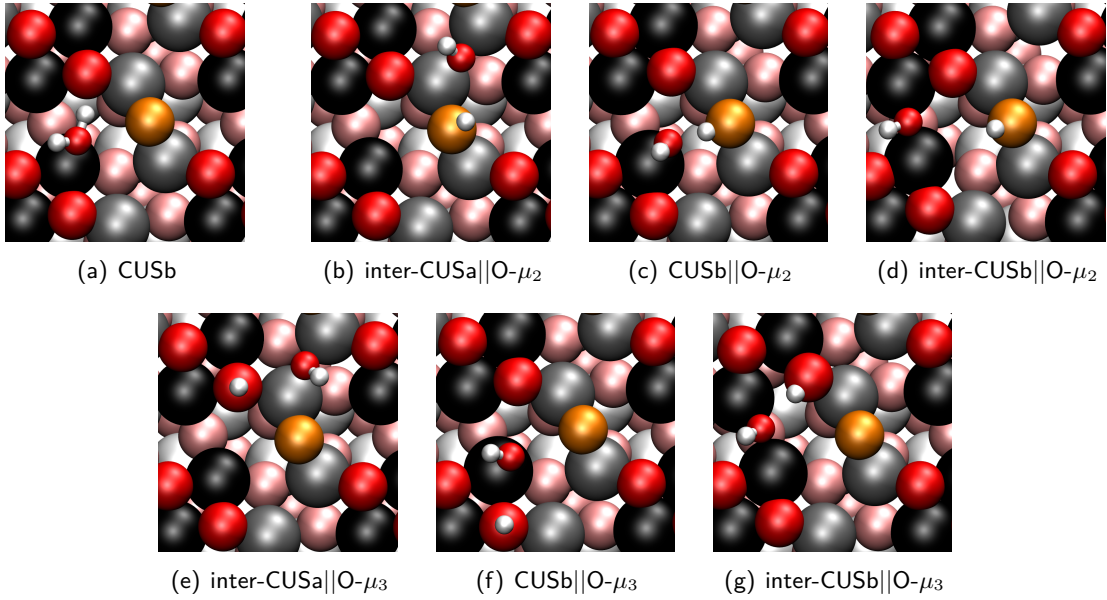


**Figure 2.4.:** Top view of the adsorption geometries for molecular CUSb (a) and the next neighbor dissociated water ((b)-(g)). The color code is the same as in Figure 2.1(b) and (c), CUSa grey, CUSb black, O- $\mu_2$  yellow and O- $\mu_3$  red; Hydrogen is illustrated in white; subsurface layers are shown in pale colors.

(0001) and (1̄102) that were previously investigated in our group by Dr. Jonas Wirth [28, 31]. Dissociated species, where the proton is located at a twofold coordinated surface oxygen are far more stable than the corresponding systems where the threefold coordinated is occupied. This is due to the higher negative charge and the higher basicity of such a twofolded oxygen atom in comparison with the more saturated threefold coordinated O- $\mu_3$  oxygen atom. In fact, the adsorption can be seen as a Lewis acid / base reaction [34] with the Lewis acid character of the undercoordinated aluminum and the base character of the oxygen from the water molecule. The adsorption of OH at an inter-CUSA site is more favorable than at a CUSb site, because the former corresponds to a site where in the bulk system another oxygen atom would be situated, which is not the case for the CUSb position. Additionally, the CUSb position is electronically and sterically more hindered because of the two threefold coordinated oxygen atoms in the surroundings.

Dissociated species in direct neighborhood as shown in Table 2.2 and Figure 2.4 are more stable than those where the proton and the OH residue are further apart (see Table 2.3), because the OH residue has a stabilizing effect on the H. It is apparent from this table that the inter-CUSb||O- $\mu_3''$ -species is more stable than the species inter-CUSb||O- $\mu_3''$ . This is due to the fact that the periodic conditions actually lead to a decrease of the distance between OH groups in

## 2. Water on $\alpha\text{-Al}_2\text{O}_3(11\bar{2}0)$

the former system. The distances between the neighboring OH groups in the  $\text{O}-\mu_3''$  system are 6.19 and 8.82 Å, compared to 6.64 and 8.96 Å in the  $\text{O}-\mu_3'''$  system (the numbers refer to the two possible distance in the periodic system, direct and over the border of the unit cell). The latter one is in fact only slightly further away, the average distance is 0.739 Å for inter-CUSb||O- $\mu_3''$  and 0.780 Å for inter-CUSb||O- $\mu_3'''$ . Although the distance is larger, there seems to be more stabilization TODO: mysterious.... For examples of the corresponding diffusion reactions, see chapter 2.3.

**Table 2.3.:** Comparison of adsorption energies for next neighbor dissociated species and dissociated species where OH and H are further apart. Results are given in eV.

Adsorbed Species	$E_{\text{ads}}$
inter-CUSA  O- $\mu_3$	-1.67
inter-CUSA  O- $\mu_3'$	-1.42
inter-CUSb  O- $\mu_3$	-1.89
inter-CUSb  O- $\mu_3''$	-1.16
inter-CUSb  O- $\mu_3'''$	-1.22

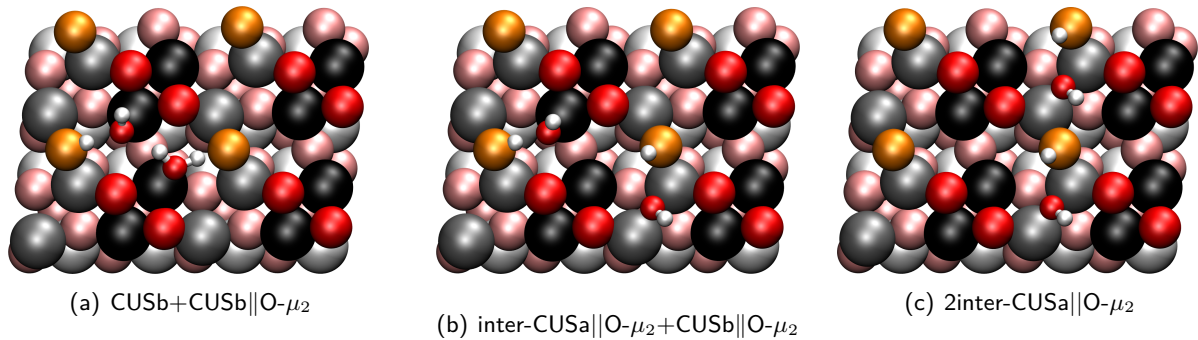
Apart from that, systems with additional atomic layers were studied to gain knowledge towards more realistic systems. The corresponding adsorption energies are shown in Table 2.4. Basically, the findings do not differ largely with increasing slab size. The molecular species still is less stable than the  $\text{O}-\mu_2$  dissociated species and is more stable than the  $\text{O}-\mu_3$  dissociated ones (except for inter-CUSb||O- $\mu_3$  dissociated system). inter-CUSA||O- $\mu_2$  is the most stable structure through all sampled systems sizes, inter-CUSb||O- $\mu_2$  and CUSb||O- $\mu_2$  change their stability (it approaches to nearly the same value for 25 layers) depending on the number of layers but still are some orders of magnitude less probable than inter-CUSA||O- $\mu_2$ . Dissociated systems occupying the threefold coordinated surface oxygen atom remain in the same stability order.

Table 2.4 shows that the most stable systems are already converged for the 10-layer slab with regard to adsorption energies (and also vibrational OH/OD frequencies as will be seen in section 2.4.1).

Furthermore, systems with a higher water coverage were considered to model enhanced systems, some cases for 2 water molecules (16.6% coverage), 4 inter-CUSA||O- $\mu_2$  (33.3% coverage) and a fully covered supercell (12 molecules, 100%), for these systems normal mode analyses were carried out to get vibrational spectra, see chapter 2.4.1. Structures can be found in Figures 2.15 and 2.6.

**Table 2.4.:** Adsorption energies calculated from equation 2.1 for molecular and dissociated species for different vertical slab sizes. All values are given in eV. The most stable systems (inter-CUSa||O- $\mu_2$ , CUSb||O- $\mu_2$  and inter-CUSb||O- $\mu_2$ ) are highlighted in bold letters.

System	10 layers	15 layers	20 layers	25 layers
CUSb	-1.78	-1.80	-1.81	-1.83
<b>inter-CUSa  O-<math>\mu_2</math></b>	<b>-2.50</b>	<b>-2.46</b>	<b>-2.54</b>	<b>-2.56</b>
inter-CUSa  O- $\mu_3$	-1.67	-1.67	-1.78	-1.80
<b>CUSb  O-<math>\mu_2</math></b>	<b>-2.28</b>	<b>-2.35</b>	<b>-2.36</b>	<b>-2.35</b>
CUSb  O- $\mu_3$	-1.19	-1.71	-	-
<b>inter-CUSb  O-<math>\mu_2</math></b>	<b>-2.09</b>	<b>-2.43</b>	<b>-2.48</b>	<b>-2.36</b>
inter-CUSb  O- $\mu_3$	-1.89	-1.59	-1.65	-2.09



**Figure 2.5.:** PBE+D2 optimized geometries of systems with two water adsorbates: (a) molecular CUSb and CUSb||O- $\mu_2$ , (b) the two most stable configurations inter-CUSa||O- $\mu_2$  and CUSb||O- $\mu_2$  and (c) 2 inter-CUSa||O- $\mu_2$ , which is the most stable adsorption pattern.

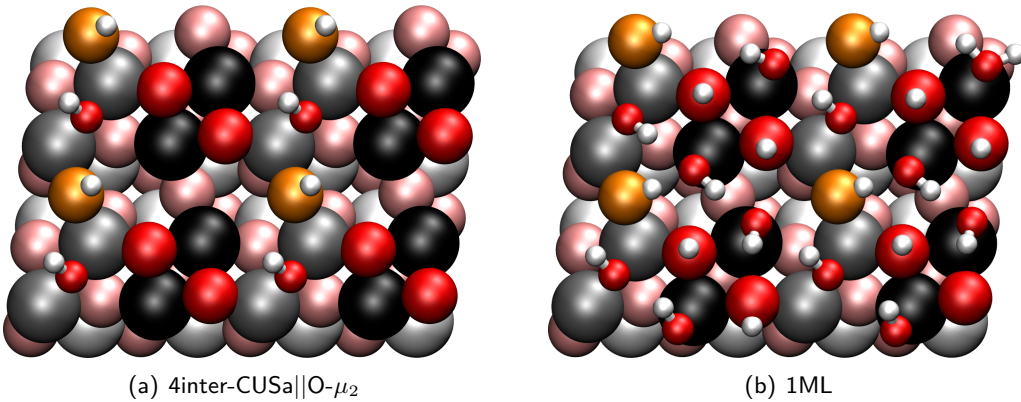


**Figure 2.6.:** Optimized structures of the (a) 4 inter-CUSa||O- $\mu_2$  and (b) fully covered (1ML) system. The latter one shows one molecular species and several hydrogen bonded OH groups.

## 2. Water on $\alpha\text{-Al}_2\text{O}_3(11\bar{2}0)$

The stability of those species with  $n$  adsorbed water molecules is defined as

$$E_{\text{ads}} = E_{\text{ads. species}} - (n \times E_{\text{free water molecule}} + E_{\text{surface}}). \quad (2.2)$$

In Table 2.5, the adsorption energies for the high coverage species mentioned above are given. There are also the results for the higher coverages in comparison to results in the low coverage

**Table 2.5.:** Adsorption energies for higher water coverages in eV. For better comparison in the third column labeled “isolated species” the added energies for singly adsorbed water as given in Table 2.2 are presented.

Adsorbed Species	$E_{\text{ads}}$	isolated species
CUSb(mol)+CUSb  O- $\mu_2$	-4.57	-4.06
inter-CUSA  O- $\mu_2$ +CUSb  O- $\mu_2$	-4.77	-4.78
2inter-CUSA  O- $\mu_2$	-4.84	-5.0
4inter-CUSA  O- $\mu_2$	-9.55	-10.0
12H <sub>2</sub> O	-23.39	<i>a</i>

*a* One can not distinguish exactly, but there are 4 inter-CUSA-OD groups, 8 CUSb-OD groups, 8 O- $\mu_3$  and 4 O- $\mu_2$  OD groups, hence one can not calculate a sum of the isolated species.

limit by adding them up (see also column 3 in Table 2.5). The neighborhood effect shows three different outcomes: it can have a stabilizing effect, where the dissociated water stabilizes the molecularly adsorbed water in CUSb(mol)+CUSb||O- $\mu_2$  (Figure 2.15(a)). It can also have the contrary effect, as can be seen in the 2inter-CUSA||O- $\mu_2$ , which becomes less stable (Figure 2.15(c)). On the other hand, there is the inter-CUSA||O- $\mu_2$ +CUSb||O- $\mu_2$  which is merely affected by the neighbor water residues (Figure 2.15(b)).

As a short excursus, also a “defect site”, the O-II terminated surface, as it is called in the nomenclature of Kurita [35], was calculated. This is the second most stable surface termination under most chemical potential conditions, mostly in Al-rich environment. In this termination, the topmost oxygen layer of the O-I termination is missing. As for the O-I termination, 10 layers were considered and from these the lowest five layers were kept fixed to bulk values. Both the clean surface and the fully covered (1 ML) surface were optimized (see Figure 2.7) and frequency calculations were conducted, to obtain a spectrum. The structure of the clean surface, of course, differs by the “missing” oxygen O- $\mu_2$  atom in the topmost layer, and the fully covered system is even more different: of 12 water molecules that can adsorb, 7 adsorb molecularly and 5 dissociatively. In comparison, the fully covered system for the O-I termination only shows one molecularly adsorbed molecule.

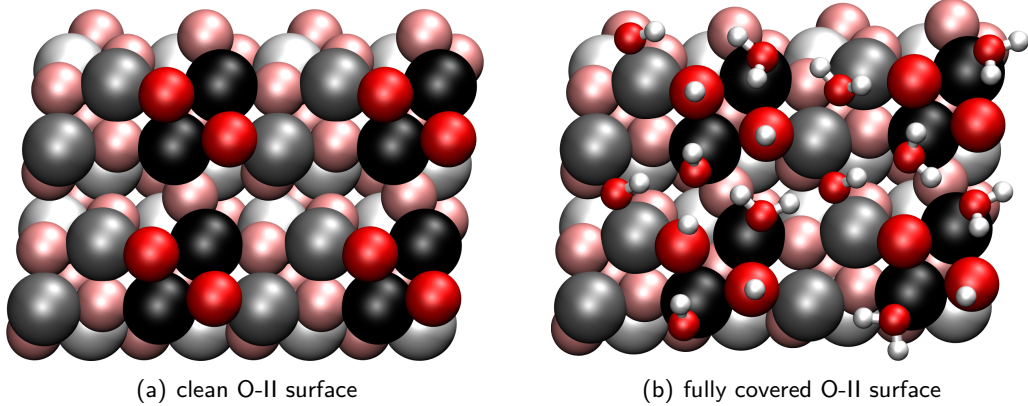


**Figure 2.7.:** O-II terminated surface, as an example of a defect site optimized with PBE+D2. The top layer oxygen atom from the O-I terminated surface is missing and gives rise to a different chemical behaviour. (a) clean surface, (b) 1ML water adsorbed surface.

### 2.3. Reactions and Microkinetic Model

*TODO: discrepancy between OD and Df-OH etc. this should be consistent! In fact paths and rates were calculated for H<sub>2</sub>O.*

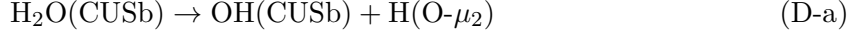
Based on the minimum structures one has to identify reaction pathways to fully understand the reactivity of a system. We utilize the NEB method including Climbing Image to search for transition states between the minima. We examined 3 different types of reactions: dissociation from the molecular minimum, as well as OH- and H-diffusion. The dissociation reactions are named D, diffusion reaction with Df-OH and Df-H, respectively, in Table 2.6 and figures 2.8 and 2.9. In addition, molecular water diffusion on the surface is supposed but due to the low stability, it will dissociate before diffusion can occur. In reference [36] only some reactions were introduced, additional reaction paths are given here.

We investigated 5 different dissociation reactions: the reactions from CUSb to the twofold coordinated oxygen (D-a) and one to the threefold coordinated O (D-b). One additional dissociation starts from the metastable inter-CUSA molecular structure that is, as was shown before, no minimum structure and goes to the most stable species inter-CUSA||O- $\mu_2$  (D-c). Two further dissociation reactions were converged but showed a two step process and are therefore not interesting in the first place (these reactions are CUSb $\rightarrow$ inter-CUSA||O- $\mu_2$  and CUSb $\rightarrow$ inter-CUSb||O- $\mu_2$  and both went via the dissociated CUSb||O- $\mu_2$  intermediate).

As can be seen from section 2.2 (Table 2.2), the molecular minimum CUSb is very low in stability compared to the dissociated minima. The reaction D-a leads from the molecular

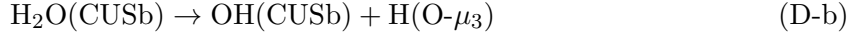
## 2. Water on $\alpha\text{-Al}_2\text{O}_3(11\bar{2}0)$

minimum at CUSb to the twofold coordinated CUSb $\parallel$ O- $\mu_2$ :

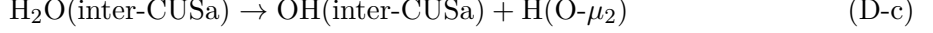


The barrier is very low, about 0.002 eV as one can see from Table 2.6 and Figure 2.8(a), hence the reaction rate constant is very high, in the range of  $k_{300\text{K}} = 10^{12} \text{ s}^{-1}$ . This low barrier might be due to underestimation of barrier heights [26] with the used functional PBE (compare section 1.7).

For the other dissociation reaction D-b from CUSb to CUSb $\parallel$ O- $\mu_3$ , there is no barrier found at all, the reaction pathway shows simply an upgoing path in energy without any barrier (see Figure 2.8(b)), since the molecular minimum is by 0.15 eV more stable than the dissociated structure on CUSb $\parallel$ O- $\mu_3$ . Thus, no reaction rate constant can be calculated.



A further dissociation D-c from the metastable inter-CUSA species also shows no barrier (without Figure), assumingly because the educt is no stable minimum and because the product is much more stable:



On the other hand reaction D-b does also not possess a barrier, so it remains unclear whether it is due to methodology and the barrier is too low to be detected with the settings applied for the calculations or for chemical reasons.

Apart from dissociation that is highly favored on this surface cut compared to more stable alumina surfaces [36], diffusion reactions starting from the dissociated species are important for understanding for further processes. The OD diffusion reaction Df-OH-a moves from CUSb $\parallel$ O- $\mu_2$  to the inter-CUSb position, which is relatively fast for OD diffusion reactions compared to the reactions at other alumina surfaces [28, 31].



In this special reaction, the OH residue diffuses from an on top CUS position into a gap between two CUSb atoms (inter-CUSb position), so that there is not much repulsion with neighboring surface oxygen atoms and other CUS atoms nearby during the diffusion, see Figure 2.8(c). Also the distance that has to be overcome is very small. The barrier height equals 0.35 eV and the corresponding rate constant  $k_{300\text{K}} = 1.88 \times 10^6 \text{ s}^{-1}$ . In contrast to that the real CUS-to-CUS

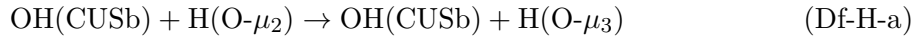
### 2.3. Reactions and Microkinetic Model

reaction Df-OH-b that is much slower. It is a diffusion from CUSb to inter-CUSA with the hydrogen residue staying at an O- $\mu_2$  position (see Figure 2.8(d)). This barrier is with 1.07 eV relatively high and leads to  $k_{300K} = 2.41 \times 10^{-6} \text{ s}^{-1}$ .



This is still faster than OH diffusion reaction for the (0001) alumina surface [28,37], where the rate constant  $k_{300K} = 4 \times 10^{-45} \text{ s}^{-1}$ . For the (1\bar{1}02) surface no OH diffusion was calculated, but the corresponding H<sub>2</sub>O diffusion process is around  $k_{300K} = 1.4 \times 10^{-3} \text{ s}^{-1}$ , whereas the H<sub>2</sub>O diffusion process for the (0001) surface is in the range of  $k_{300K} = 8 \times 10^{-3} \text{ s}^{-1}$ , too. For the (11\bar{2}0) surface no H<sub>2</sub>O diffusion reactions can be observed due to the instability of the molecularly adsorbed species that would rather dissociate than diffuse.

A larger variety can be achieved looking at H diffusion reactions. The different types of surface oxygen atoms and also the distances between OH and H residue make differences in the adsorption energy and also in the observed reactions. As seen before, the hydrogen is preferably found on the twofold coordinated oxygen atom, but the reaction to a neighboring threefold coordinated oxygen is possible and opens the gate to structures with greater distance. The reaction can take place with the OH residue being on a CUSb site:



The reaction shows a proton transfer reaction with a barrier height of 0.95 eV, but the NEB transition state has no imaginary frequency so that no rate can be derived, although the NEB path clearly shows a smooth barrier profile, compare Figure 2.9(a).

A further reaction starting from the most stable inter-CUSA||O- $\mu_2$  to the threefold coordinated oxygen can be seen in Figure 2.9(b) and is called reaction Df-H-b:



The barrier of the free energy is 1.50 eV, with a rate constant at 300 K of  $4.90 \times 10^{-13} \text{ s}^{-1}$ . This process is so unlikely because a less favored O- $\mu_3$  position is occupied and this position is also less stabilized by reason of the greater distance of OH<sub>surf</sub> and OH<sub>ads</sub> groups. This reaction increases the distance to a position further away than next neighbor. As mentioned before, the nomenclature for these structures uses primes ( $'$ ) to display the distance.

A similar reaction can be seen in Figure 2.9(c) for the OH being situated on inter-CUSb and the hydrogen being adsorbed on an O- $\mu_2^{(')}$  position, diffusing further away to O- $\mu_3^{''}$ , which is

## 2. Water on $\alpha\text{-Al}_2\text{O}_3(11\bar{2}0)$

less in stability:



The free energy barrier is relatively high with 1.30 eV giving a rate constant  $k_{300\text{K}} = 9.96 \times 10^{-1}\text{s}^{-1}$ . The ' in the equation above is set in parentheses because it is the nearest possible O- $\mu_2$  position, but not the nearest possible distance from the OH<sub>ads</sub>.

Going one step further from reaction Df-H-c, the following reaction leads to the position where OH and H have the greatest possible distance with the applied periodic bounding conditions:



With an energy barrier of 0.94 eV the rate at 300 K is  $1.1 \times 10^{-3}\text{s}^{-1}$ , see also Figure 2.8(d). These H diffusion paths can be assembled to a longer diffusion path leading from inter-CUSb||O- $\mu_3$  to O- $\mu_2'$  to O- $\mu_3''$  and to the furthest possible O- $\mu_3'''$ . The first reaction was calculated but did not converge for unknown reasons. The two next steps of this hydrogen migration path were studied (Df-H-c and Df-H-d). The rate of the first step is unknown but it is assumed to be fast, because as the product a very stable O- $\mu_2$  configuration is involved. The second reaction (Df-H-c) has a medium rate with  $10^{-1}\text{s}^{-1}$ . The last step of this path is the slowest with  $10^{-3}\text{s}^{-1}$ . The corresponding adsorption energy profile is different from that: -1.89, -2.09, -1.16 and -1.22 eV. One can conclude that hydrogen migration but not likely because the O- $\mu_2$  acts as a trap for H that hinders further reactions.

**Table 2.6.:** Energy and free energy differences are given:  $\Delta E = E(\text{product}) - E(\text{educt})$ ,  $\Delta E^\ddagger = E^\ddagger - E(\text{educt})$ , respective for  $G$ . The same is given for the transition state - educt. Thermodynamic properties are given at  $T = 300\text{ K}$ .  $k$  is the rate constant from eq. (1.26). The three types of reactions are dissociation (D), OH diffusion (Df-OH) and H diffusion (Df-H). "n.f." indicates "not found"

Reaction Type		$\Delta E$ (eV)	$\Delta G_{300\text{ K}}$ (eV)	$\Delta E^\ddagger$ (eV)	$\Delta G_{300\text{ K}}^\ddagger$ (eV)	$k_{300\text{ K}}(\text{s}^{-1})$
H <sub>2</sub> O dissociation	D-a	-0.50	-0.52	0.01	0.002	$5.76 \times 10^{12}$
	D-b	0.59	0.53	n.f.	n.f.	n.f.
	D-c	-1.15	-1.27	n.f.	n.f.	n.f.
OH diffusion	Df-OH-a	0.19	0.22	0.35	0.39	$1.88 \times 10^6$
	Df-OH-b	-0.21	-0.13	1.07	1.10	$2.41 \times 10^{-6}$
H diffusion	Df-H-a	0.76	0.58	n.f.	n.f.	n.f.
	Df-H-b	1.08	1.04	1.65	1.49	$4.90 \times 10^{-13}$
	Df-H-c	0.93	0.89	1.36	1.30	$9.96 \times 10^{-10}$
	Df-H-d	-0.06	-0.07	1.05	0.94	$1.05 \times 10^{-3}$

### 2.3. Reactions and Microkinetic Model

Proton diffusion reactions are way more variable than OH diffusions or dissociation reactions, providing reaction rates at 300 K ranging from  $10^{-13}$  to  $10^{-3}\text{s}^{-1}$ . The barriers and therefore also rate constants for H-diffusion cover a wider range depending on the distance between OH and H and of course more importantly on the fact between which types of O- $\mu_{2/3}$  the proton is diffusing.

Also reactions leading to another situation than next neighbored, increasing the distance between OH and H are less favorable since geometries with the residues further apart are energetically less stable (compare Table 2.3).

Rates for backreactions can also be calculated and the results are shown in Table 2.7.

**Table 2.7.: Reaction rate constants for the backreactions (right) in comparison with forward reactions (left). These rates can be calculated via detailed balance  $\frac{\leftarrow}{\rightarrow} k = k e^{-\Delta G/k_B T}$ . All values are given in  $\text{s}^{-1}$  at a temperature of 300 K.**

Reaction Type	$k_{300 \text{ K}}(\text{s}^{-1})$ forward reaction	$k_{300 \text{ K}}(\text{s}^{-1})$ back reaction
D-a	$5.76 \times 10^{12}$	$1.17 \times 10^4$
D-b	n.f.	n.f.
D-c	n.f.	n.f.
Df-OH-a	$1.88 \times 10^6$	$9.86 \times 10^9$
Df-OH-b	$2.41 \times 10^{-6}$	$1.69 \times 10^{-8}$
Df-H-a	n.f.	n.f.
Df-H-b	$4.90 \times 10^{-13}$	$1.49 \times 10^5$
Df-H-c	$9.96 \times 10^{-10}$	$9.95 \times 10^5$
Df-H-d	$1.05 \times 10^{-3}$	$7.12 \times 10^{-5}$

As mentioned before an immense well known problem of GGA is that barriers are underestimated [26]. Optimizing structures with HSE06 is nearly impossible due to high cost and doing single point calculations on PBE optimized transition state is not very accurate and doesn't deliver better results (unpublished work by Dr. J. Wirth, U Potsdam).

## 2. Water on $\alpha\text{-Al}_2\text{O}_3(11\bar{2}0)$

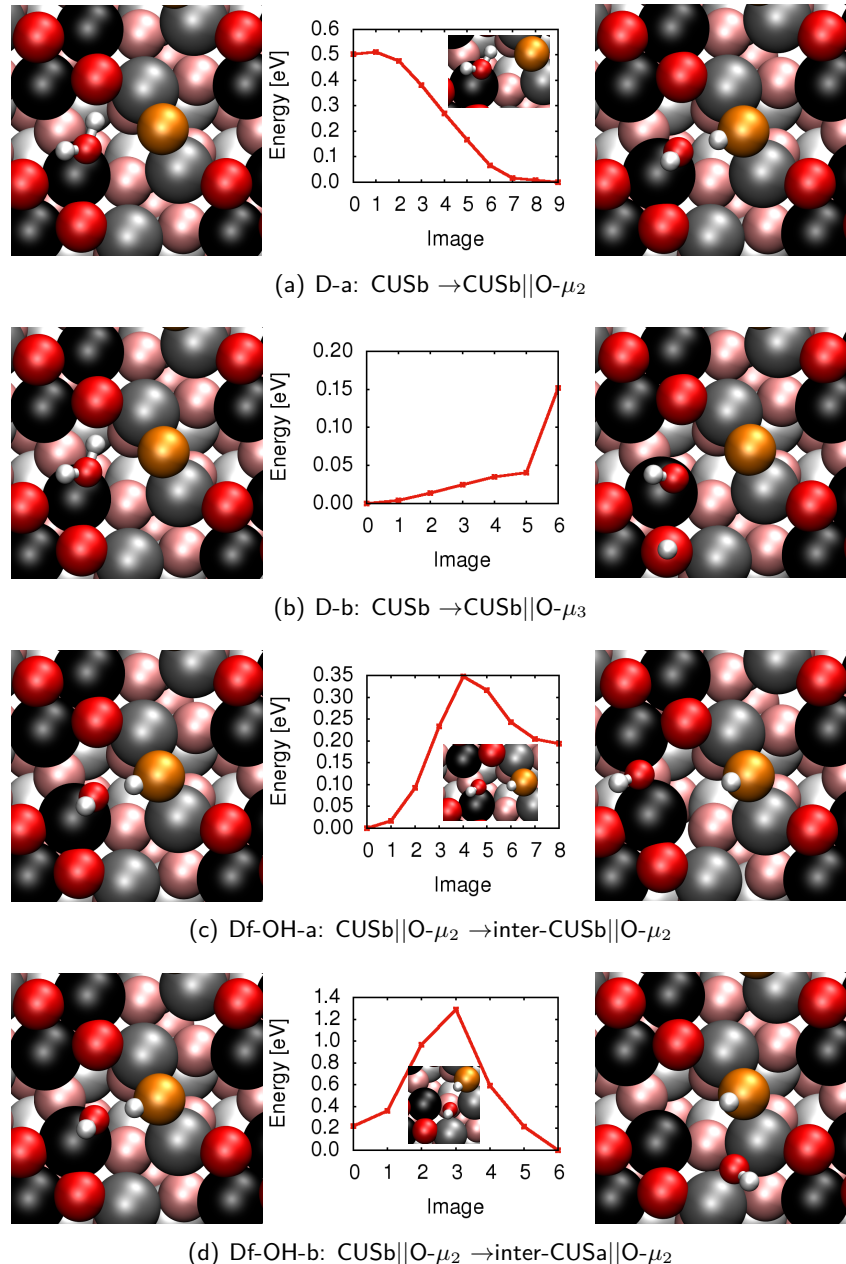


**Figure 2.8.:** Minimum energy paths with transition states (inlay; if available), and both educt (left) and product (right) states for D-a, D-b, D-c, Df-OH-a and Df-OH-b reactions, respectively. The color code is as explained above.

### 2.3. Reactions and Microkinetic Model

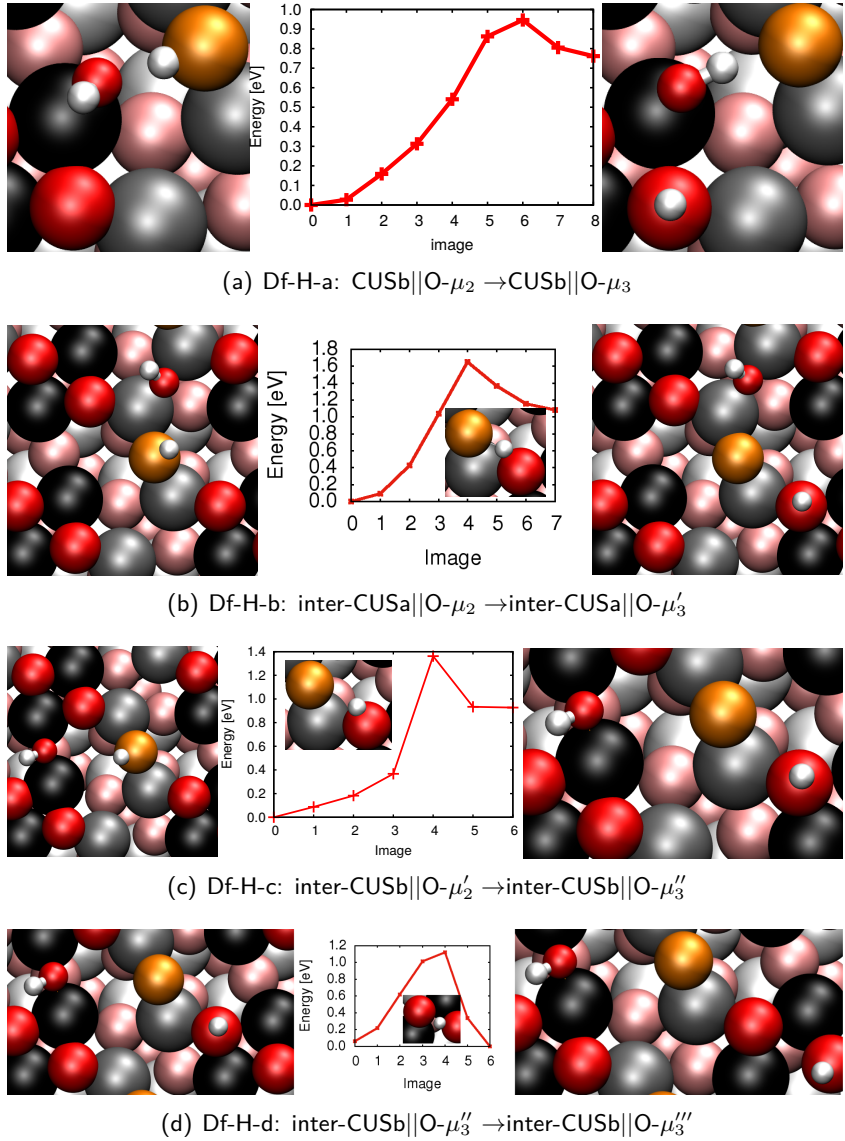


**Figure 2.9.:** Minimum energy paths with transition states, and both educt and product states for Df-H-a - Df-H-d reactions. The color code is as explained above.

## 2. Water on $\alpha\text{-Al}_2\text{O}_3(11\bar{2}0)$

### 2.4. Vibrational Frequencies

A great source of knowledge about chemical systems is vibrational spectroscopy, so we were interested in vibrational frequencies of the systems, since the frequencies of vibrations give us hints about the chemical environment as hydrogen bonds and other atoms nearby that bond to each other. These vibrational frequencies were calculated for the surface system adsorbed with OH and also with OD. Our experimental partners from FHI use deuterated water ( $\text{D}_2\text{O}$ ) instead of  $\text{H}_2\text{O}$  because the chemical reactivity is the same but the spectroscopic properties are clearer with their applied Laser system. The experimental SFG spectra (Sum Frequency Generation) for the OD range of the low coverage regime for two different coverages are shown in Figure 2.10 as they were published in [36]. Of course, the frequencies for a deuterated system

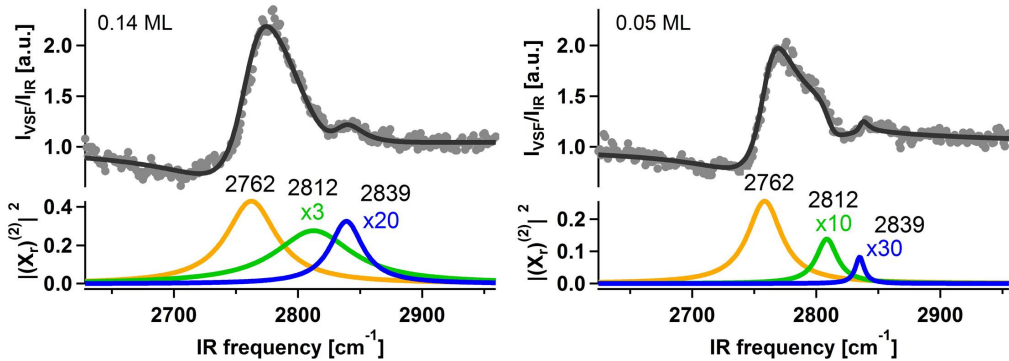


**Figure 2.10.:** Experimental SFG results for  $(11\bar{2}0)$  surface with 0.14ML (mono layer, left spectrum) and 0.05ML water coverage (right) including fit. The experiment was conducted by Yanhua Yue, FHI Berlin. Coverage only influences intensity of the peaks but not the peak position itself. The different coverages are achieved via different preparing temperatures of the sample.

are different from OH, but the different isotopes can be calculated easily within vasp, just by changing the mass.

In experiment the alumina single crystal was cleaned in ethanol and Milli-Q water and dried with  $\text{N}_2$  before being installed in the ultra high vacuum chamber. It was then sputtered in Ar, and annealed to high temperatures in UHV and afterwards three times in oxygen at different temperatures. After this treatment,  $\text{D}_2\text{O}$  was brought onto the surface with a molecular beam source. For further details see [36] and the supporting information therein.

To calculate the modes in this work mainly two methods were applied: Normal mode analyses (see section 2.4.1) and power spectra from *ab initio* MD via velocity-velocity autocorrelation function (section 2.4.3).

The focus lies mainly on the position of the peaks rather than the intensities, because in the

## 2.4. Vibrational Frequencies

first place it is of greater importance what kind of vibrations gives which peak than the intensity of the peak itself. Also, it is still challenging to determine the frequencies before heading to intensities. In the power spectra from MD calculations the intensities are implicitly received and for the normal mode analyses this work follows 2 different approaches: dipole corrections and Born effective charges.

In subsection 2.4.1, also modes for higher coverage systems are also examined.

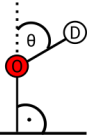
But not only the OD frequencies are of interest, but also the lattice vibrations, and are covered in both subsections.

### 2.4.1. Normal Mode Analysis

#### *OD Vibrations*

The normal modes are calculated within the harmonic approximation and depend on the mass and the spring constant of the bond. This ansatz is quite good for high frequency modes like OD stretch vibrations. We assumed that the OD stretching modes for the three most stable structures would contribute to the spectrum the most. These results are presented in Table 2.8.

**Table 2.8.:** Wavenumbers of normal modes for the different slab sizes: OD stretching modes for each of the most stable minima. All values are given in  $\text{cm}^{-1}$ ; in parantheses, the angle of the OD bonding vector to the surface normal ( $\theta$  in  $^\circ$ ) is provided. In each column, the left value reflects the adsorbed OD group and the right wavenumber the surface OD group, respectively. In the right part a sketch of the angle  $\theta$  between the OD bond and the surface normal is shown.

Layers	inter-CUSa  O- $\mu_2$	CUSb  O- $\mu_2$	inter-CUSb  O- $\mu_2$	
10	2731 (44), 2694 (36)	2785 (26), 1711 (61)	2692 (41), 2689 (54)	
15	2728 (44), 2695 (36)	2783 (24), 1812 (60)	2711 (34), 2656 (60)	
20	2729 (44), 2694 (35)	2783 (24), 1838 (60)	2715 (34), 2665 (58)	
25	2728 (44), 2696 (35)	2767 (59), 1750 (62)	2764 (29), 2724 (41)	
exp.		2839, 2812, 2762		

Following this approach we expect six modes, for each of the three an  $\text{OD}_{surf}$  and an  $\text{OD}_{ads}$ . In all cases the relationship between the two individual modes for each considered structure is portrayed by  $\tilde{\nu}(\text{OD}_{ads}) > \tilde{\nu}(\text{OD}_{surf})$ . This can be explained with the different reduced mass for both vibrations: The  $\text{OD}_{surf}$  oscillator has a slightly larger reduced mass since the deuterium is bound directly to the surface, whereas the adsorbed OD group can act more as a quasi-free OD group [29]. All these vibrations are clearly localized on one of the OD groups, which suggests that the normal modes ansatz is reasonable.

Of course, normal modes of all molecular and next neighbor dissociated structures from 10 to

## 2. Water on $\alpha\text{-Al}_2\text{O}_3(11\bar{2}0)$

the 25 slab layer model were calculated, although as it was mentioned in section 2.2 that the slab was already converged with 10 layers concerning OD stretch frequencies.

To consider the probability of observing these species, we calculated their respective Boltzmann weights  $P_i$ :

$$P_i = e^{-G_i/(k_B T)}. \quad (2.3)$$

With this analysis it is possible to show the relative population for different temperatures, given in Table 2.9. In the temperature range relevant for the experiments, it is shown that the population of the species inter-CUSA $\parallel$ O- $\mu_2$  clearly dominates and furthermore that the population of inter-CUSb $\parallel$ O- $\mu_2$  is very low, compared to the others.

**Table 2.9.:** Boltzmann population  $P$  relative to the most stable inter-CUSA $\parallel$ O- $\mu_2$ , calculated according to Equation 2.3 for 130, 300 and 400 K. Values are given for the 10-layer system.

	$P_{130K}$	$P_{300K}$	$P_{400K}$
inter-CUSA $\parallel$ O- $\mu_2$	1	1	1
CUSb $\parallel$ O- $\mu_2$	$1.4 \times 10^{-6}$	$6.1 \times 10^{-3}$	$3.2 \times 10^{-2}$
inter-CUSb $\parallel$ O- $\mu_2$	$1.0 \times 10^{-15}$	$1.2 \times 10^{-6}$	$6.6 \times 10^{-5}$

From the results for the frequencies of the three most stable structures (from Table 2.8), one can see, that for all slab sizes, there are 4 relevant modes to be expected. One of them is noticeable lower in energy that is due to hydrogen bonding (OD surface vibration of CUSb $\parallel$ O- $\mu_2$ ). Also the angle of the bonding vector with respect to the surface normal is very high (i.e. the bond is more in plain, values and schematic representation shown in Tab. 2.8) so that the expected intensity in experiment is remarkably lower and may be not visible in experiment because of the angle dependence of the intensity in VSF.

With this in mind, we are able to predict 3 peaks, which fits well to the experimental results of Yanhua Yue from FHI Berlin (see Figure 2.10). Comparing these results in absolute numbers is not very convincing as before in the literature, but relative numbers are in good agreement (see results for experiment and all different sized layer slabs in Table 2.10).

Two problems of this approach are, that we neglect anharmonicities, that are especially important for hydrogen bonded vibrations and also the absence of neighbor effects, that can be solved by computing higher coverage systems.

The influence of higher coverage was examined for some systems already presented in section 2.2. The coverage differs from 2D<sub>2</sub>O molecules per super cell to 4 and 12 water molecules which equals 1ML. Here the frequencies of the OD stretching modes are affected due to the

## 2.4. Vibrational Frequencies

**Table 2.10.:** Wave number differences  $\Delta\tilde{\nu}$  are given in [cm<sup>-1</sup>].  $\Delta\tilde{\nu}_1$  depicts the difference between the surface OD group of the inter-CUSA||O- $\mu_2$  species and the respective surface OD group on O- $\mu_2$  and  $\Delta\tilde{\nu}_2$  is the difference between the same surface OD group and the adsorbed OD group on CUSb from CUSb||O- $\mu_2$ .

layers	$\Delta\tilde{\nu}_1$	$\Delta\tilde{\nu}_2$
10	37	91
15	33	88
20	35	89
25	32	71
exp.	50	77

neighbor adsorbates, for some structures more and for other less (e.g. the system with 2 inter-CUSA||O- $\mu_2$ ). *TODO: compare modes of low coverage limit to spectra with higher coverage, ask Lu for more data of higher coverage.*

The simulation of intensities was done both with dipole corrections and Born effective charges and is shown in Table 2.11 as a comparison. The results are in reasonable agreement for inter-

**Table 2.11.:** Comparison of the IR intensities for the 10-layer system obtained from dipole corrected calculations and from the Born effective charges based approach. It was normalized to the highest intensity peak.

$\tilde{\nu}$ [cm <sup>-1</sup> ]	Intensity [a.u.]	
	dip.	BEC
inter-CUSA  O- $\mu_2$	2731	0.034
	2694	0.022
CUSb  O- $\mu_2$	2785	0.262
	1711	0.155
inter-CUSb  O- $\mu_2$	2692	0.007
	2689	0.060
		1.0
		0.072

CUSA||O- $\mu_2$  and inter-CUSb||O- $\mu_2$ , but are deviate largely for the hydrogen bonded CUSb||O- $\mu_2$  system. Corresponding “intensities” from AIMD calcualtions are presented in section 2.4.3. Frequencies for the low coverage limit were also calculated using the crystal code. This enables calculations with atomic centered bases and makes it possible to treat a real 2-D system without the need to calculate the repetition of the slab in z-direction, see also section 3.3.1. With this code it is also possible to calculate hybrid functionals easily, here B3LYP. For both PBE and B3LYP, geometries of the most stable states were reoptimized starting from VASP optimized geometries and consecutive normal modes were calculated (both with the basis set pob\_TZVP). Also anharmonicities for OH/OD bonds were calculated, these results are shown

## 2. Water on $\alpha\text{-Al}_2\text{O}_3(11\bar{2}0)$

in comparison with VASP results in Table 2.12. First, PBE results from both programs do not differ largely. Anharmonicities decrease the wavenumbers and lead to worse agreement to experiment (2839, 2812 and 2762  $\text{cm}^{-1}$ ) and to VASP calculations. Data from B3LYP calculations show great agreement with experiment, although here, anharmonic corrections make the agreement worse, too. This effect can be caused by error cancellation. One has to mention, that here influence of the basis set is strong and larger basis sets were not feasible due to high computational costs.

**Table 2.12.:** Stretch wavenumbers in  $\text{cm}^{-1}$  for both of the OD groups at the  $(11\bar{2}0)$  surface (10 atomic layers) for the 3 most stable species, calculated with atom centered basis functions with the program crystal. Frequencies were calculated at the B3LYP+D3 and PBE+D3 level of theory, optimized with the respective method. As a basis pob\_TZVP was used. The VASP results were obtained with a plane wave basis and PBD+D2 corrections. The short notation for inter-CUSa||O- $\mu_2$  (iCa2), CUSb||O- $\mu_2$  (Cb2) and inter-CUSb||O- $\mu_2$  (iCb2) were used.

stretch	PBE		B3LYP		VASP result
	$\tilde{\nu}$	$\tilde{\nu}$ +anharm	$\tilde{\nu}$	$\tilde{\nu}$ +anharm	
iCa2: OD <sub>surf</sub>	2682	2599	2773	2695	2694
iCa2: OD <sub>ads</sub>	2728	2644	2811	2729	2731
Cb2: OD <sub>surf</sub>	1658	1310	2019	1722	1711
Cb2: OD <sub>ads</sub>	2769	2687	2843	2765	2785
iCb2: OD <sub>surf</sub>	2657	2595	2778	2694	2689
iCb2: OD <sub>ads</sub>	2688	2569	2777	2689	2692

## Intensities and Lattice Vibrations of Further Systems

For the phonons the same 10-layer slab normal modes analyses were checked to get a first impression into how the spectra can look like. But for a better description of the deeper lying phonon vibrations we need to consider more layers of the bulk in order to get more reliable results. From an experimental point of view it is suggested that SFG spectra can give insight into at least three layers of the bulk. Therefore we did calculations for the most stable adsorption geometries for more layered systems, going up to  $6 \times 5 = 30$  layers (with 5 being the number of atomic layers in the unit cell in z direction, compare Figure 2.2), both for the clean surface and for the adsorbate covered surface. These more-layered optimized geometries do not differ strongly from the 10 layer ones that were presented in section 2.2 and hence are not shown *TODO: here, maybe Appendix?*. Respective adsorption energies can be found in Table 2.4. For the low energy modes, one has to have in mind, that normal modes may not be a perfect description of these deeply delocalized vibrations.

The results for the clean surface with intensities from dipole corrections are shown in Figure

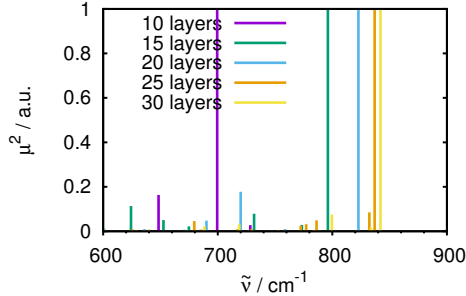


**Figure 2.11.:** Comparison of the spectra for different slab sizes from 10 to 25 layers for the clean surface obtained with normal mode analyses and intensities from dipole corrections.

2.11. For different sized slabs, the results differ largely. Especially the 10 layer system is shifted strongly compared to the other slab sizes. From Table 2.13 can be seen that the most intense peak is shifted to higher wavenumbers with increasing slab size. All spectra shown were normalized to the most intense peak.

**Table 2.13.:** Comparison of the results of the different slab sizes of the NMA: most intense peak from dipole corrections of the lattice vibrations for the clean surface.

Layers	10	15	20	25	30
$\tilde{\nu}$ [cm <sup>-1</sup> ]	700	796	823	837	842

While this trend is true for the clean surface and the lattice region of the covered systems, it does not hold for the OD vibrations regime. As it was already mentioned the OD frequencies seem to be converged for the 10-layer slab and both position and intensity show no eminent difference, see Figures 2.12, 2.13 and 2.14. The exact wavenumbers differ slightly for the OD regions but in general are in good agreement, except for the hydrogen bonded peak in the CUSb||O- $\mu_2$ , confer Figure 2.8. However, the lattice region below 1000 cm<sup>-1</sup> is systematically affected, as in the clean surface system.

The higher coverage systems (see Figures 2.15-2.6) were also examined. The total spectrum and the OD range are shown in Figure 2.15 *TODO: show this alone or only stick to the comparison in Fig. 2.16?* In Figure 2.16 a comparison between the systems with two D<sub>2</sub>O molecules and the corresponding systems with only one adsorbate is given. For all three systems the agreement is very good. If the water molecules interact strongly with each other, the peaks would be shifted heavily. The system inter-CUSe||O- $\mu_2$ +CUSb||O- $\mu_2$  seem to be only weakly affected, inter-CUSe||O- $\mu_2$ +inter-CUSe||O- $\mu_2$  is shifted slightly more. The system CUSb+CUSb||O- $\mu_2$  however, is shifted significantly, displaying a strong interaction between the molecularly

## 2. Water on $\alpha\text{-Al}_2\text{O}_3(11\bar{2}0)$

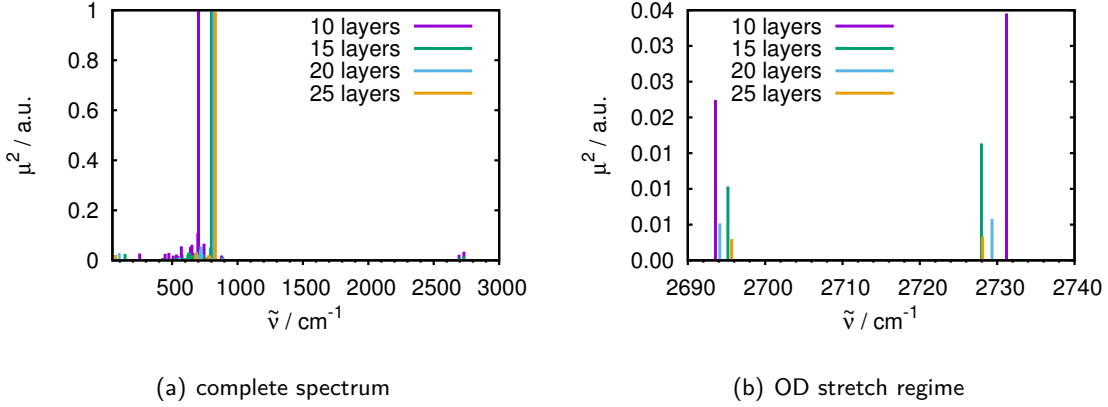


**Figure 2.12.:** Comparison of inter-CUSa||O- $\mu_2$  frequencies for different slab sizes in z direction, obtained by normal mode analyses with intensities from dipole corrections.

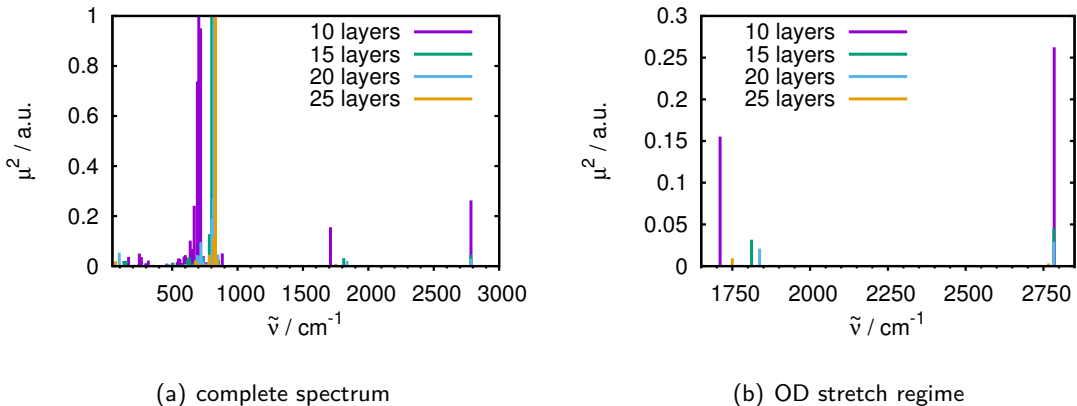


**Figure 2.13.:** Comparison of CUSb||O- $\mu_2$  frequencies for different slab sizes, obtained by normal mode analyses with intensities from dipole corrections.

adsorbed and the dissociated groups. This is interesting since in the adsorption energy the three systems acted differently, the inter-CUSa||O- $\mu_2$ +inter-CUSa||O- $\mu_2$  increased its stability, whereas the system inter-CUSa||O- $\mu_2$ +CUSb||O- $\mu_2$  did not change and CUSb+CUSb||O- $\mu_2$  even was more stabilized. With this in mind, it makes sense that the system, in which the adsorption energy is merely affected also shows hardly any difference to the single adsorption in the spectrum. On the other hand, the system where the molecular water is stabilized by its dissociated neighbor, the spectrum is shifted strongly. The inter-CUSa||O- $\mu_2$ +inter-CUSa||O- $\mu_2$  is more balanced, because the geometry does not change largely and only the adsorption energy is (negatively) affected.

Looking at the spectrum of the system with four adsorbed water molecules (1/3 coverage) we

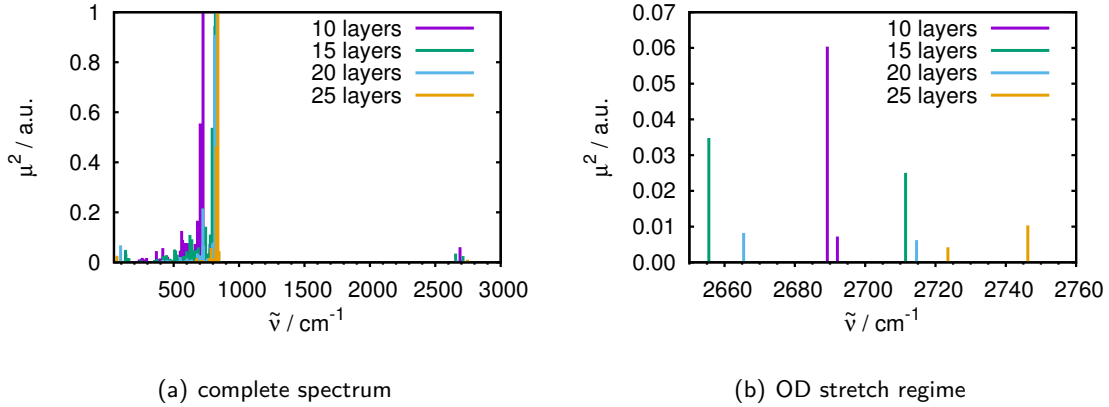


**Figure 2.14.:** Comparison of inter-CUSb||O- $\mu_2$  frequencies for different slab sizes in z direction, obtained by normal mode analyses with intensities from dipole corrections.

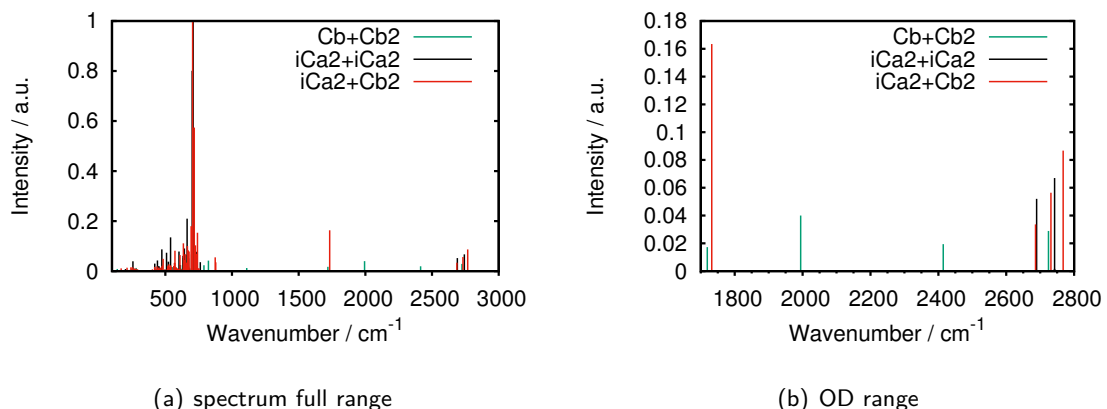


**Figure 2.15.: Spectra from normal mode analyses and dipole intensities for two water molecules per super cell (10 layers). (a) shows the full spectral range and (b) only the OD range above  $1700\text{ cm}^{-1}$ . The short notations stand for Cb=CUSb, Cb2=CUSb||O- $\mu_2$  and iCa2=inter-CUSa||O- $\mu_2$ .**

get Figure 2.17. All of these water molecules are adsorbed in inter-CUSa||O- $\mu_2$ , see Fig. 2.6(a). We see as expected the stretch vibrations of the adsorbed residue at higher wavenumbers. There are three modes for asymmetric and one for symmetric stretch vibrations around  $2740\text{ cm}^{-1}$ . At lower wavenumbers (between  $2691$  and  $2693\text{ cm}^{-1}$ ) there are localized OD<sub>surf</sub> vibrations. Below that there are delocalized combined vibrations of lattice and OD. In comparison to the singly adsorbed system the systems are in astonishing agreement, both in the OD range and the lattice region.

In contrast to the latter systems, for the 1ML system it is not easy to compare to the singly

## 2. Water on $\alpha\text{-Al}_2\text{O}_3(11\bar{2}0)$

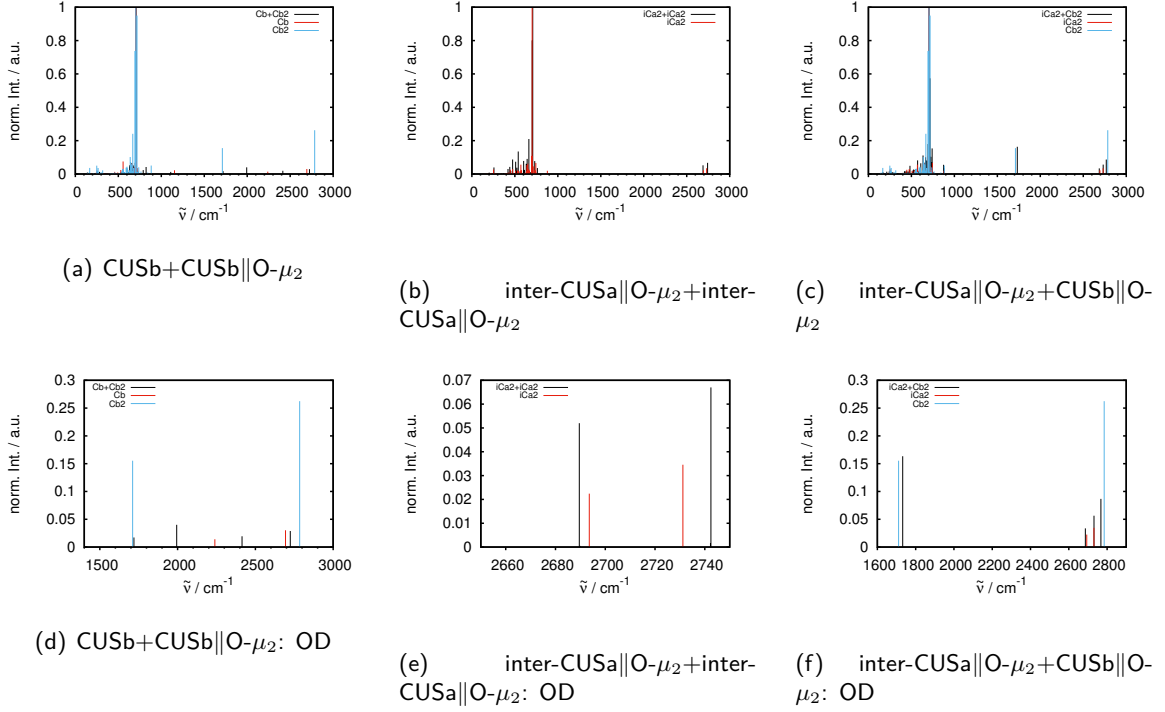


**Figure 2.16.:** Comparison between  $2\text{D}_2\text{O}$  system with the corresponding systems with one water molecule, upper line (a,b,c) complete spectrum, lower line (d,e,f) OD range.

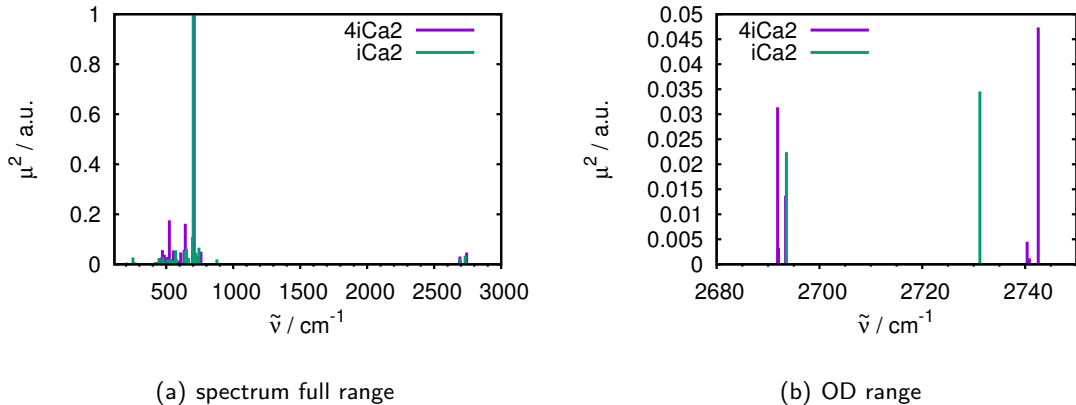


**Figure 2.17.:** Spectra from normal mode analyses and dipole intensities for four water molecules per super cell (10 layers). (a) shows the full spectral range and (b) only the OD range above  $2680\text{ cm}^{-1}$ . The short notations stand for iCa2=inter-CUSA||O- $\mu_2$ .

adsorbed species, since it consists of a wild mixture of 12 adsorbed OD residues (on CUSb, inter-CUSA and inter-CUSb), as well as 12 surface OD groups on O- $\mu_2$  and also the less fa-

## 2.4. Vibrational Frequencies

vorable threefold coordinated O- $\mu_3$ . Due to this magnitude of different species, the spectrum possess many peaks in the OD region, see Figure 2.18. Hydrogen bonding and interaction between groups shift many of the peaks. From  $\approx 2000$  to  $2740\text{ cm}^{-1}$  various OD stretch vibrations occur. In the region between  $872$  and  $1117\text{ cm}^{-1}$  there are bending like vibrations of mostly O- $\mu_2$ D groups, and below that delocalized OD and lattice vibrations can be found. As before, the agreement in the OD range (without hydrogen bonding) is very good (Figure

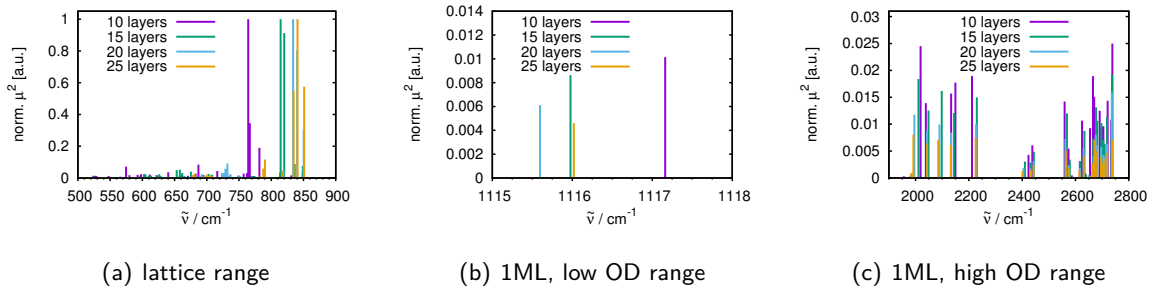


**Figure 2.18.:** Comparison of the spectra of the fully with D<sub>2</sub>O covered surface. Shown is a comparison between the different slab sizes for (a) the lattice region, (b) the low energy OD range with butterfly like vibrations and (c) the high energy OD range *TODO: it looks like there are 3 distinguishable region? can this be explained?*

2.18(c)), in the hydrogen bonded region around  $1116\text{ cm}^{-1}$  is convincing (Figure 2.18(b)) and only in the lattice region (Figure 2.18(a)) is slightly different with the highest energy peak shifted to higher energy with increasing slab size, which is the same trend as for the clean surface.

In addition to the different sized slabs, a symmetric model of the surface with 15 layers was built. On both the top and the bottom, D<sub>2</sub>O adsorbed dissociatively in inter-CUSA||O- $\mu_2$ . A figure of the structure can be found in Figure 2.19. In this model all atoms were allowed to relax. Henceforth the normal mode analysis gives three imaginary frequencies, that represent frustrated translation in a, b and c direction. The spectrum was calculated at the basis of dipole corrected normal modes and can be seen in Figure 2.20. The high energy part (see Figure 2.20(b)) shows that each of the two peaks comes as a doublet due to the imperfect degeneracy of “both sides” of the slab, which has numerical reasons. These doublet lie at  $2690$  and  $2725\text{ cm}^{-1}$ , which is slightly lower than the asymmetric model (only one adsorbate on the top) results for all applied slab sizes. For example, for the 15 layer system the peaks come up at  $2695$  and  $2728\text{ cm}^{-1}$ . In the lattice region, these shifts are stronger, but nevertheless small in general. The most intense peak is shifted from  $801$  to  $816$  (15 layer symmetric slab) but

## 2. Water on $\alpha\text{-Al}_2\text{O}_3(11\bar{2}0)$

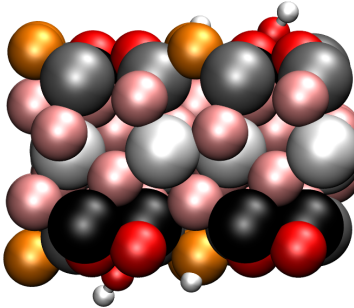


**Figure 2.19.:** PBE+D2 optimized geometry of the 15-layer symmetric slab. The adsorbed species is the most stable inter-CUSa||O- $\mu_2$ . Color code as explained above.

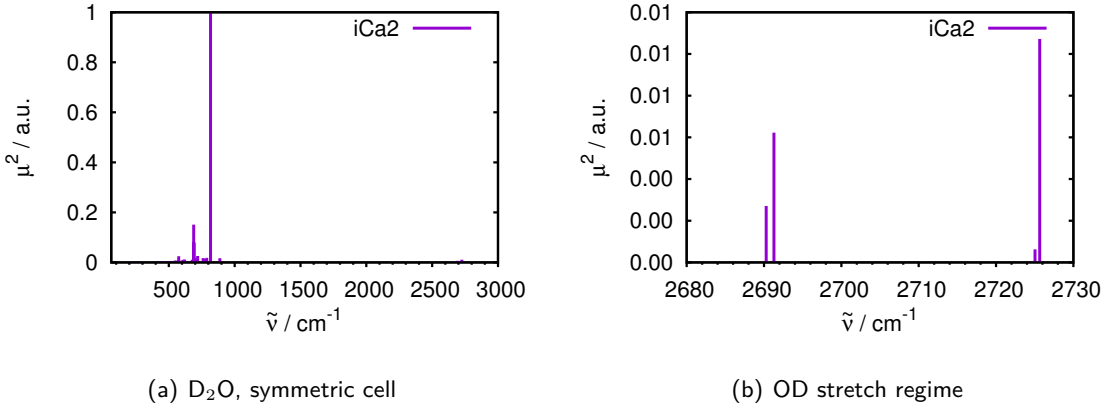


**Figure 2.20.:** Stick spectrum of the 15 layer symmetric adsorption model. (a) shows the total range of the dipole corrected spectrum and (b) gives a closer look at the OD range, featuring two doublets.

this shift is rather small. The overall agreement is very good so that it can be concluded, that although the computational costs are increased the symmetrically adsorption ansatz does not give any new insights to the system.

Apart from the most stable surface termination (called O-I in [35]), calculations of the second most stable surface termination (O-II) were done. Frequencies were analyzed of the clean surface and the fully covered system. This was done for the 10 and 25 layer systems. **TODO: continue here when the calculations are ready! Compare O-I and O-II for 10 and 25 layer slabs, both for clean surface and fully covered.**

## 2.4. Vibrational Frequencies

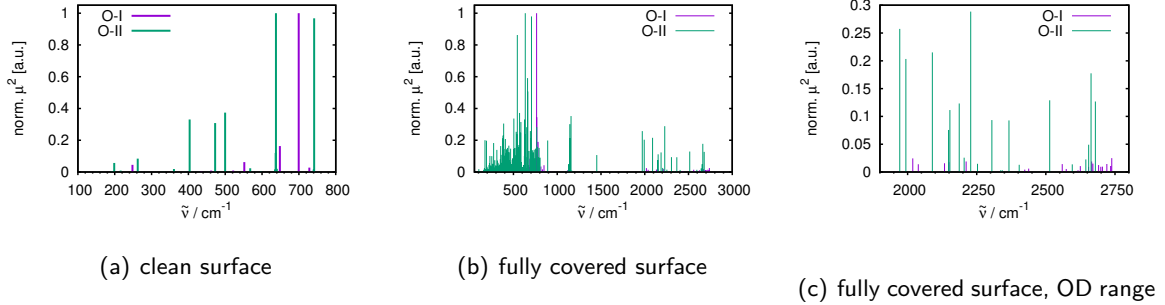


**Figure 2.21.:** Comparison of the 10-layer slab spectra calculated with normal mode analysis and intensities from the dipole corrections. The clean surface (a), O-I termination (most stable under the whole range of chemical potential) and O-II termination (see Kurita [35], also relatively stable over a wide chemical potential range). The comparison of the fully covered O-I and O-II terminations is shown in (b) with a detailed view of the OD range in (c).

### 2.4.2. Born Effective Charges

These results were obtained for the three most stable adsorbed systems with 10 layers. For getting the spectrum an angle of the IR beam of 45° was assumed. Because both the dipole corrections intensities and the BEC calculations are based on normal modes, the frequencies are equal and only the intensities differ. In Figure 2.22 the spectra for the three most stable structures can be seen, (a) depicts the whole range and (b) the OD range only. The peak

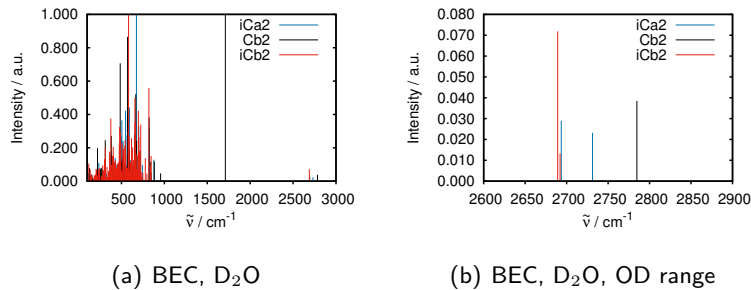


**Figure 2.22.:** IR spectrum with intensities based on Born effective charges (BEC) evaluation for the three most stable species, (a) full spectrum, (b) OD range above 2600 cm<sup>-1</sup>.

around 1700 cm<sup>-1</sup> comes solely from the hydrogen bonded CUSb||O- $\mu_2$  OD group. The other non hydrogen bonded peaks come above 2500 cm<sup>-1</sup> and the lattice region can be seen below 1000 cm<sup>-1</sup>.

In comparison to the results from the dipole corrections, for inter-CUSA||O- $\mu_2$  the intensities in the OD range are nearly the same, although the more intense peak is changed. In the lattice

## 2. Water on $\alpha\text{-Al}_2\text{O}_3(11\bar{2}0)$

region the agreement is not as excellent. For the OD region of CUSb||O- $\mu_2$ , the agreement is worse, BEC predicts the H-bonded peak at  $1711\text{ cm}^{-1}$  to be the most intense whereas the dipole corrected intensities give this in the lattice region which is also very distinctive. Concerning the inter-CUSb||O- $\mu_2$  the OD region shows good agreement, also the more intense peak is the same. Again in the lattice region, the difference is larger. This might be due to the fact, that low energy modes are less precisely represented by normal modes and both methods give low quality results.

### 2.4.3. Velocity-Velocity Autocorrelation Function

The velocity-velocity autocorrelation function that is evaluated from *ab initio* MD calculations and Fourier transformed is a totally different ansatz to calculating a spectrum. No frequency analysis has to be done, *i. e.* no harmonic approximation is applied. Instead the movement of the nuclei at the temperature is taken into account. At 300 K for the clean surface (30 layers) and the three most stable adsorbed structures (inter-CUSA||O- $\mu_2$ , CUSb||O- $\mu_2$  and inter-CUSb||O- $\mu_2$ , 10 layers each) the respective MD were calculated, starting from the minimum structure.

For the clean surface, the 30-layer model was applied, with a duration of 5 ps. As for the

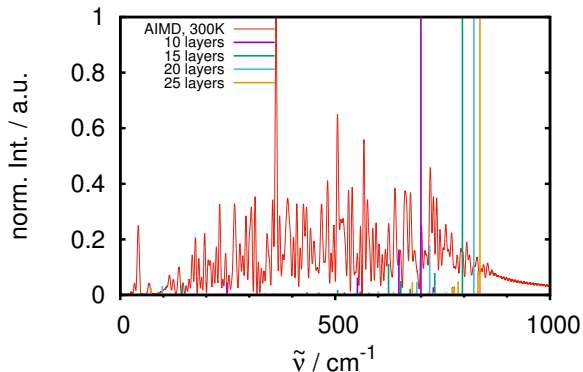


**Figure 2.23.:** Power spectrum of the clean surface of the 30-layer slab, calculated from velocity-velocity autocorrelation functions from canonical (NVT) AIMD trajectories at 300 K (5000 steps, 5 ps). In comparison to the power spectrum, the stick spectra of the dipole corrected normal modes are shown.

normal modes results, the peaks are below  $900\text{ cm}^{-1}$ , see Figure 2.23. The shown intensities can not be perfectly reasonable compared to the IR intensities obtained from BEC or dipole corrected normal modes, but still as a first impression it is a useful approximation. The most intense peak in the power spectrum can be observed at significantly lower energy than for any

## 2.4. Vibrational Frequencies

normal mode based result. Also more peaks are present in the whole range from 0 to around  $900\text{ cm}^{-1}$ .

The results for the adsorbed species were obtained by AIMD calculations of the 10 layer system at a temperature of 300 K. The system inter-CUSa||O- $\mu_2$  was propagated for 3.68 ps. The respective spectrum is shown in Figure 2.24(a) and shows one intense peak in the OD region at  $2720\text{ cm}^{-1}$ . Compared to the normal modes where we observe two peaks, one for the surface and one for the adsorbed OD group. It is possible that both groups overlap and lead to the broad peak. In the lattice region, as it could be observed for the clean surface as well, the intense peaks are at lower wavenumbers and there is no strong agreement.

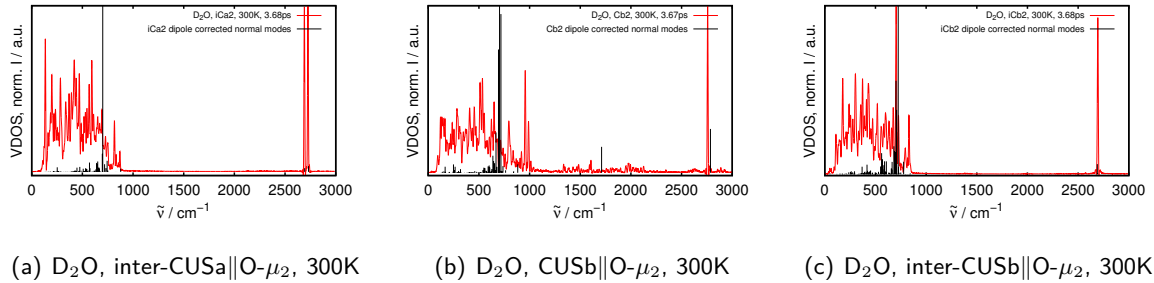


**Figure 2.24.:** Power spectra are shown in red, obtained from NVT AIMD trajectories at 300K for the geometries (starting points were geometry optimized structures at 0K) of the most stable structures via vel-vel ACF. Duration of the trajectories is given inside the figures and is approximately 3.7 ps. In black the spectrum with intensities from dipole corrected normal modes are shown for comparison.

The spectrum of the CUSb||O- $\mu_2$  system can be seen in Figure 2.24(b). It was propagated for 3.67 ps. The OD range shows one clear peak at around  $2757\text{ cm}^{-1}$ , that can be compared to the non-hydrogen bonded peak in the normal modes. In contrast to that the hydrogen bonded peak that can be found in the normal modes at  $1711\text{ cm}^{-1}$  is given in the power spectrum as a multitude of small peaks in the region between  $1300$  and  $2100\text{ cm}^{-1}$ . The lattice region the intense peaks are distributed wider and also the most intense peak of the lattice region is at a higher energy than the normal modes suggest.

For the inter-CUSb||O- $\mu_2$  species with a trajectory duration of about 3.68 ps, the OD region is in very good agreement with the normal mode results (see Figure 2.24(c)). There is one broad peak that covers both peaks from the normal modes. Also in the lattice region there is good compliance, the most intense peaks are only separated by  $20\text{ cm}^{-1}$  which is the best result for the computed systems.

*TODO: It also is possible to separate modes from water layers from bulk phonons, like Giacomo*

## 2. Water on $\alpha\text{-Al}_2\text{O}_3(11\bar{2}0)$

*does. Though, this is not really important if you don't use hydroxylated surface with a higher water coverage. So for Giacomo's system it makes sense, but here it is unnecessary.*

### 3. Water on $\alpha\text{-Al}_2\text{O}_3(0001)$

The (0001) surface is the most stable surface site of alumina under UHV conditions, and was subject of several studies so far **TODO: cite some**. Both experimental and theoretical studies discovered characteristics and specialties of this crystal cut. In our workgroup previous work was done concerning the stability of low limit water coverage and their vibrational spectroscopic behaviour, reaction pathways between these stable minima, but also studying higher water coverages and hydroxylated surface systems [28–30].

In this work, the focus lies more on two topics:

- (i) Understanding the processes of a water molecule ( $\text{D}_2\text{O}$ ) being shot at the surface with a molecular beam source with the help of *ab initio* Molecular Dynamics and
- (ii) The improvement of reaction rates with different methods beyond GGA functionals (as PBE).

First, the surface and the most stable adsorption patterns are introduced (section 3.1), followed by the results for the molecular beam scattering (section 3.2) and the improvements for the reaction rates (see section 3.3).

#### 3.1. Surface Model and Static Calculations

The most stable surface cut is a stoichiometric, Al terminated one, and in contrast to the  $(11\bar{2}0)$  surface there is only one type of Al-CUS atom, which is a reactive Lewis-acid site. Also, all oxygen atoms are threefold coordinated, that leads to a topography that is not as complex as for the higher indexed surfaces. We apply here a  $2 \times 2$  supercell with vectors that were optimized from the bulk structure vectors (previous work of J. Wirth [28]). The surface slab consists of nine atomic layers, that equals three repeating units in z direction of the type Al-O<sub>3</sub>-Al..., with the top five layers being allowed to relax during optimization and AIMD and the lowest four layers being fixed to bulk values, see Figure 3.1. The unit cell vectors in there are equal to  $a = b = 9.66 \text{ \AA}$  and a  $60^\circ$  angle between them. The  $c$ -vector of the slab model is  $31.4 \text{ \AA}$  long, hence the vacuum gap between two slabs in this direction is  $26.4 \text{ \AA}$ . The stability, vibrations and reactivity of one water molecule per  $2 \times 2$  supercell were already studied by Dr. Jonas Wirth. As it was published in [28], there is one molecular minimum on top of a CUS atom and

### 3. Water on $\alpha\text{-Al}_2\text{O}_3(0001)$

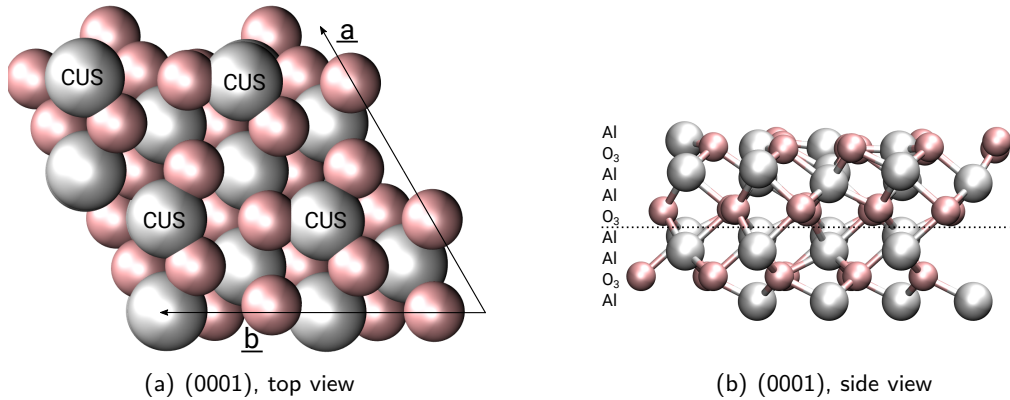


**Figure 3.1.:** Surface model of the (0001), the most stable surface cut under UHV conditions. The top view (a) shows 4 Al CUS atoms, that are surrounded by three threefold coordinated surface oxygen atoms. (b) reveals the Al terminated surface cut in detail with the atomic layers.

three dissociated states (see Figure 3.2): the next neighboring 1-2 dissociated state, the 1-4 dissociated structure with the hydrogen atom being one position further and the 1-4' that is the configuration with the greatest distance that is possible for this slab size. From these, the 1-2 dissociated species is the most stable one and the 1-4' is the least stable one, see left side of Table 3.1. For the stability of the molecular and the 1-4 dissociated species, the situation is more controversial in the literature. In our periodic DFT studies with VASP, it lies between the previously mentioned ones, depending on the exact method employed, for PBE+D2 the molecular adsorbed species is more stable than 1-4, for PW91+D2 the 1-4 dissociated is more stable, whereas PW91 without dispersion corrections gives the same adsorption energy for both species (the values for the adsorption energy are calculated analogously to the (11 $\bar{2}$ 0) surface cut, see eq. 2.1). Calculations with an atom centered basis instead of plane waves with the crystal code show, that for most basis sets the molecular species is more stable and for others, they are both equal in adsorption energy. *TODO: see section 3.3.1, add it there!*

Of course, there are reactions linking these minima, dissociation, OH- and H-diffusion were studied, as well as rotation of an OH group and molecular water diffusion from CUS to CUS. The latter two do not play a crucial role in this work, especially the CUS to CUS diffusion of molecular water is very improbable due to the slow reaction rate. Adsorption energies and reaction rates that are of importance for this work are shown in Table 3.1, these PBE results were unpublished and obtained by J. Wirth.

The adsorption process from the surface itself was studied, by starting from the molecular minimum, gradually doing optimizations with greater O-surface distance and letting everything relax except for the c coordinate of the water-oxygen atom. This calculations gives an energy

### 3.1. Surface Model and Static Calculations

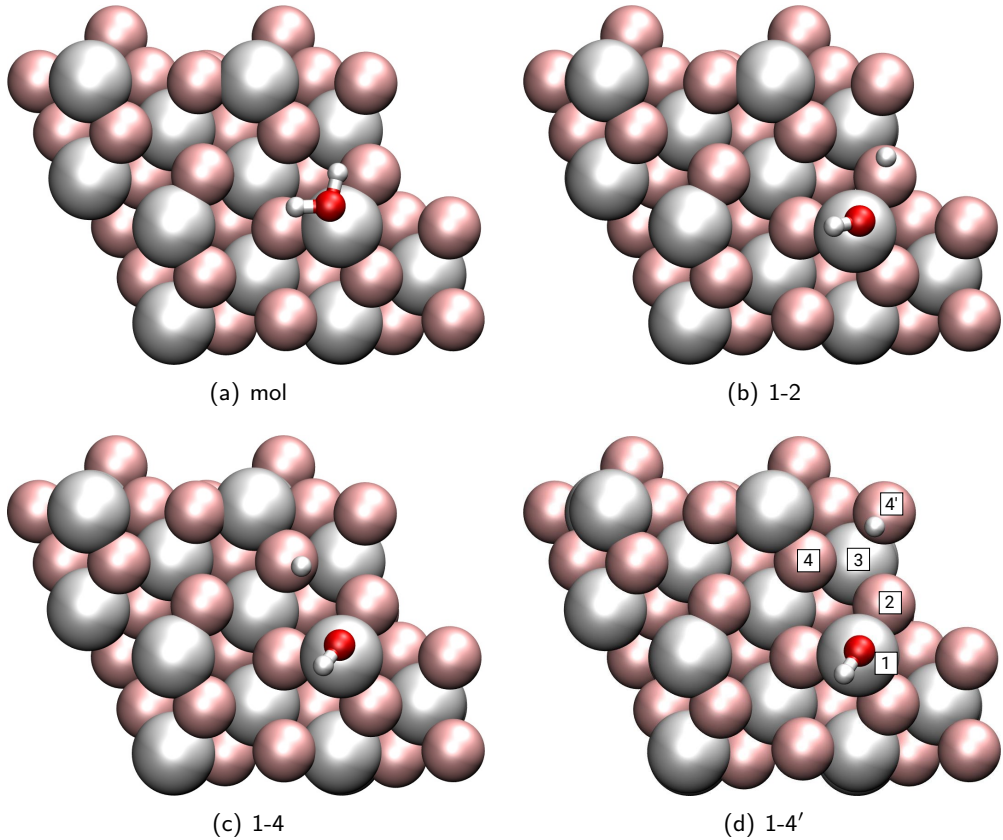


**Figure 3.2.: Adsorption geometries of the molecular and the three dissociated species. Adsorption energies for these species can be found in Table 3.1. Additionally, panel (d) shows the numbering of the surface atoms that gives the nomenclature.**

**Table 3.1.: Adsorption energies for the stable minima (left part) and reaction rate constants  $k$  in  $\text{s}^{-1}$  at 300 K with corresponding barrier heights  $\Delta E^\ddagger/\Delta G_{300\text{K}}^\ddagger$  in eV for the processes connecting these minima (right part). Here the upper two line show the reactions in the direction given in the name and the lower two line give the back reaction's rates constants and barriers. All values were calculated with PBE including D2 dispersion corrections and are unpublished work of Dr. J. Wirth.**

E <sub>ads</sub> [eV]				k <sub>300K</sub> [s <sup>-1</sup> ]				
mol	1-2	1-4	1-4'	diss-1-2	diss-1-4	diff-2-4	diff-2-4'	diff-4-4'
-1.31	-1.69	-1.30	-1.21	8.0×10 <sup>10</sup>	2.8×10 <sup>10</sup>	2.7×10 <sup>1</sup>	3.8×10 <sup>1</sup>	7.1×10 <sup>5</sup>
				0.13/0.11	0.19/0.14	0.82/0.68	0.81/0.67	0.61/0.41

### 3. Water on $\alpha\text{-Al}_2\text{O}_3(0001)$

profile for the adsorption/desorption but no barrier could be found (see Figure 3.3), so the underlying adsorption process is thought to be barrierless.

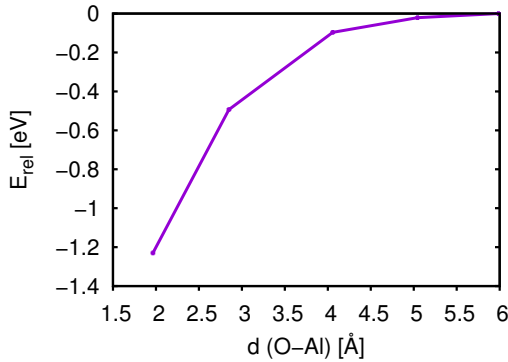


**Figure 3.3.:** Energy profile of the adsorption process, relative to the energy of the system with a distance of 5.98 Å.  $d(\text{O-Al})$  denotes the distance between the oxygen atom of the water and the Al-CUS where the water is/was adsorbed molecularly.

## 3.2. AIMD for MBS Process

**TODO:** *Hass et. al.*

*put the data in the appendix?*

Molecular beam experiments have shown recently that water is able to adsorb both molecularly and dissociatively on an  $\alpha\text{-Al}_2\text{O}_3(0001)$  surface. The results show an enhanced dissociation probability compared to “pinhole dosing”, which may be referred to as adsorption under thermal equilibrium conditions. However, precise mechanistics of the ongoing reactions and their relative probabilities are not known. In this work *Ab Initio* Molecular Dynamics calculations were conducted to unravel this process. In these simulations heavy water ( $\text{D}_2\text{O}$ ) collides with the  $\alpha\text{-Al}_2\text{O}_3(0001)$  surface. This was done for better comparison to the results of R. Kramer Campen, Interfacial Molecular Spectroscopy group, FHI Berlin.

Previous studies by Hass *et. al.* [38, 39] discussed the idea whether water will first adsorb molecularly and dissociate in a consecutive step or if it can dissociate directly. This study did not consider water being shot on the surface rather than an adsorbed water that was propagated.

To tackle this question, we did AIMD calculations for a water molecule approaching the surface. Different beam and surface models were applied.

**TODO:** *more or will this be covered in the sections to come?*

### 3.2.1. Beam Model

For the understanding of a Molecular Beam source experiment, the introduction of a beam is an essential part of the model. However, it was not possible to compute a fully realistic beam that was statistically converged, which would require wide knowledge about energy and velocity distributions and a systematic high dimensional sampling, that is not feasible with the computational power available at the moment. Instead as a first order approach, a single, rigid water ( $D_2O$ ) molecule (initial parameters are  $d_{OD} = 0.97\text{\AA}$  and bond angle of  $104.5^\circ$ ) was sent perpendicularly from a center of mass position from a distance of  $4\text{\AA}$  onto the surface, in agreement with the experiment. Having these degrees of freedom excluded, six are still left (see Figures 3.4, 3.5 and Table 3.2): two for the impact site  $[a_0, b_0]$  as it is given relative to the super cell vectors  $\underline{a}$  and  $\underline{b}$ , three Euler angles  $\alpha$ ,  $\beta$  and  $\gamma$  for the rotational orientation of the molecule with respect to the surface and the kinetic energy  $E_{kin}$  that gives the molecule a momentum towards the surface, solely as translational motion, no vibration or rotation included. These parameters are varied systematically to gain insight into the process.

As was mentioned before, the barriers can be high (and corresponding rates low), especially for the H-diffusion reactions, but the adsorption process itself is barrierless, and additionally the incoming water molecule has kinetic energy so that processes, that are slow at room temperature otherwise, can be speeded up.

Further details on the improvements of this simplest model are made in subsection 3.2.6, that address clustering and rotational and vibrational excited water, respectively.

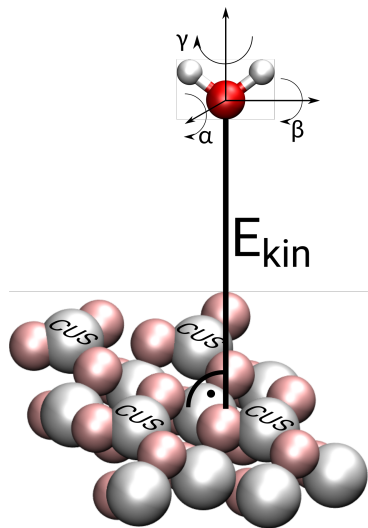


**Figure 3.4.:** Sketch for initial parameters of the trajectories. The water molecule is situated  $4\text{\AA}$  above the surface and is arranged within the shown coordinate system, before being shot onto the surface with a defined kinetic energy  $E_{kin}$ .

### 3. Water on $\alpha\text{-Al}_2\text{O}_3(0001)$

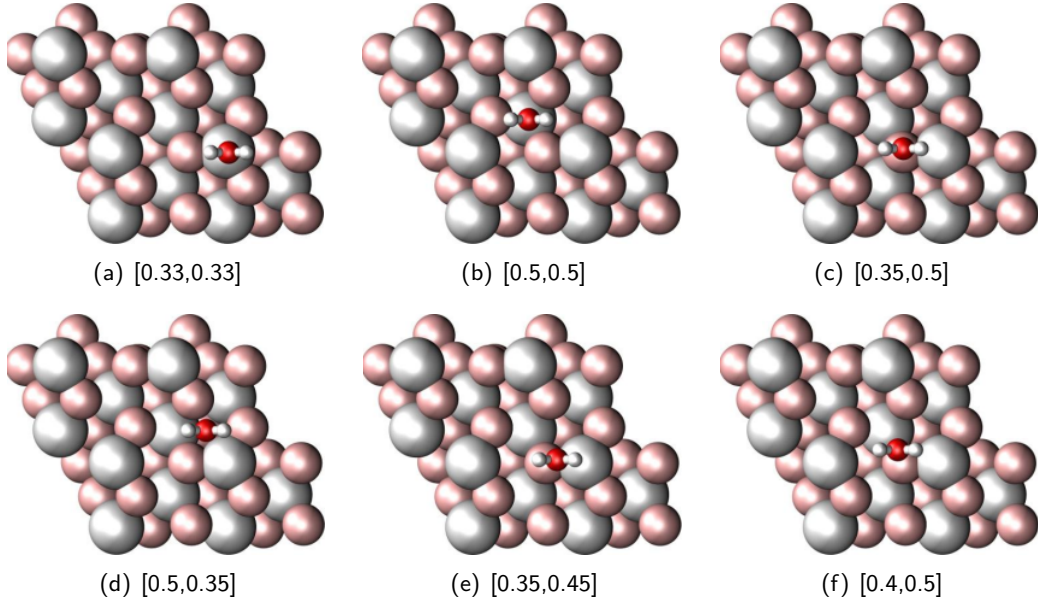


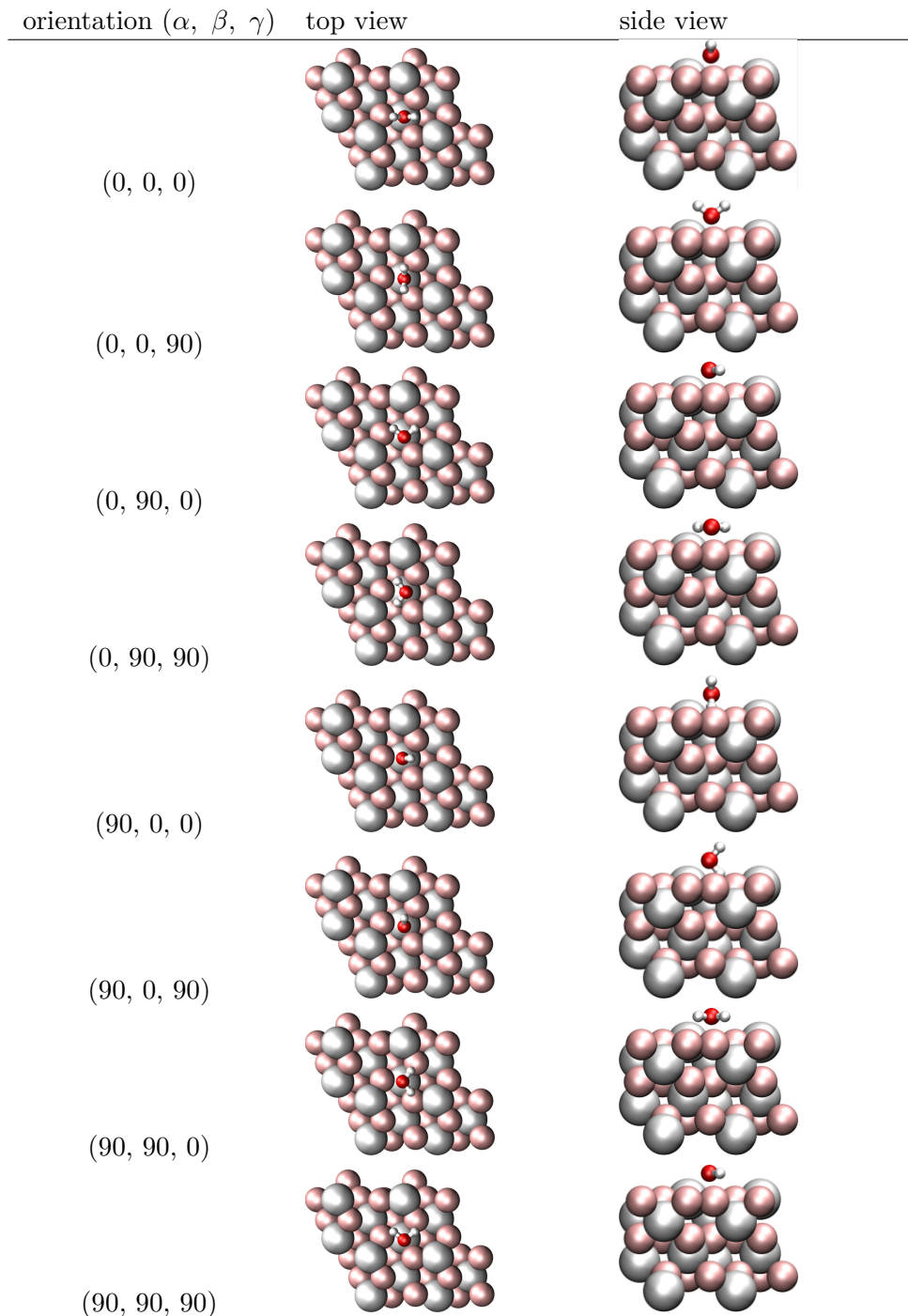
**Figure 3.5.:** The six impact points  $[a_0, b_0]$  that were used in the AIMD calculations (shown for the rotational orientation  $[0, 0, 0]$ , topview). The different points reflect the most important sites of the surface,  $[0.33, 0.33]$  is on top of an Al CUS,  $[0.5, 0.5]$  on top of an Al in a lower layer.  $[0.35, 0.5]$  is on top of a surface oxygen atom, whereas  $[0.5, 0.35]$  is on top of a subsurface oxygen atom.  $[0.35, 0.45]$  is in a gap between an Al CUS and a surface oxygen and  $[0.4, 0.5]$  is in the gap between a surface O and a subsurface Al atom.

#### 3.2.2. Example Trajectories

Before going to the details, example trajectories for each process leading to one of the four most stable adsorbed species, molecular adsorption, 1-2 dissociation, 1-4 dissociation and 1-4' dissociation are shown in Figure 3.6. The applied parameters are reported in the respective caption. These figures were all obtained from canonical calculations (NVT) at 300K (see Figure 3.6, the trajectory shown in (d) was additionally preexcited in the asymmetric stretch mode leading to 1-4' dissociation). As one can see, molecular, 1-2 and 1-4 dissociated species can occur directly at the impact time of the water molecule at the surface and is henceforth called direct dissociation from the gas phase. For the 1-4' dissociation shown in Figure 3.6(d), this process does not happen directly at the impact but (in this case) ca. 40 fs later, so this is referred to as indirect dissociation with a molecular intermediate. This indirect process is not unique for the 1-4' dissociated species, all the other species including the molecular can be observed to happen indirectly by either being reflected first from the surface before adsorbing/dissociating or by adsorbing molecularly before dissociating. However, the 1-4'

### 3.2. AIMD for MBS Process

**Table 3.2.:** Orientations of the water molecule, given in  $^{\circ}$ . Shown are both top view and side view at impact point 0.5,0.5. (look from the right-hand side to the top view)



### 3. Water on $\alpha\text{-Al}_2\text{O}_3(0001)$

species was the only one that could not be observed after direct dissociation.

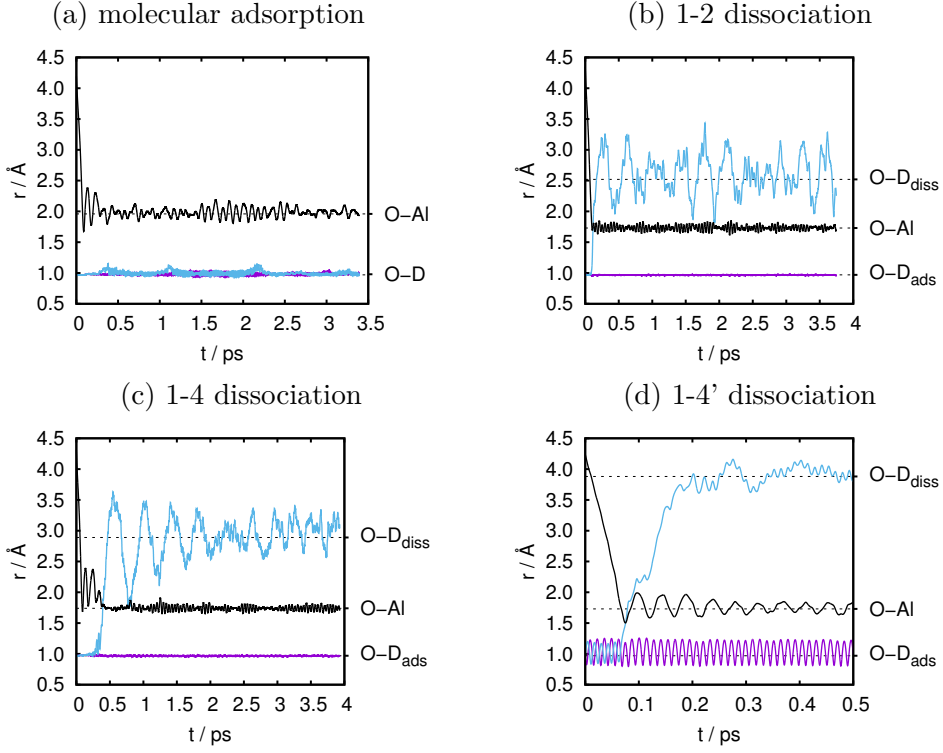


**Figure 3.6.:** The four adsorbed states of water, as shown in Figures 3.2(a)-(d) can be obtained in these exemplary trajectories. All of them are from canonical (NVT) trajectories at  $T = 300$  K. The initial parameters: (a)  $E_{\text{kin}} = 0.7$  eV,  $[a_0, b_0] = [0.33, 0.33]$ ,  $[\alpha, \beta, \gamma] = [0, 0, 90]$ ; (b)  $E_{\text{kin}} = 0.7$  eV,  $[a_0, b_0] = [0.35, 0.45]$ ,  $[\alpha, \beta, \gamma] = [0, 0, 0]$ ; (c)  $E_{\text{kin}} = 0.7$  eV,  $[a_0, b_0] = [0.33, 0.33]$ ,  $[\alpha, \beta, \gamma] = [0, 90, 0]$ ; (d)  $E_{\text{kin}} = 0.7$  eV,  $[a_0, b_0] = [0.35, 0.5]$ ,  $[\alpha, \beta, \gamma] = [0, 0, 0]$ . As specified in Subsection 3.2.6, for the latter the water molecule was vibrationally preexcited along the asymmetric stretch normal coordinate. The  $r$  values (y axis) corresponds to the bond lengths between water-O and the CUS Al atom on which D<sub>2</sub>O or the water hydroxyl unit OD adsorb (O-Al), the distance between water-O and D in non-dissociated (fragments of) D<sub>2</sub>O (O-D or O-D<sub>ads</sub>), and the distance between water-O and D in dissociated (fragments) of D<sub>2</sub>O (O-D<sub>diss</sub>), respectively. Also the interatomic distances of the minimum geometries are given as horizontal dashed lines. Panel (d) shows that the 1-4' state is not obtained directly but reached via a short-lived 1-2 dissociation intermediate.

Probabilities for all outcomes can be found in the Appendix.  
TODO: find a better place for this sentence!

### 3.2. AIMD for MBS Process

#### 3.2.3. Microcanonical AIMD at clean surface

The effects of a single D<sub>2</sub>O shot to the cool surface with a NVT ensemble (microcanonical AIMD, the 0 K optimized geometry of the surface had no initial momenta) were studied systematically by probing over three parameters: Five different kinetic energies (from 0.5 to 0.9 eV in 0.1 eV steps), six lateral impact points at the surface ([0.33,0.33], [0.5,0.5], [0.35,0.5], [0.5,0.35], [0.35,0.45], [0.4,0.5], see also Figure 3.5) and eight different orientations of the water with respect to the surface ([0,0,0], [0,0,90], [0,90,0], [0,90,90], [90,0,0], [90,0,90], [90,90,0], [90,90,90], see also Tab.3.2). These  $5 \times 6 \times 8 = 240$  AIMD trajectories for the clean surface at  $T = 0$  K were carried out for ca. 1.2 ps each.

In the trajectories either molecular adsorption, 1-2 dissociation or reflection could be observed. Dissociation was assumed, if the OD distance was greater than 1.3 Å, but it was made sure that the results did not differ for a greater cutoff distance. Interestingly, only 1-2 dissociation and no 1-4 dissociation could be observed for the conditions (NVT, clean surface), although the molecular and the 1-4 dissociated species are almost equal in energy, and also the barrier heights for the dissociation to 1-2 (0.13 eV) and 1-4 (0.19 eV) do not differ largely. As it is shown later, other conditions are necessary for reaching 1-4 dissociation.

For a statistical analysis of the data see Figure 3.7, where the probabilities for reflection,

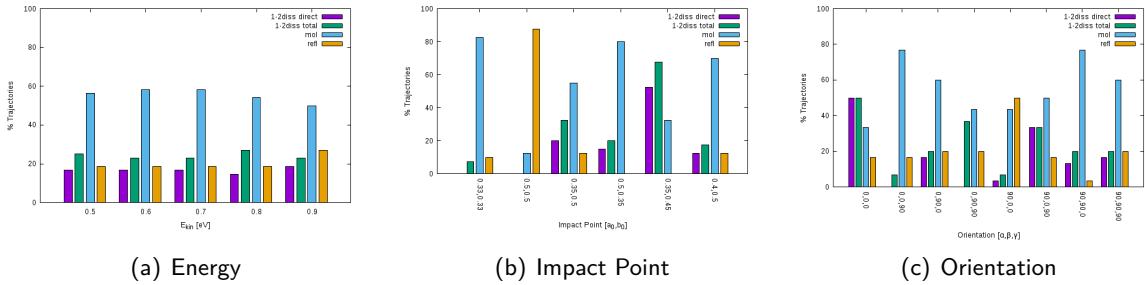


**Figure 3.7.:** Bar charts showing the statistics of NVE AIMD trajectories at 0 K for a single D<sub>2</sub>O molecule approaching the clean alumina(0001) surface. (a) summarizes the findings for all kinetic energies  $E_{\text{kin}}$  averaged over  $6 \times 8 = 48$  combinations of impact point and orientation. In (b), for all impact points  $[a_0, b_0]$  is averaged over  $5 \times 8 = 40$  combinations of kinetic energies and rotational orientation and (c) gives an overview over all orientational orientations  $[\alpha, \beta, \gamma]$ , averaged over  $5 \times 6 = 30$  combinations of kinetic energies and impact points. The columns give percentages of the different outcomes - here labeled as “refl” reflection, “mol” molecular adsorption and direct and total 1-2 dissociation (“1-2 diss direct” and “1-2 diss total”). If one type of outcome did not occur, no column is shown.

molecular adsorption and 1-2 dissociation are shown as a function of the kinetic energy (a), impact point (b) and the orientation (c). It was distinguished between direct and indirect

### 3. Water on $\alpha\text{-Al}_2\text{O}_3(0001)$

dissociation. Admittedly, this analysis is restricted by the number of trajectories (240). From these figures and the data one can derive the following conclusions:

As anticipated, all three processes could be observed, reflection (20.4%, 49 of the 240 trajectories), molecular adsorption (55.4%, 133 trajectories) and 1-2 dissociation (24.2%, 58 trajectories).

Looking at the influence of the kinetic energy in Figure 3.7(a), the results do not depend largely on the initial kinetic energy of the molecule, at least for the probed energy range. In all cases molecular adsorption dominates, followed by 1-2 dissociation and reflection, that are in the same range around 20-25%. This reflecction probability  $P_{\text{diss}}$  is only increased for 0.9 eV, at the expense of the molecular species. To tackle the low energy regime, one additional trajectory of 0.1 eV was done ( $[a_0, b_0] = [0.35, 0.45]$ ;  $[\alpha, \beta, \gamma] = [0, 0, 0]$ ), for which  $P_{\text{diss}} = 1$  for all energies  $\geq 0.5$  eV. In the case of  $E_{\text{kin}} = 0.1$  eV, the trajectory only shows molecular adsorption. This result was rather surprising, since the kinetic energy plus the adsorption energy minus the barrier height is with  $(0.1 + 1.31 - 0.13)\text{eV} = 0.28$  eV larger than the reaction barrier. It seems that the excess energy is not available for the OD-bond breaking and instead relaxes in other degrees of freedom of the system. That allows to draw the conclusion, that a minimum kinetic energy is necessary for the dissociation process. In the experiments of R. K. Campen, a kinetic energy of the beam between 0.6 and 0.75 eV is used. This minimum energy constraint can be one possible explanation of the difference between MBS and pinhole dosing. In the latter case, the only energy of a water molecule comes from the thermal energy that is for a D<sub>2</sub>O molecule in the gas phase at 300 K around  $\frac{3}{2}k_B T \approx 40$  meV.

In contrast to the kinetic energy, the lateral impact point at the surface has a great influence on adsorption and dissociation probabilities as can be seen in Figure 3.7(b). For the impact point [0.5,0.5], that is at a non-surface Al position, 88% of the trajectories get reflected and molecular adsorption and 1-2 dissociation are oppressed, whereas for [0.33,0.33], directly on top of an Al CUS position, 83% adsorb molecularly which dominates clearly over 1-2 dissociation. In contrast to both sites, [0.35,0.45] which lies at a gap between the CUS position and a neighboring oxygen atom leads to a high dissociation probability of  $P_{\text{diss}} \approx 68\%$  with a minor percentage of indirect dissociation. This high dissociation probability can be explained by the fact, that the molecule hits the surface already in a “product-like” geometry, so that the OD bond breakage is facilitated.

The initial rotational orientation has also an effect (cf. Figure 3.7(c)), although not so clearly as for the impact point. This might be explained when looking at the trajectories in detail, so one can see, that the water molecule rotates due to the attractive and repulsive interaction with the surface atoms. That leads to a reorientation of the water molecule right before adsorbing, so that the initial orientation is not remembered by the system. The orientation

### 3.2. AIMD for MBS Process

that the molecule is in shortly before reaching the surface is more important, also here, if the molecule's orientation is already in a product-like state, the dissociation probability is elevated. As can be seen from the data, direct dissociation dominates mostly over indirect dissociation, although it is dependend from the initial conditions, e.g. for the initial orientation [0,90,90] only indirect dissociation is observed.

#### 3.2.4. Thermalized Surface

After getting an impression about the system with the microcanonical MD with the clean surface, as a next step the thermalized surface at 300 K is studied. For this the naked surface was preequilibrated at 300 K for 1 ps and the obtained geometry with the included velocities was used as an input to the following calculations. Here, only a kinetic energy of 0.7 eV was considered, since this energy is the closest to previous experiments by Campen and also the energy dependence was shown to be very low. The water molecule was then shot onto the equilibrated surface and the heat bath acted from the start on the water molecule. This is not huge a problem, since the molecule hits the surface quickly and thus hardly affects the dynamics.

First, for a selection of 5 parameter sets 100 NVT trajectories were calculated each at a temperature of 300 K. These parameter sets are  $[a_0, b_0][\alpha, \beta, \gamma] = [0.35, 0.45], [0, 0, 0]; [0.35, 0.45], [0, 90, 90]; [0.35, 0, 45], [90, 90, 90]; [0.4, 0.5], [0, 0, 0]; [0.5, 0.35], [90, 0, 90]$ . These parameters led in the previous microcanonical ensemble to 1-2 dissociation and were chosen because the idea was that the thermal effects might trigger them to dissociate or diffuse to the 1-4 species. The duration of the trajectories was 1 ps and were done analogously as explained in section 3.2.3 except for now the thermalized surface. All of these 500 trajectories dissociated 1-2, no reflection, molecular adsorption or further dissociation could be observed. As it seems, the thermal contribution is low, which was unexpected. The energy of the thermalized surface can be estimated by  $N_s \times 3k_B T = 2.8 \text{ eV}$  (with  $N_s = 36$  being the number of atoms in the surface slab that were allowed to relax/move). This energy is in the same range as the kinetic energy of the incoming water molecule ( $\approx 2 \text{ eV}$ ). Indeed, this surface energy is not valid for the small surface range where the impact takes place, so that the thermal energy of the atom(s) of the impingement is considerably smaller.

As a next step, for all  $6 \times 8 = 48$  combinations of parameters, but with the thermalized surface, were done for all 6 impact points and 8 orientations presented in Section 3.2.3, but only for a kinetic energy of 0.7 eV. For each of the sets, two trajectories of 4 ps duration were calculated for at least a small statistic. This restriction is due to high computational costs and gives rise to only a limited statistical significance. The long duration accounts for processes that

### 3. Water on $\alpha\text{-Al}_2\text{O}_3(0001)$

occur later after the impact, that could have been missed by shorter trajectories. In Table 3.3, the probabilities for each process is shown, in comparison with the previous microcanonical AIMD trajectories. Because 6 of the trajectories aborted due to numerical reasons, here only 42 trajectories can be evaluated and the comparison is, of course, done only with the corresponding microcanonical trajectories. In the first line of the table, the results for the

**Table 3.3.:** Statistical results for NVE (both upper lines) and NVT trajectory at 300 K (lower line).

The models differ only by the thermalized surface, for all trajectories a single  $\text{D}_2\text{O}$  was sent on a clean surface with a kinetic energy of  $E_{\text{kin}} = 0.7 \text{ eV}$ . The initial parameters were the 48 and selected 42 from Section 3.2.3, respectively, as explained in the text.

ensemble	no. of trajectories	$P_{\text{refl}}$	$P_{\text{mol}}$	$P_{\text{diss}}(1\text{-}2)$	$P_{\text{diss}}(1\text{-}4)$
NVE <sup>1</sup>	48	0.19	0.58	0.23	0.00
NVE <sup>1,3</sup>	42	0.19	0.55	0.26	0.00
NVT <sup>2</sup>	$42 \times 2$	0.12	0.54	0.24	0.11

<sup>1</sup> Propagation time 1.22 ps. <sup>2</sup> Propagation time 4 ps. <sup>3</sup> A subset of the NVE/48 data set, corresponding to the same initial impact parameters as used for the NVT ensembles.

complete probed space for the NVE ( $T=0$ ) is shown, the second line gives the results for the corresponding 42 microcanonical trajectories and in the third line, the canonical results for 42 NVT trajectories ( $T = 300 \text{ K}$ ) are given. For all, the kinetic energy is  $E_{\text{kin}} = 0.7 \text{ eV}$ . In contrast to the microcanonical MD, the canonical yields 1-4 dissociation at a percentage of around 11% and gives slight decreases in the reflection, whereas molecular adsorption and 1-2 dissociation almost remain constant. From the 1-4 dissociated trajectories, 44% dissociated directly and 56% indirectly after initial molecular adsorption. Interestingly, all initial conditions in the trajectories that show 1-4 dissociation in the NVT led only to molecular adsorption in the NVE AIMD. The idea supposed earlier emanated that 1-4 dissociation from trajectories that gave 1-2 dissociation in NVE, but apparently the molecular species plays a more important role. Note, that the surface temperature indeed has an effect on the probabilities for the different processes and also 1-4 dissociation could be observed. As before, the first impact can lead to reflection and in a “bouncing” process, the molecule can also adsorb after another impact, in few cases also on another CUS atom as the initial impact was on.

#### 3.2.5. Refined Surface Model

In the experiment, after a certain time, the coverage will be higher, which will have an impact on the incoming molecule. To account for this a preadsorbed surface model was applied, where the minimum structure of the surface with a single adsorbed water molecule was used and a second  $\text{D}_2\text{O}$  was sent onto this surface. For the preadsorbed water, the three minima were

### 3.2. AIMD for MBS Process

assumed: (a) the molecular minimum, (b) the 1-2 dissociated species and (c) the less stable 1-4 dissociated water. The preadsorbed OD/D<sub>2</sub>O was adsorbed at the position [0.33,0.33], in the lower right  $1 \times 1$  sub cell of the super cell in Figure 3.2(a)-(c), that is located around the CUS atom at this lateral impact point.

For the incoming second water molecule with an initial kinetic energy of 0.7 eV, one has to distinguish two cases: The impact points  $[a_0, b_0]$  were chosen such that (i) the second water molecule is shot in the same  $1 \times 1$  sub cell where the preadsorbed water is adsorbed (the lower right part of the super cell) and (ii) in another sub cell, here, the lower left part. Once again, various initial orientations and impact points were probed for a propagation time of 1 ps.

First, NVE (microcanonical,  $T = 0$  K of the initial surface) were done. (i) In the first case, the incoming water is shot to the direct vicinity (same sub cell) of the preadsorbed molecular water, the second *incoming* D<sub>2</sub>O is observed to be either reflected or adsorb molecularly at another CUS atom after initial reflection from the preadsorbed water molecule. In the case of molecular preadsorbed water, the impact of the second molecule can make the molecular *preadsorbed* water dissociate to 1-2, 1-4 and even 1-4'. Assumingly, part of the energy is not used to overcome the barrier to diffusion/dissociation but to interaction with the preadsorbed molecular species. However, this does not happen for the 1-2 and the 1-4 *preadsorbed* species; only in one case it reacts to the molecular adsorbed species. As can be seen in Table 3.4, there is a difference between impact points direct on the CUS atom [0.33, 0.33] and the impact position next to the CUS position [0.35, 0.45]. Additional data is shown in the Appendix **TODO: name the section?**.

Considering the impact point [0.33,0.33] of the incoming water, that is exactly where the preadsorbed water is located, one can see either reflection (R) or molecular adsorption after diffusion to another CUS site (M in Table 3.4).

In contrast to that, an impact point near the CUS atom, [0.35,0.45], gives rise to a greater number of different outcomes. In the case of the molecular preadsorbed species, molecular adsorption on a neighboring CUS and physisorption above the preadsorbed molecular species (*i.e.* the molecule is not bound directly to a CUS atom but to water (fragments) via hydrogen bonds) can be observed, which leads to the conclusion, that clustering occurs at the surface. For the 1-2 dissociated preadsorbed system, also 1-2 dissociation on a neighboring CUS can be discovered. The 1-4 dissociated preadsorbed species gives in addition to molecular adsorption, physisorption also reflection. If the preadsorbed species is dissociated, molecular adsorption is clearly favored, followed by physisorption.

Looking at the preadsorbed species, the molecular species is mostly affected by the incoming molecule by showing dissociation to all dissociated states (1-2, 1-4 and also 1-4'), whereas the 1-2 dissociated preadsorbed species is not influenced at all. Only for one of the 1-4 preadsorbed

### 3. Water on $\alpha\text{-Al}_2\text{O}_3(0001)$

**Table 3.4.:** Selected results of preadsorbed surface trajectories for the microcanonical ensemble ( $NVT$ ,  $T = 0\text{ K}$ ,  $E_{\text{kin}} = 0.7\text{ eV}$ ). The three relevant cases are: molecular, 1-2 and 1-4 dissociated preadsorption. R=reflection, M=molecular adsorption (chemisorption), P=molecular physisorption, D(1-2)=1-2 dissociation, D(1-4)=1-4 dissociation. The two letters for each cell give the outcomes for the *incoming* molecule (first entry) and the *predisorbed* water (second entry). For the case that the predisorbed species changed its character, a \* is attached. “term.” refers to terminated trajectories. Missing entries mean that no calculation was done.

		type of preadsorption			
		molecular	1-2 dissociated	1-4 dissociated	
orientation	[ $\alpha, \beta, \gamma$ ]	impact position [ $a_0, b_0$ ] [0.33,0.33] [0.35,0.45]			
[0, 0, 0]		P, D(1-2)*		M, D(1-2)	R, D(1-4)
	[0, 0, 90]	M, D(1-2)*		M, D(1-2)	P, D(1-4)
	[0, 90, 0]	M, D(1-2)*	P, D(1-4)*	R, D(1-2)	P, D(1-4)
	[0, 90, 90]		P, D(1-4')*	M, D(1-2)	term.
	[90, 0, 0]		P, D(1-2)*	M, D(1-2)	M, D(1-4)
	[90, 0, 90]		P, M	D(1-2), D(1-2)	P, D(1-4)
	[90, 90, 0]		P, D(1-4)*	M, D(1-2)	R, D(1-4)
	[90, 90, 90]	M, D(1-2)*	P, D(1-4)*	R, D(1-2)	M, D(1-4)
				M, D(1-2)	P, D(1-4)

trajectories, a change of the state is observed, to a molecular species via proton transfer from the incoming water molecule.

(ii) In the second case, a neighboring sub cell (the lower left one) is the aim of the molecular beam, where no water is preadsorbed. The preadsorbed water or water fragments are hardly disturbed by the incoming  $\text{D}_2\text{O}$ , due to the great distance of the residues. Only a single trajectory out of 36 changed its character: the molecularly preadsorbed species exchanged a proton with the neighboring 1-2 dissociated incoming species after the impact and therefore dissociated.

Surprisingly, the incoming molecule is affected by the preadsorbed species in the way that the dissociation probability is increased and 1-4 dissociation occurs, in contrast to comparable previous microcanonical with a clean surface: Mostly molecular adsorption ( $P_{\text{mol}}=0.47$ ), dissociation ( $P_{1-2}=0.22$  and  $P_{1-4}=0.14$ ), physisorption ( $P_{\text{phys}}=0.11$ ) take place. Reflection is drastically decreased ( $P_{\text{refl}}=0.06$ ). Respective values for microcanonical MD of the clean surface are  $P_{\text{mol}}=0.58$ ,  $P_{1-2}=0.23$ ,  $P_{1-4}=0$ ,  $P_{\text{phys}}=0$  and  $P_{\text{refl}}=0.19$ . Although the statistics may not be sufficient, the reduced probability of reflection can be interpreted with attractive interaction of both the incoming and the preadsorbed molecule and leads to a higher probability of dissociation.

Summarizing these findings, one can say, that the preadsorbed enhancement of the system

### 3.2. AIMD for MBS Process

leads to further outcomes of the scattering as physisorption/clustering on the surface and the so far unreached 1-4 and 1-4' species, the latter by dissociation of preadsorbed molecular water. As it is not surprising, the influence is more massive with the incoming water molecule being near the preadsorbed species.

In analogy to these NVE trajectories, canonical (NVT, with  $T = 300\text{ K}$ ) trajectories with the preadsorbed systems were done. As before (Section 3.2.4), as a starting point the pre-equilibrated structures of molecular adsorption, 1-2 and 1-4 dissociation were used, that were equilibrated at 300 K for 1 ps. The following trajectories including the 0.7 eV water “beam” were run for 1 ps. As for the respective microcanonical trajectories, one has to distinguish between the water aiming at (i) the same sub cell (lower right) and (ii) the neighboring sub cell (lower left  $1 \times 1$  sub cell). The results do not differ largely, but some probabilities are altered. For case (i) in comparison with the microcanonical preadsorbed surface one can see that only physisorption is enhanced, whereas the other processes (molecular adsorption, 1-2, 1-4 dissociation and reflection) are suppressed. In the case of the water hitting the neighboring subcell (ii) similar effects can be seen, although here molecular adsorption is favored and the other processes (1-4 dissociation, physisorption and reflection) are reduced, and 1-2 dissociation happens with almost the same amount as in the NVE ensemble. Also concerning the preadsorbed water (fragment) there are changes, especially for the molecular preadsorbed species in case (i): Only in 4 out of 24 cases the character of the preadsorbed water changes. For the case of molecular preadsorption and the neighboring CUS, there is an increase in the molecular adsorption ( $P_{1-2}=0.34$  instead of 0.23 for microcanonical) leads to the conclusion, that the influence of the preadsorbed species is high despite the distance so that the non-locality of the process is enhanced. For further probabilities see Appendix.

#### 3.2.6. Refined Beam Model

Enhancing the beam is a further refinement and is done here in two different ways: assuming a water cluster as the approaching species and as a second improving method exciting the water molecule rotationally, vibrationally and with a combination of both.

##### ***Clustering***

As a cluster, the  $(\text{D}_2\text{O})_4$  system was optimized in the same periodic boundary conditions as the cell before but without the surface, for geometry see Figure 3.8. The same cluster was already shown to be the most stable one by Wales et al. [40], there it is called “up-down-up-down”. This cluster was then fired with a kinetic energy of 0.9 eV at the cold clean surface (NVE) from a distance of 4 Å above the Al surface layer, with a duration of around 1.22 ps. Once again,

### 3. Water on $\alpha\text{-Al}_2\text{O}_3(0001)$

several impact points (defined for the center of mass position) and orientations of the cluster were considered. These orientations were applied analogously to the previous ones with the axes of the rotations shown in Figure 3.8(b).

Evaluating the data shows that the cluster breaks up upon contact with the surface into

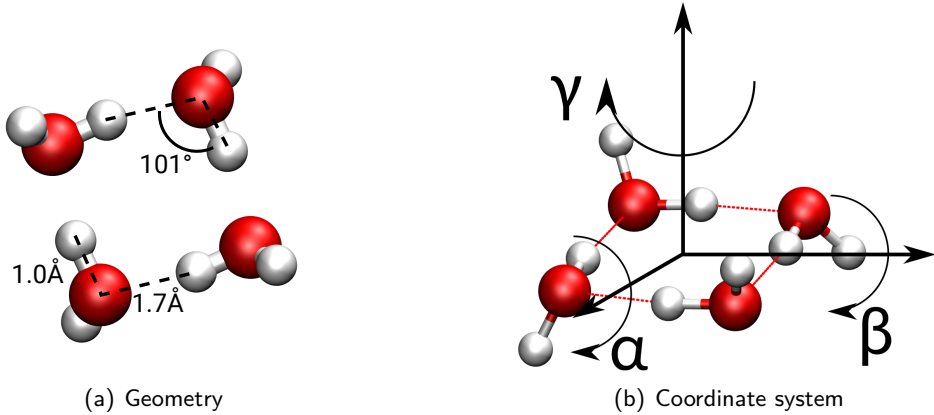


**Figure 3.8.:** (D<sub>2</sub>O)<sub>4</sub> cluster for simulation of effects of higher coverages. (a) shows the geometry, especially the DOD bond angle and the OD bond length of neighboring molecules and (b) shows the coordinate system for the rotations along the axes.

individual D<sub>2</sub>O molecules and these undergo different processes, to a great extent influenced by the surrounding water molecules, due to the high coverage of 1 ML (the 2 × 2 supercell with its four CUS positions can hold 4 water molecules in one mono layer). The water can adsorb molecularly or dissociatively (both directly and indirectly), physisorb, deuterium atoms can diffuse or single molecules can be reflected totally. Two examples of the final geometries can be found in Figure 3.9.

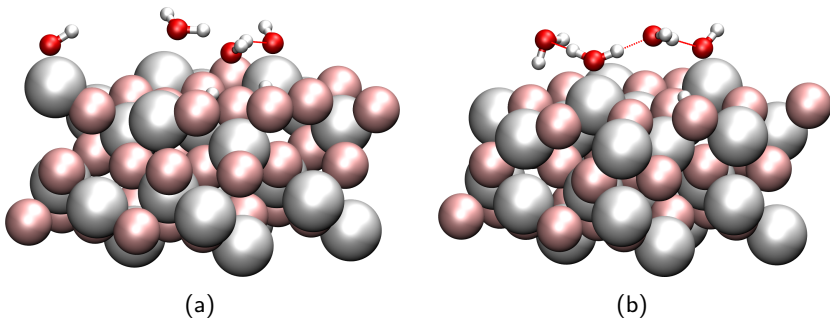


**Figure 3.9.:** Sideviews of the last time step (1.22 ps) for two initial conditions: (a)  $E_{\text{kin}} = 0.9 \text{ eV}$ ,  $[a_0, b_0] = [0.5, 0.35]$ , and  $[\alpha, \beta, \gamma] = [0, 0, 0]$  and (b)  $E_{\text{kin}} = 0.9 \text{ eV}$ ,  $[a_0, b_0] = [0.35, 0.5]$ , and  $[\alpha, \beta, \gamma] = [90, 90, 0]$ . Hydrogen bonds are shown as red dashed lines. Physisorption, molecular adsorption and dissociation can be seen in both snapshots.

### 3.2. AIMD for MBS Process

Mostly independent of the settings, the molecules interact strongly with each other showing a profoundly dynamic behavior. This gives rise to processes that were not possible for the clean surface NVE and a single water situation, where no 1-4 dissociation nor physisorption were observed. Of course, the probabilities for dissociation, molecular adsorption and reflection are different, the probability of molecular adsorption is strongly diminished to the advance of 1-2, 1-4 and 1-4' dissociation and physisorption. For details see Appendix.

#### ***Rotationally and vibrationally preexcited Water***

Here, qualitative results are given for a D<sub>2</sub>O molecule that is at the start of the trajectory not rigid as before but excited rotationally and/or vibrationally. It is shot with a kinetic energy of 0.7 eV at the clean surface in a NVE ensemble for a trajectory duration of 2 ps at the impact point [0.35, 0.5] with the initial orientation [0, 0, 0]. With these applied conditions in the rigid case (microcanonical at 0 K without rotational or vibrational excitation), the molecule dissociates to the 1-2 structure, the same for the thermal surface at  $T = 300\text{ K}$ .

The vibrational excitations were chosen as follows: For the single water molecule in the periodic boundary conditions a normal mode analysis was done. The eigenvectors of the dynamical matrix for the symmetric stretch, asymmetric stretch and the bending mode were used in a zeroth order approach (after proper scaling) as an input for the MD trajectories in addition to the initial momentum towards the surface. For the rotational preexcitations along the three axes, D atoms were given initial momenta to induce a rotational motion corresponding to rotational energies of  $\sim 0.2\text{ eV}$ .

The results for the rotation around the  $\gamma$ -axis (cp. Figure 3.4) shows molecular adsorption whereas rotations around the other two axes give 1-2 dissociation as in the initial microcanonical trajectories without rotational excitation. In the cases of vibrational preexcitation, the symmetric stretch leads to reflection, the asymmetric stretch gives 1-4' dissociation after initial 1-2 dissociation (as was already mentioned in Figure 3.6) and with the bending mode being excited, the water dissociates to 1-2. Also, a small collection of combinations of vibrations with rotations were calculated, that lead to either molecular adsorption (rotation around  $\alpha$  and bending mode), or 1-2 dissociation (rotation around  $\gamma$  and asymmetric stretch; and rotation around  $\beta$  and symmetric stretch).

Quantitatively, the results may depend strongly on the excitation energy, that was not of concern here, one can say, that preexcitation has an effect on the dynamics of the water adsorption and dissociation, respectively, that were not possible with the rigid water molecule.

Although a large number of trajectories were done with the contingent at the HLRN facility a

### 3. Water on $\alpha\text{-Al}_2\text{O}_3(0001)$

reliable statistics could not be achieved. It was only computationally feasible to do trajectories with 1–4 ps duration. Also only a limited set of degrees of freedom could be probed, *e.g.* the angle of the beam with respect to the surface was no other than 90° and initial orientations were only probed in 90° steps. Apart from that, no quantum effects were considered.

### 3.3. Improvement of Reaction Rates

For a model reaction we try to improve the reaction rate of a specific chosen reaction with different new methods. This reaction is a H-diffusion reaction on the (0001) surface studied before in our group, the Df-H-4-2 reaction, that moves a proton in the 1-4 position to the OH residue to the 1-2 dissociated state (see Figure 3.10). The transition state was calculated with

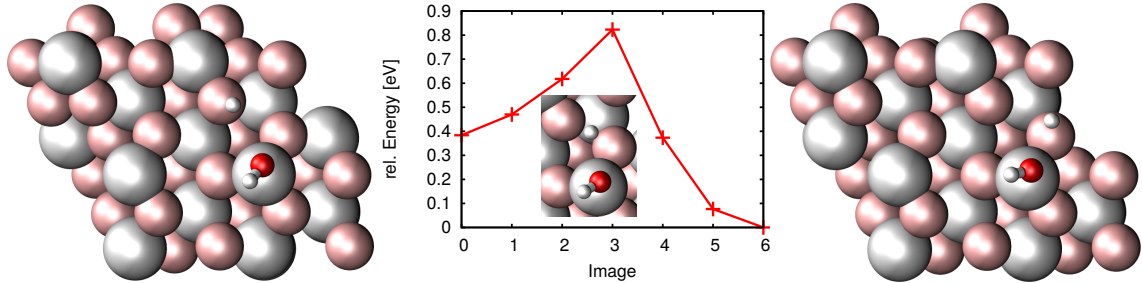


**Figure 3.10.:** Reaction path of the Df-H-4-2 proton diffusion reaction in the PBE-D2 level of theory, left is the educt (1-4), in the middle the minimum energy path with the transition state geometry as an inlay and on the right the product (1-2) of the reaction. *Data with friendly permission by Jonas Wirth.*

PBE+D2 with the implementation of Nudged Elastic Band in VASP. Rates were calculated via Eyring (Equation 1.26). An approach where singlepoint calculations at the HSE level of theory (hybrid functional) on top of PBE optimized geometries were done for the minima and the transition state was also done. Additionally, for this process a 1-D potential energy surface was calculated and then the Schrödinger equation was solved to obtain the wave function and see the localization/delocalization of the reaction pathway. These results are summarized in Table 3.5.

**Table 3.5.:** PW91, PBE+D2 after geometry optimization and transition state via NEB, HSE single point calculations on top of PBE optimized geometries. Both were calculated from Eyring equation 1.26. The exact tunneling was calculated from a 1-D potential and the calculation of the Schrödinger equation in this potential. These calculations were done by Dr. J. Wirth and partially unpublished.

Method	$k$ [ $s^{-1}$ ]
PW91	$1.97 \times 10^8$
PBE	$9.15 \times 10^7$
HSE	$3.15 \times 10^7$
“exact” tunneling (1D)	$6.49 \times 10^8$

Now we want to expand these methods to the following: We want to calculate the adsorption

### 3. Water on $\alpha\text{-Al}_2\text{O}_3(0001)$

energies and the barrier within a atom centered orbital method with the hybrid functional B3LYP and also go beyond density functional theory and go to perturbation theory (LMP2).

#### 3.3.1. MP2 and B3LYP

Going beyond pure density functionals and also beyond DFT has been too costly for a long time, simply not applicable for surface adsorbat system that large and electron rich. In the crystal/cryscor code one uses atom centered bases instead of plane waves and so large scale systems can also be computed. We first optimized our parameters with HF calculations and then did calculations with PBE similar to prior plane wave based calculations.

We found out, that BSSE takes a big part, but corrections are not easily applied because the ghosted calculations needed for that do not converge for all the structures with a bigger OH-H distance. Instead we have to use bigger basis sets containing diffuse functions in order to handle the BSSE. Such a self designed basis set by our cooperation partner Dr. Denis Usyat (HU Berlin, group of Martin Schütz) was used here. With this basis set we did the PBE calculations again (?) and the B3LYP as well as the MP2 calculations. First we compared the differences in adsorption energies. We furthermore compared the vibrational frequencies from B3LYP with the ones from VASP/PBE to see a methodological effect.

We also reoptimized the transition state for the Df-H-4-2 reaction.

## **Summary**

We made great progress in understanding the  $(11\bar{2}0)$  surface of  $\alpha\text{-Al}_2\text{O}_3$  in contact with water in the low coverage regime.

The dissociation process of water on  $(0001)$  surface was studied.

Several methods were tested to improve reaction rates.

## Acknowledgment

I want to thank my doctoral father Prof. Dr. Saalfrank, for giving me the scientific opportunity to research on surface systems and all the valuable discussions and advices. Also I am deeply grateful to my supervisor Dr. Jonas Wirth who gave me support during my time starting as a Bachelor's student, during my Master's thesis and also through the beginning of my PhD, PD Dr. Tillmann Klamroth for discussions about programming and theoretical questions that arose during the work, Dr. Radosław Włodarczyk for his endless knowledge with vasp and programming in general, Giacomo Melani (soon to be Dr.) for his advice and his help, and also the discussions about our teaching duties in mathematics and the whole workgroup for all the valuable discussions and the help. Also for the great atmosphere, that was some times productive and some times also just relaxing and felt very comfortable, here especially Clemens Rietze, Robert Scholz, Gereon Floss, and Steven Lindner. Also I want to thank my second supervisor Beate Paulus for discussion and help beyond research topics. Great acknowledgement to my experimental cooperation partners from FHI, Yanhua Yue, Dr. Harald Kirsch and Dr. Kramer R. Campen for the great work and publications we did together. Thanks to Dr. Denis Usvyat for all his patience and knowledge and valuable discussions about crystal/crysccor and his help. *TODO: Maristella Alessio from Sauer group (HU Berlin) for help with Turbomole and setting the mechanical embedding calculations, that unluckily did not work for the applied cluster. Ji Chen and Wei Fang from Michaelides group from UCL London for their help with cp2k and i-Pi, necessary for the PIMD calculations.*

Last I want to thank Dr. Jean Christophe Tremblay who brought me to theoretical chemistry by bringing my attention to this field of science. Christiane Wunderlich who was my school teacher in chemistry, without whom I would not have studied chemistry.

# Appendix

reaction pathways: dissociation Cb-iCa2 and Cb-iCb2 were tested but both were two step processes. Show reaction paths here? I think not..

Conversion of reciprocal coordinates a,b,c coordinates to x,y,z coordinates via matrix product:

$$(a'_1, b'_1, c'_1) \begin{pmatrix} a_1 & a_2 & a_3 \\ b_1 & b_2 & b_3 \\ c_1 & c_2 & c_3 \end{pmatrix} = (x_1, y_1, z_1)$$

with the matrix that is built up by the cell vectors.

## A. Experimental Techniques

In this work several experimental techniques were used from our collaborating group at the FHI in Berlin, that is why the basics of those methods shall be explained briefly.

### A.1. Vibrational Sum Frequency Generation

This method is a surface specific vibrational spectroscopy. An UV/Vis and an IR Laser beam are overlapped spatially and in time to produce the so called sum frequency signal, see Figure .1. There also the energy scheme is given: The system is excited with a pulse to a vibrationally excited state and with a UV/Vis pulse to a virtual state. The resulting SFG signal is a sum of both frequencies. For this, the polarization of the beam is important, it can be either s or

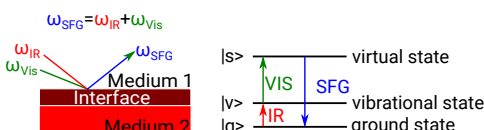


**Figure A.1:** Scheme of the SFG Process, left side the spatially overlapping Laser beams are shown, on the right side the orbital representation with the excitation to a virtual orbital is given.

p polarized. The selection rules result in the surface specificity: The SFG only occurs if the vibration is IR and Raman active and additionally only in systems with inversion symmetry.

## Appendix

This makes this method predestinated for analysis of surfaces, because neither the bulk nor the gas phase are inversion symmetric, however the interface (=surface, at least three atomic layers) is, so that the only signals come from this region. It is usually abbreviated SFG (sum frequency generation) but also named VSF (vibrational sum frequency).

### A.2. Thermal Desorption Spectroscopy

In thermal desorption spectroscopy (TDS, also temperature programmed desorption, TPD) the prepared sample is heated with a defined temperature program. Thus, adsorbates are removed from surface according their binding energies and detected as a function of temperature with any detection method required. The analysis sheds light on adsorption strength and probable reaction networks.

### A.3. Molecular Beam Source vs. Pinhole Dosing

When doing the experiment the method of preparation seems crucial for the results, because these result in different surface situations. Our collaborators use the so called Molecular Beam Source but also widely used is pinhole dosing. Here the idea behind these methods and the main differences shall be explained.

Pinhole Dosing (PD): Water is brought with a high partial pressure onto the surface. Problem here: in the gas phase and on the walls of the measuring chamber can be amounts of water left that can influence the measurement. This leads to an equilibrium situation.

Molecular Beam Source (MBS): A medium, e.g. water is probed onto the surface at a very low pressure. Non-equilibrium situations are generated by the kinetic energy of the beam.

*TODO: The difference between pinhole doser and MBS is that the former cannot heat the gas source to higher temperature but MBS can heat it to more than 800 K and this high energy is able to increase the dissociation of the gas source for example water or CH<sub>4</sub>. MBS is used instead of pinhole doser to enhance the dissociated population on the sample surface.*

### A.4. Low-Energy Electron Diffraction

Spectroscopical method for determining crystal structures in crystalline materials by an electron beam with an energy in the range from 20 to 200 eV. Diffracted electrons are observed as a pattern on a fluorescent screen. The structure can be derived from the geometry of this pattern and the lattice geometry can be seen. Problem is the high energy of the beam that can lead to damage in the sample.

*TODO: Other methods as tunneling based methods do not work on isolating materials like alu-*

## B. Reaction Probabilities

*mina, so that it is simply not possible to measure STM. Others? Rasterkraft? ATM?*

## B. Reaction Probabilities

Here, probabilities  $P$  for the different outcomes of the simulations will be listed, if not already given in the main text. The following abbreviations will be used:  $P_{\text{mol}}$ =molecular adsorption,  $P_{\text{diss}}(1\text{-}2)$ = 1-2 dissociation,  $P_{\text{diss}}(1\text{-}4)$ = 1-4 dissociation,  $P_{\text{diss}}(1\text{-}4')$ = 1-4' dissociation,  $P_{\text{phys}}$ = physisorption (of molecular D<sub>2</sub>O), and  $P_{\text{refl}}$ =reflection. If two numbers are given in one cell, this refers to direct (first number) and indirect (i.e., after prior molecular adsorption, second number) processes. If the sum of reaction probabilities is not exactly equal to one, this is due to the rounding procedure. When no probabilities are listed in the tables, e.g., for  $P_{\text{diss}}(1\text{-}4)$ ,  $P_{\text{diss}}(1\text{-}4')$  or  $P_{\text{phys}}$ , they are zero. Probabilities were obtained from (sometimes limited) swarms of trajectories, as specified for each case below.

### B.1. Microcanonical AIMD at a Clean Surface at $T = 0$

In the following Table, we show probabilities for the microcanonical (NVE) trajectories for a clean surface and a single D<sub>2</sub>O molecule approaching the surface initially at  $T = 0$  with different initial kinetic energies  $E_{\text{kin}}$ . This is the same information as in the first row of Tab.2 of the main text, there for  $E_{\text{kin}} = 0.7$  eV only.

**Table AB.1:** Reaction probabilities for the microcanonical (NVE,  $T = 0$ ) trajectories for a single D<sub>2</sub>O molecule approaching the clean surface with different initial kinetic energies. Results are averaged over 48 combinations of six initial impact sites and eight rotational orientations in each case.

$E_{\text{kin}}$ [eV]	$P_{\text{mol}}$	$P_{\text{diss}}(1\text{-}2)$	$P_{\text{refl}}$
0.5	0.56	0.17 + 0.08	0.19
0.6	0.58	0.17 + 0.06	0.19
0.7	0.58	0.17 + 0.06	0.19
0.8	0.54	0.15 + 0.12	0.19
0.9	0.50	0.19 + 0.04	0.27

### B.2. Refined Surface Models: Effects of Precoverage

In the main text (Sec.III.D.1), a refined surface model was considered with the surface ( $2 \times 2$ ) cell precovered with a single D<sub>2</sub>O molecule, either molecularly or dissociatively adsorbed (1-2 or 1-4 dissociation, see Table 3 of the main text). Then, a single D<sub>2</sub>O molecule was shot on

## Appendix

surface (at  $T = 0$  K), with an initial kinetic energy of 0.7 eV, and an impact site either within the same  $1 \times 1$  subcell as the preadsorbed species, or at a neighbouring  $1 \times 1$  subcell (see main text). Table B.2 gives corresponding reaction probabilities. These were obtained by averaging over 89 trajectories as detailed in the table caption / footnotes.

**Table AB.2:** Reaction probabilities for the microcanonical (NVE,  $T = 0$ ) trajectories of D<sub>2</sub>O approaching a preadsorbed surface with an initial kinetic energy of 0.7 eV. The incoming water was at an impact site close to the preadsorbed species (D<sub>2</sub>O, “preads.=mol” or OD fragment (“preads.=1-2 or 1-4”) in the lower right  $1 \times 1$  subcell of the  $2 \times 2$  unit cell, “same CUS”), or at an impact site close to a neighbouring CUS position (in the lower left  $1 \times 1$  subcell of the  $2 \times 2$  unit cell, “neighbour CUS”).

	preads.	$P_{\text{mol}}$	$P_{\text{diss}}(1\text{-}2)$	$P_{\text{diss}}(1\text{-}4)$	$P_{\text{phys}}$	$P_{\text{refl}}$
same CUS	mol <sup>1</sup>	0.57	0.00+0.04	0.04+0.00	0.32	0.04
	1-2 <sup>2</sup>	0.77	0.08+0.00	0.00	0.00	0.15
	1-4 <sup>3</sup>	0.42	0.00	0.00	0.33	0.25
neighbour CUS	mol <sup>4</sup>	0.36	0.18+0.05	0.23	0.18	0.00
	1-2 <sup>5</sup>	0.57	0.29	0.00	0.00	0.14
	1-4 <sup>6</sup>	0.71	0.14	0.00	0.00	0.14

<sup>1</sup> 28 trajectories, for [0.35,0.5], [0.5,0.35] and [0.35,0.45] all eight orientations and for the remaining three impact points only selected ones: [0.33,0.33]: [0,90,0] and [90,90,90]; [0.5,0.5]: [90,90,0] and [0.4,0.5]: [0,90,0]

<sup>2</sup> 13 trajectories, for [0.35,0.45] all eight orientations, [0.33,0.33]: [0,90,0] and [90,90,90]; [0.5,0.5]: [90,90,0]; [0.35,0.5]: [0,0,0]; [0.4,0.5]: [0,90,0]

<sup>3</sup> 12 trajectories, for [0.35,0.45] all orientations were calculated, but [0,90,90] failed, for [0.33,0.33]: [0,90,0] and [90,90,90]; [0.5,0.5]: [90,90,0]; [0.35,0.5]: [0,0,0]; [0.4,0.5]: [0,90,0]

<sup>4</sup> 22 trajectories, for [0.35,1.0] and [0.5,0.85] all orientations, [0.33,0.83]: [0,90,0] and [90,90,90]; [0.5,1.0]: [90,90,0]; [0.35,0.95]: [0,0,0] and [90,90,0]; [0.4,1.0]: [0,90,0]

<sup>5</sup> seven trajectories, for [0.33,0.83]: [0,90,0] and [90,90,90]; [0.5,1.0]: [90,90,0]; [0.35,1.0]: [0,0,0]; [0.35,0.95]: [0,0,0] and [90,90,0]; [0.4,1.0]: [0,90,0]

<sup>6</sup> seven trajectories, for [0.33,0.83]: [0,90,0] and [90,90,90]; [0.5,1.0]: [90,90,0]; [0.35,1.0]: [0,0,0]; [0.35,0.95]: [0,0,0] and [90,90,0]; [0.4,1.0]: [0,90,0]

Analogous information is given in Table B.3 for NVT calculations, for a preequilibrated, precovered surface. The surface was equilibrated for 1 ps at 300 K starting from the minimum structures of the adsorbed species. The water molecule was shot with an initial kinetic energy of 0.7 eV in 140 trajectories as detailed in the table caption / footnotes.

### B.3. Refined Beam Models: Clustering and Preexcitation

Table B.4 refers to a beam model in which a (D<sub>2</sub>O)<sub>4</sub> cluster was shot with an initial kinetic energy of 0.9 eV on a cold, naked surface, see section III.D.2 in the main text. In total we did ten trajectories with a kinetic energy of 0.9 eV of the incoming water molecule for four different

## B. Reaction Probabilities

**Table AB.3:** The same as Tab.B.2, for the canonical (NVT) case ( $T = 300$  K). Here, only three impact points were considered for the “same CUS”: [0.33,0.33], [0.35,0.45] and [0.5,0.35] and four for the “neighbouring CUS”: [0.33,0.83], [0.35,0.95] and [0.5,0.85], see Figure .2. If not mentioned otherwise, all eight rotational orientations were considered in each case.

	preads.	$P_{\text{mol}}$	$P_{\text{diss}}(1-2)$	$P_{\text{diss}}(1-4)$	$P_{\text{phys}}$	$P_{\text{refl}}$
same CUS	mol	0.08+0.17	0.00+0.04	0.00	0.63	0.08
	1-2	0.00+0.83	0.00	0.00	0.13	0.04
	1-4 <sup>1</sup>	0.05+0.40	0.00+0.05	0.00	0.40	0.10
neighbour CUS	mol	0.63	0.17+0.17	0.04	0.00	0.00
	1-2	0.71	0.21	0.08	0.00	0.00
	1-4	0.92	0.08	0.00	0.00	0.00

<sup>1</sup> for [0.33,0.33] the orientations [0,0,0], [90,90,0] and [90,90,90] and for impact points [0.5,0.35] the orientation [90,0,90] the trajectories failed and were not analyzed

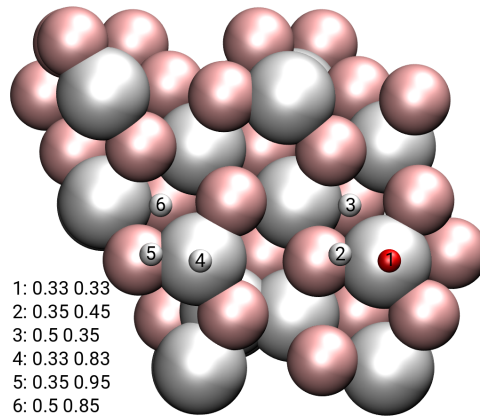


**Figure A.2:** Impact points for the calculations from Table B.3 for the “same” and the “neighboring” CUS.

impact points and three different orientations (for one impact point only a single orientation was considered).

Finally, results for microcanonical trajectories of a (single) D<sub>2</sub>O molecule, that was vibrationally and/or rotationally excited approaching a clean surface with an initial kinetic energy of 0.7 eV can be found in Table B.5. Averaged was over all ten trajectories (three rotations, three vibrations (symmetric, asymmetric and bending), and four rotations coupled with vibrations) for only one set of parameters ([0.35,0.5],[0,0,0]). The initial translational energy of D<sub>2</sub>O was 0.7 eV.

## Appendix

**Table AB.4:** Reaction probabilities for microcanonical (NVE,  $T = 0$ ) trajectories of a  $(D_2O)_4$  cluster approaching a clean surface with  $E_{kin} = 0.9$  eV.

$P_{mol}$	$P_{diss}(1-2)$	$P_{diss}(1-4)$	$P_{diss}(1-4')$	$P_{phys}$	$P_{refl}$
0.25	0.05+0.10	0.03+0.18	0.00+0.05	0.18	0.18

**Table AB.5:** Reaction probabilities for microcanonical (NVE,  $T = 0$ ) trajectories of vibrationally and/or rotationally excited  $D_2O$  approaching a clean surface with  $E_{kin} = 0.7$  eV.

$P_{mol}$	$P_{diss}(1-2)$	$P_{diss}(1-4)$	$P_{diss}(1-4')$	$P_{phys}$	$P_{refl}$
0.20	0.30+0.20	0.00	0.00+0.10	0.00	0.20

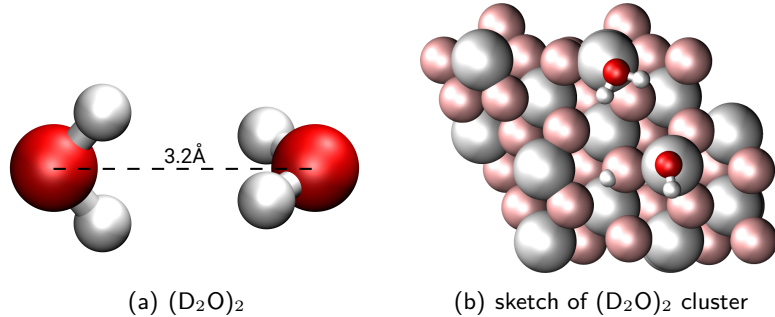


**Figure A.3:** Structure of the optimized  $(D_2O)_2$  cluster (a). (b) shows an example situation at the last step (after 1.2 ps) for 2 water molecules for the initial parameters  $[a_0, b_0] = [0.35, 0.45]$ ,  $[\alpha, \beta, \gamma] = [90, 0, 90]$ .

## C. 2D<sub>2</sub>O Cluster

Also one type of  $(D_2O)_2$  was tested (see Figure .3). The structure is not the minimum structure but another dimolecular water cluster. Even in the case of the  $(D_2O)_2$  cluster, strong interaction between the molecules can be observed, although not as much as for the tetramer. Also “only” molecular adsorption, 1-2 and 1-4 dissociation occur within the sampling. Interestingly, there is no case, where both molecules react in the same way. For most dissociated trajectories there is only direct dissociation at the moment of the impact, with the only one dissociating 0.3 ps later. Apart from that, no further dissociation and diffusion reactions were observed.

**TODO:** also a table with the probabilities here!

*C. 2D<sub>2</sub>O Cluster*

## Publications

### ***This Work:***

- (1) Heiden, S.; Yue, Y.; Kirsch, H.; Wirth, J.; Saalfrank, P.; Campen, R. K.: »Water Dissociative Adsorption on  $\alpha\text{-Al}_2\text{O}_3(11\bar{2}0)$  Is Controlled by Surface Site Undercoordination, Density, and Topology«, *Journal of Physical Chemistry C* **2018**, 122 (12), 6573-6584.
- (2) Heiden, S.; Wirth, J.; Campen, R. K.; Saalfrank, P.: »Water Molecular Beam Scattering at  $\alpha\text{-Al}_2\text{O}_3(0001)$ : An *Ab Initio* Molecular Dynamics Study«, *Journal of Physical Chemistry C* **2018**, vol, pp.

## References

- [1] Ago, H.; Nakamura, K.; Ikeda, K.; Uehara, N.; Ishigami, N.; Tsuji, M. Aligned Growth of Isolated Single-Walled Carbon Nanotubes Programmed by Atomic Arrangement of Substrate Surface, *Chem. Phys. Lett.* **2005**, *408*, 433-438.
- [2] Cargnello, M.; Delgado, J.; Hernández, J.; Bakmutsky, K. ; Montini, T.; Gámez, J. C.; Gorte, R.; Fornasiero, P. Exceptional Activity for Methane Combustion over Modular Pd@CeO<sub>2</sub> Subunits on Functionalized Al<sub>2</sub>O<sub>3</sub>, *Science* **2012**, *337*,
- [3] Knözinger, H.; Ratnasamy, P. Catalytic Aluminas: Surface Models and Characterization of Surface Sites, *Catal. Rev.* **1978**, *17*, 31-70.
- [4] Elam, J. W.; Nelson, C. E.; Cameron, M. A.; Tolbert, M. A.; George, S. M. Adsorption of H<sub>2</sub>O on a Single-Crystal  $\alpha$ -Al<sub>2</sub>O<sub>3</sub>(0001) Surface, *J. Phys. Chem. B* **1998**, *102*, 7008-7015.
- [5] Environmental Effects of the Space Shuttle, *Environ. Sci.* **1978**, *21*, 15-21.
- [6] Cofer, W. R.; Lala, G. G.; Wightman, J. P. Analysis of Mid-Tropospheric Space Shuttle Exhausted Aluminum Oxide Particles, *Atmos. Environ.* **1987**, *21*, 1187-1196.
- [7] Jones, A. E.; Bekki, S.; Pyle, J. A. On the Atmospheric Impact of Launching the Ariane 5 Rocket, *J. Geophys. Res.: Atm.* **1995**, *100*, 16651-16660.
- [8] Jackman, C. H.; Fleming, E. L.; Chandra, S.; Considine, D. B.; Rosenfield, J. E. Past, Present, and Future Modeled Ozone Trends with Comparisons to Observed Trends, *J. Geophys. Res.: Atm.* **1996**, *101*, 753-28.
- [9] Riedel, E.; Janiak, C. *Anorganische Chemie*; Walter de Gruyter: Berlin, 7 ed.; 2007.
- [10] Breuer, H. *dtv-Atlas Chemie, Band 1, Allgemeine und anorganische Chemie*; dtv: München, 9 ed.; 2000.
- [11] Trail, D.; Watson, E. B.; Tailby, N. D. The Oxidation State of Hadean Magmas and Implications for Early Earth's Atmosphere, *Nature* **2011**, *480*, 79-82.
- [12] Jensen, F. *Introduction to Computational Chemistry*; Wiley: 2 ed.; 2007.
- [13] Born, M.; Oppenheimer, R. Zur Quantentheorie der Moleküle, *Annalen der Physik* **1927**, *389*, 457-484.

- [14] Monkhorst, H. J.; Pack, J. D. Special Points for Brillouin-Zone Integrations, *Phys. Rev. B* **1976**, *13*, 5177.
- [15] Tosoni, S.; Tuma, C.; Sauer, J.; Civalleri, B.; Ugliengo, P. A comparison between plane wave and Gaussian-type orbital basis sets for hydrogen bonded systems: Formic acid as a test case, *J. Chem. Phys.* **2007**, *127*, 154102-1-11.
- [16] Marx, D.; Hutter, J. *Ab Initio Molecular Dynamics: Basic Theory and Advanced Methods*; Cambridge University Press: 2012.
- [17] Verlet, L. Computer "Experiments" on Classical Fluids. I. Thermodynamical Properties of Lennard-Jones Molecules, *Phys. Rev.* **1967**, *159*, 98–103.
- [18] Nosé, S. A Unified Formulation of the Constant Temperature Molecular Dynamics Methods, *J. Chem. Phys.* **1984**, 511-519.
- [19] Nosé, S. A Molecular Dynamics Method for Simulations in the Canonical Ensemble, *Mol. Phys.* **1984**, 255-68.
- [20] Hoover, W. G. Canonical Dynamics: Equilibrium Phase-Space Distributions, *Phys. Rev. A* **1985**, 1695-97.
- [21] Karhánek, D.; Bučko, T.; Hafner, J. A Density-Functional Study of the Adsorption of Methane-Thiol on the (111) Surfaces of the Ni-Group Metals: II. Vibrational Spectroscopy, *J. Phys.: Condens. Matter* **2010**, *22*, 265006-1-9.
- [22] Grillo, F.; Garrido Torres, J. A.; Treanor, M.-J.; Larrea, C. R.; Götze, J. P.; Lacovig, P.; Fruchtl, H. A.; Schaub, R.; Richardson, N. V. Two-Dimensional Self-Assembly of Benzotriazole on an Inert Substrate, *Nanoscale* **2016**, *8*, 9167-9177.
- [23] Thomas, M.; Brehm, M.; Fligg, R.; Vöhringer, P.; Kirchner, B. Computing Vibrational Spectra from *Ab Initio* Molecular Dynamics, *Phys. Chem. Chem. Phys.* **2013**, *15*, 6608.
- [24] Horníček, J.; Kaprálová, P.; Bouř, P. Simulations of Vibrational Spectra from Classical Trajectories: Calibrations with *Ab Initio* Force Fields, *J. Chem. Phys.* **2007**, *127*, 084502-1-9.
- [25] Hudecová, J.; Hopmann, K.; Bouř, P. Correction of Vibrational Broadening in Molecular Dynamics Clusters with the Normal Mode Optimization Method, *J. Phys. Chem. B* **2012**, *116*, 336–342.
- [26] Zhao, Y.; González-García, N.; Truhlar, D. G. Benchmark Database of Barrier Heights for Heavy Atom Transfer, Nucleophilic Substitution, Association, and Unimolecular Reactions and Its Use to Test Theoretical Methods, *J. Phys. Chem. A* **2005**, *109*, 2012-2018.
- [27] Møller, C.; Plesset, M. S. Note on an Approximation Treatment for Many-Electron Systems, *Phys. Rev.* **1934**, *46*, 618-622.
- [28] Wirth, J.; Saalfrank, P. The Chemistry of Water on  $\alpha$ -Alumina: Kinetics and Nuclear Quantum Effects from First Principles, *J. Phys. Chem. C* **2012**, *116*, 26829-26840.

- [29] Kirsch, H.; Wirth, J.; Tong, Y.; Wolf, M.; Saalfrank, P.; Campen, R. K. Experimental Characterization of Unimolecular Water Dissociative Adsorption on  $\alpha$ -Alumina, *J. Phys. Chem. C* **2014**, *118*, 13623-13630.
- [30] Tong, Y.; Wirth, J.; Kirsch, H.; Wolf, M.; Saalfrank, P.; Campen, R. K. Optically Probing Al-O and O-H Vibrations to Characterize Water Adsorption and Surface Reconstruction on  $\alpha$ -Alumina: An Experimental and Theoretical Study, *J. Chem. Phys.* **2015**, *142*, 054704.
- [31] Wirth, J.; Kirsch, H.; Włosczyk, S.; Tong, Y.; Saalfrank, P.; Campen, R. K. Characterization of Water Dissociation on  $\alpha$ -Al<sub>2</sub>O<sub>3</sub>(1102): Theory and Experiment, *Phys. Chem. Chem. Phys.* **2016**, *18*, 14822-14832.
- [32] Passerini, L. Solid Solutions, Isomorphism and Symmorphism of the Oxide of Trivalent Metals: The Systems Al<sub>2</sub>O<sub>3</sub>-Cr<sub>2</sub>O<sub>3</sub>, Al<sub>2</sub>O<sub>3</sub>-Fe<sub>2</sub>O<sub>3</sub>, Cr<sub>2</sub>O<sub>3</sub>-Fe<sub>2</sub>O<sub>3</sub>, *Gazz. Chim. Ital.* **1930**, *60*, 544.
- [33] Wyckoff, R. W. G. *The Structure of Crystals*; American Chemical Society: 1931.
- [34] Stair, P. C. The Concept of Lewis Acids and Bases Applied to Surfaces, *J. Am. Chem. Soc.* **1982**, *104*, 4044-4052.
- [35] Kurita, T.; Uchida, K.; Oshiyama, A. Atomic and Electronic Structures of  $\alpha$ -Al<sub>2</sub>O<sub>3</sub> Surfaces, *Phys. Rev. B* **2010**, *82*, 155319.
- [36] Heiden, S.; Yue, Y.; Kirsch, H.; Wirth, J.; Saalfrank, P.; Campen, R. K. Water Dissociative Adsorption on  $\alpha$ -Al<sub>2</sub>O<sub>3</sub>(1120) Is Controlled by Surface Site Undercoordination, Density, and Topology, *J. Phys. Chem. C* **2018**, *122*, 6573–6584.
- [37] Wirth, J. *Chemische Reaktionen in Substrat-Adsorbat-Systemen: Eine kinetische Perspektive*, Thesis, Universität Potsdam, 2014.
- [38] Hass, K. C.; Schneider, W. F.; Curioni, A.; Andreoni, W. The Chemistry of Water on Alumina Surfaces: Reaction Dynamics from First Principles, *Science* **1998**, *282*, 265–268.
- [39] Hass, K. C.; Schneider, W. F.; Curioni, A.; Andreoni, W. First-Principles Molecular Dynamics Simulations of H<sub>2</sub>O on  $\alpha$ -Al<sub>2</sub>O<sub>3</sub>(0001), *J. Phys. Chem. B* **2000**, *104*, 5527–5540.
- [40] Wales, D. J.; Walsh, T. R. Theoretical Study of the Water Tetramer, *J. Chem. Phys.* **1997**, *106*, 7193-7207.

## **Erklärung**

Hiermit versichere ich, dass die vorliegende Arbeit an keiner anderen Hochschule eingereicht sowie selbständig und ausschließlich mit den angegebenen Mitteln angefertigt worden ist.

Potsdam, xx 2018